

LAMINAR SIMULATION OF PULSATIONS IN
SUBCHANNEL GEOMETRIES

LAMINAR SIMULATION OF FLOW PULSATIONS IN
SIMPLIFIED SUBCHANNEL GEOMETRIES

By

ALAN CHETTLE, B.ENG

A Thesis

Submitted to the School of Graduate Studies

in Partial Fulfillment of the Requirements

for the Degree

Master of Applied Science

McMaster University

© Copyright by Alan Chettle, September 2011

MASTER of APPLIED SCIENCE (2011)

McMaster University

(Mechanical Engineering)

Hamilton, Ontario

TITLE: Laminar Simulation of Flow Pulsations in
Simplified Subchannel Geometries

AUTHOR: Alan Chettle, Bachelor of Engineering
(McMaster University)

SUPERVISORS: Dr. M. F. Lightstone
Dr. S. Tullis

NUMBER OF PAGES: xxi, 145

ABSTRACT

Flow pulsations in subchannel geometries play an important role in homogenization of fluid temperatures within a fuel rod bundle cross-section. As such, there is a strong need to develop accurate integral models that incorporate the underlying physics of these flows for inclusion in the broader safety analysis codes. This research is concerned with using computational fluid dynamics to investigate the flow pulsations in order to develop an enhanced understanding of the flow physics. The vast majority of previous experimental work has been in the turbulent regime, with varying degrees of geometric complexity. Previous numerical work has focused on steady or unsteady simulation of the turbulent experimental results, with the requirement that an appropriate turbulence model must be selected.

Recent experimental work by Gosset and Tavoularis in 2006 has indicated that flow pulsations can occur under laminar conditions. Computational modeling of laminar flow pulsations provides an ideal framework for studying the physical mechanisms or instabilities that promote formation of the pulsations. Simulations of their experimental domain were run for a gap height normalized by the rod diameter (δ/D) of 0.3 and Reynolds numbers of 718, 900 and 955. These simulations found frequencies in the same range as Gosset and Tavoularis, as well as qualitatively similar particle tracks to their dye streaks. Analysis of the numerical pulsations showed them to be fluid rotations around the rod. These rotations were shown to be strongly correlated with the axial velocity gradient, which acted to transfer momentum from axial flow to the crossplane rotational pulsatile flow. The pulsations were shown to develop from a purely

axial flow through disturbances in the axial velocity gradient, which initially arose near inflection points in the axial velocity profile in the spanwise direction. Under the influence of the axial velocity gradient and fluctuating pressure, these disturbances evolve into a sustained quasi-periodic flow.

Acknowledgements

Firstly, I thank my friends and family who partner with me in the work of the Kingdom. There are far too many to list by name, but they all have given much needed support, encouragement and wisdom to me throughout my time at McMaster. Without their consistent prayers and love, this work could never have been completed. The supervision and guidance of Dr. Lightstone and Dr. Tullis have helped me in developing my skills as a researcher. The financial support of the University Network of Excellence in Nuclear Engineering (UNENE) and the Natural Science and Engineering Research Council of Canada (NSERC) are gratefully acknowledged. This work was made possible by the facilities of the Shared Hierarchical Academic Research Computing Network (SHARCNET) and Compute/Cancel Canada.

Dedication

For the Lord God Almighty - Father, Son and Spirit.

Contents

1.0	Introduction	1
1.1	Motivation for Research	1
1.2	Objectives of Thesis	4
1.3	Thesis Structure ..	5
2.0	Literature Review	7
2.1	Introduction	7
2.2	Experimental work	8
2.2.1	Mean Flow Investigation	8
2.2.2	Secondary Flow Investigation	9
2.2.3	Turbulent Transport Investigation	14
2.2.4	Periodic Structures Investigation	17
2.3	Numerical Work	33
2.3.1	Reynolds Averaged Navier Stokes (RANS) Numerical Work	33

- 2.32. Unsteady Reynolds Averaged Navier Stokes (URANS) Numerical Work 39
- 2.4 Summary 46
- 3.0 Methodology 47
 - 3.1 Introduction 47
 - 3.2 Details of Experiment 47
 - 3.3 Simulation Details 50
 - 3.3.1 Spatial and Temporal Grid Setup 50
 - 3.3.1.1 Independence Tests 51
 - 3.3.2 Fluid Properties 56
 - 3.3.3 Boundary and Initial Conditions 56
 - 3.3.4 Advection Scheme 57
 - 3.3.5 Modeling of the Transient Term 58
 - 3.3.6 Equipment and Resources. 58
- 4.0 Results and Discussion 59
 - 4.1 Overview 59

4.2	Contour Plots of Velocity and Fluctuating Pressure	60
4.3	Spanwise Velocity Time Traces	65
4.4	Sensitivity to Domain Length	79
4.5	Particle Track Data	81
4.6	Q-Criterion Plots and Cross-plane Visualizations	84
4.7	Evolution of Pulsing Flow	110
5.0	Closure	133
5.1	Summary and Conclusions	133
5.2	Recommendations for Future Work	135

List of Tables

2.1	Summary of Experimental Investigations.	26
2.2	Summary of Reynolds Averaged Navier Stokes investigations	37
2.3	Summary of Unsteady Reynolds Averaged Navier Stokes investigations	43
3.1	Details of the independence tests conducted	51
3.2	Fluid properties used in simulations	56
4.1	Range of the measured quantities	64
4.2	Summary table of maximum and minimum velocities	73
4.3	Comparison between experimental and predicted frequencies	78
4.4	Average wavelengths from particle track data	83

List of Figures

1.1	Cross-section of a 37 element fuel rod bundle. Adapted from Eiff and Lightstone [4]	2
2.1	Mixing Coefficient vs Reynolds number, taken from Van Der Ros and Bogaardt [3]	9
2.2	Secondary flows measured by a x-probe, with the flow direction stylized in the image in the top left. Adapted from [36].	14
2.3	Contours of axial velocity, Adapted from Rehme [9].	16
2.4	Reynolds number vs Frequency and Strouhal number. Data taken from Meyer and Rehme [46].	19
2.5	Reynolds number vs Strouhal number. Adapted from Gosset and Tavoularis [53] . . .	24
3.1	Cross-section of the experimental domain of Gosset and Tavoularis [53]	48
3.2	Reynolds number vs Strouhal number. Adapted from Gosset and Tavoularis [53] Red symbols indicate where simulations were run	49
3.3	Cross-section of mesh used in all simulations.	50
3.4	Diagram of the discrete points used in the independence tests.	52
3.5	Time trace of spanwise velocity for the coarse grid	53
3.6	Time trace of spanwise velocity for the fine grid	54

3.7	Time trace of spanwise velocity for the fine timestep.	54
3.8	Frequency spectra for each independence study conducted.	55
4.1	Visualization plane used for contour plots viewed from the top down.	60
4.2	Contour plots of total velocity for the three different cases.	61
4.3	Contour plots of spanwise velocity for the three different cases.	62
4.4	Contour plots of fluctuating pressure for the three different cases	63
4.5	Spanwise velocity time trace for $Re = 718$. Taken from a point at the far left of the gap.	65
4.6	Spanwise velocity time trace for $Re = 718$. Taken from a point at the far right of the gap.	66
4.7	Spanwise velocity time trace for $Re = 718$. Taken from a point at the centre of the gap.	66
4.8	Spanwise velocity time trace for $Re = 900$. Taken from a point at the far left of the gap.	67
4.9	Spanwise velocity time trace for $Re = 900$. Taken from a point at the far right of the gap.	67
4.10	Spanwise velocity time trace for $Re = 900$. Taken from a point at the centre of the gap.	68

4.11	Spanwise velocity time trace for $Re = 955$. Taken from a point at the far left of the gap.	68
4.12	Spanwise velocity time trace for $Re = 955$. Taken from a point at the far right of the gap.	69
4.13	Spanwise velocity time trace for $Re = 955$. Taken from a point at the centre of the gap.	69
4.14	Distribution of Spanwise Velocity for $Re = 718$	70
4.15	Distribution of Spanwise Velocity for $Re = 900$	71
4.16	Distribution of Spanwise Velocity for $Re = 955$	71
4.17	Skewness plot for all Reynolds numbers	73
4.18	Discrete Fourier transform of the spanwise velocity time trace for $Re = 718$	75
4.19	Discrete Fourier transform of the spanwise velocity time trace for $Re = 900$	75
4.20	Discrete Fourier transform of the spanwise velocity time trace for $Re = 955$	76
4.21	Strouhal number vs Reynolds number for the combined work of Gosset and Tavoularis (GT) [53], Meyer and Rehme (MR) [46] and the present work	78
4.22	Number of periods of spanwise velocity vs domain length.	80
4.23	Average wavelength of spanwise velocity vs domain length.	81
4.24	Particle tracks for $Re = 718$	82
4.25	Particle tracks for $Re = 900$	82

4.26	Dye streak image from Gosset and Tavoularis [53] for a Reynolds number of 894. . .	82
4.27	Particle tracks for $Re = 955$	82
4.28	Isosurface plot of Q-criterion for $Re = 718$	85
4.29	Vector plot of crossplane velocity (u and v) with shaded contours of axial velocity behind for $Re = 718$, 665 mm downstream of inlet.	86
4.30	Vector plot of crossplane velocity (u and v) with shaded contours of axial velocity gradient behind for $Re = 718$, 665 mm downstream of inlet.	86
4.31	Vector plot of crossplane velocity (u and v) with shaded contours of pressure behind for $Re = 718$, 665 mm downstream of inlet.	87
4.32	Vector plot of crossplane velocity (u and v) with shaded contours of axial velocity behind for $Re = 718$, 687 mm downstream of inlet.	88
4.33	Vector plot of crossplane velocity (u and v) with shaded contours of axial velocity gradient behind for $Re = 718$, 687 mm downstream of inlet.	89
4.34	Vector plot of crossplane velocity (u and v) with shaded contours of pressure behind for $Re = 718$, 687 mm downstream of inlet.	89
4.35	Vector plot of crossplane velocity (u and v) with shaded contours of axial velocity behind for $Re = 718$, 710 mm downstream of inlet.	91
4.36	Vector plot of crossplane velocity (u and v) with shaded contours of axial velocity gradient behind for $Re = 718$, 710 mm downstream of inlet.	91
4.37	Vector plot of crossplane velocity (u and v) with shaded contours of pressure behind for $Re = 718$, 710 mm downstream of inlet.	92
4.38	Isosurface plot of Q-criterion for $Re = 900$	93

4.39	Vector plot of crossplane velocity (u and v) with shaded contours of axial velocity behind for Re = 900, 540 mm downstream of inlet.	94
4.40	Vector plot of crossplane velocity (u and v) with shaded contours of axial velocity gradient behind for Re = 900, 540 mm downstream of inlet...	95
4.41	Vector plot of crossplane velocity (u and v) with shaded contours of pressure behind for Re = 900, 540 mm downstream of inlet.	95
4.42	Vector plot of crossplane velocity (u and v) with shaded contours of axial velocity behind for Re = 900, 580 mm downstream of inlet.	97
4.43	Vector plot of crossplane velocity (u and v) with shaded contours of axial velocity gradient behind for Re = 900, 580 mm downstream of inlet.	97
4.44	Vector plot of crossplane velocity (u and v) with shaded contours of pressure behind for Re = 900, 580 mm downstream of inlet.	98
4.45	Vector plot of crossplane velocity (u and v) with shaded contours of axial velocity behind for Re = 900, 620 mm downstream of inlet.	99
4.46	Vector plot of crossplane velocity (u and v) with shaded contours of axial velocity gradient behind for Re = 900, 620 mm downstream of inlet.	100
4.47	Vector plot of crossplane velocity (u and v) with shaded contours of pressure behind for Re = 900, 620 mm downstream of inlet.	100
4.48	Isosurface plot of Q-criterion for Re = 955.	102
4.49	Vector plot of crossplane velocity (u and v) with shaded contours of axial velocity behind for Re = 955, 560 mm downstream of inlet.	103

4.50	Vector plot of crossplane velocity (u and v) with shaded contours of axial velocity gradient behind for Re = 955, 560 mm downstream of inlet.	103
4.51	Vector plot of crossplane velocity (u and v) with shaded contours of pressure behind for Re = 955, 560 mm downstream of inlet.	104
4.52	Vector plot of crossplane velocity (u and v) with shaded contours of axial velocity behind for Re = 955, 585 mm downstream of inlet.	105
4.53	Vector plot of crossplane velocity (u and v) with shaded contours of axial velocity gradient behind for Re = 955, 585 mm downstream of inlet.	106
4.54	Vector plot of crossplane velocity (u and v) with shaded contours of pressure behind for Re = 955, 585 mm downstream of inlet.	106
4.55	Vector plot of crossplane velocity (u and v) with shaded contours of axial velocity behind for Re = 955, 610 mm downstream of inlet.	108
4.56	Vector plot of crossplane velocity (u and v) with shaded contours of axial velocity gradient behind for Re = 955, 610 mm downstream of inlet.	108
4.57	Vector plot of crossplane velocity (u and v) with shaded contours of pressure behind for Re = 955, 610 mm downstream of inlet.	109
4.58	Total velocity contours for Re = 718, 60.5 to 63.5 seconds after starting the transient from zero velocity.	111
4.59	Axial velocity gradient contour with crossplane velocity vectors in front. Re = 718, 60.5 seconds after starting the transient from zero velocity.	111
4.60	Total velocity contours for Re = 718, 65.5 to 68.5 seconds after starting the transient from zero velocity.	112
4.61	Axial velocity gradient contour with crossplane velocity vectors in front. Re = 718, 65.5 seconds after starting the transient from zero velocity.	113

4.62	Axial velocity gradient contour with crossplane velocity vectors in front. Re = 718, 67.5 seconds after starting the transient from zero velocity.	113
4.63	Axial velocity gradient contour with crossplane velocity vectors in front. Re = 718, 68.5 seconds after starting the transient from zero velocity.	114
4.64	Total velocity contours for Re = 718, 72.5 seconds after starting the transient from zero velocity.	115
4.65	Axial velocity gradient contour with crossplane velocity vectors in front. Re = 718, 72.5 seconds after starting the transient from zero velocity, 720 mm downstream from inlet.	115
4.66	Axial velocity gradient contour with crossplane velocity vectors in front. Re = 718, 72.5 seconds after starting the transient from zero velocity, 760 mm downstream from inlet.	116
4.67	Axial velocity gradient contour with crossplane velocity vectors in front. Re = 718, 72.5 seconds after starting the transient from zero velocity, 800 mm downstream from inlet.	116
4.68	Total velocity contours for Re = 718, 74.5 seconds after starting the transient from zero velocity.	117
4.69	Axial velocity gradient contour with crossplane velocity vectors in front. Re = 718, 74.5 seconds after starting the transient from zero velocity, 760 mm downstream from inlet.	118
4.70	Axial velocity gradient contour with crossplane velocity vectors in front. Re = 718, 74.5 seconds after starting the transient from zero velocity, 800 mm downstream from inlet.	119
4.71	Axial velocity gradient contour with crossplane velocity vectors in front. Re = 718, 74.5 seconds after starting the transient from zero velocity, 840 mm downstream from inlet.	119

4.72	Contour of pressure fluctuations with crossplane velocity vectors in front. Re = 718, 74.5 seconds after starting the transient from zero velocity, 760 mm downstream from inlet.	120
4.73	Contour of pressure fluctuations with crossplane velocity vectors in front. Re = 718, 74.5 seconds after starting the transient from zero velocity, 800 mm downstream from inlet.	121
4.74	Contour of pressure fluctuations with crossplane velocity vectors in front. Re = 718, 74.5 seconds after starting the transient from zero velocity, 840 mm downstream from inlet.	121
4.75	Total velocity contours for Re = 718, 76.5 seconds after starting the transient from zero velocity.	122
4.76	Axial velocity gradient contour with crossplane velocity vectors in front. Re = 718, 76.5 seconds after starting the transient from zero velocity, 870 mm downstream from inlet.	123
4.77	Axial velocity gradient contour with crossplane velocity vectors in front. Re = 718, 76.5 seconds after starting the transient from zero velocity, 910 mm downstream from inlet.	123
4.78	Axial velocity gradient contour with crossplane velocity vectors in front. Re = 718, 76.5 seconds after starting the transient from zero velocity, 950 mm downstream from inlet.	124
4.79	Axial velocity contour with crossplane velocity vectors in front. Re = 718, 76.5 seconds after starting the transient from zero velocity, 870 mm downstream from inlet.	125
4.80	Axial velocity contour with crossplane velocity vectors in front. Re = 718, 76.5 seconds after starting the transient from zero velocity, 910 mm downstream from inlet.	126

4.81	Axial velocity contour with crossplane velocity vectors in front. $Re = 718$, 76.5 seconds after starting the transient from zero velocity, 950 mm downstream from inlet	126
4.82	Contour of pressure fluctuations with crossplane velocity vectors in front. $Re = 718$, 76.5 seconds after starting the transient from zero velocity, 870 mm downstream from inlet.	127
4.83	Contour of pressure fluctuations with crossplane velocity vectors in front. $Re = 718$, 76.5 seconds after starting the transient from zero velocity, 910 mm downstream from inlet.	128
4.84	Contour of pressure fluctuations with crossplane velocity vectors in front. $Re = 718$, 76.5 seconds after starting the transient from zero velocity, 950 mm downstream from inlet.	128
4.85	Maximum and minimum spanwise velocities seen in the entire domain.	129
4.86	Axial velocity contours for purely axial flow.	131
4.87	Averaged axial velocity contours for pulsating flow.	131

List of Symbols

D: Rod diameter [m]

D_H : Hydraulic diameter [m]

k: Turbulent kinetic energy $\left[\frac{J}{kg}\right]$

\dot{m} : Mass flow rate $\left[\frac{kg}{s}\right]$

p: Pressure [Pa]

p' : Fluctuating pressure [Pa]

P: Rod pitch [m]

Re: Reynolds number

S: Gap spacing

St_g : Gap Stanton number

St: Strouhal number

T: Temperature [C]

u : Velocity in spanwise (x) direction $\left[\frac{m}{s}\right]$

U_b : Bulk velocity $\left[\frac{m}{s}\right]$

v : Velocity in transverse (y) direction $\left[\frac{m}{s}\right]$

w : Velocity in axial (z) direction $\left[\frac{m}{s}\right]$

W : Distance between wall and rod centre [m]

x : Spanwise direction [m]

y : Transverse direction [m]

z : Axial or stream-wise direction [m]

δ : Gap spacing [m]

ε : Turbulent dissipation rate $\left[\frac{W}{kg}\right]$

μ : Dynamic viscosity [$Pa.s$]

ρ : Density $\left[\frac{kg}{m^3}\right]$

Chapter 1

Introduction

1.1 Motivation for Research

Experimental and numerical investigation of the fluid flow within nuclear rod bundles is important for nuclear safety analysis. The heat generated by the nuclear chain reaction within the fuel rods is removed by cooling water flowing axially between the rods. If there is an interruption in this flow, this can lead to overheating of the fuel rods and the fission product could be released. A great deal of nuclear safety analysis focuses on mitigating against these accident conditions. These analyses rely on the use of computer codes which use numerical methods to solve the underlying mathematical models for the heat transfer and fluid flow in these geometries. Previous research [1,2,3] has shown that enhanced mixing arising from complex

flows can occur in rod bundle geometries. There is thus a need for models which incorporate a more realistic understanding of the flow conditions so as to produce more accurate results, leading to an increase in efficiency in design and enhanced public safety.

Much of the desire for greater understanding of this phenomenon has come from the Canadian nuclear industry, which generally uses the CANDU reactor for power generation. The CANDU reactor uses a cylindrical rod bundle geometry, with coolant flowing axially along the rods, as discussed above. One of the common rod bundle arrangements can be seen in figure 1.1.

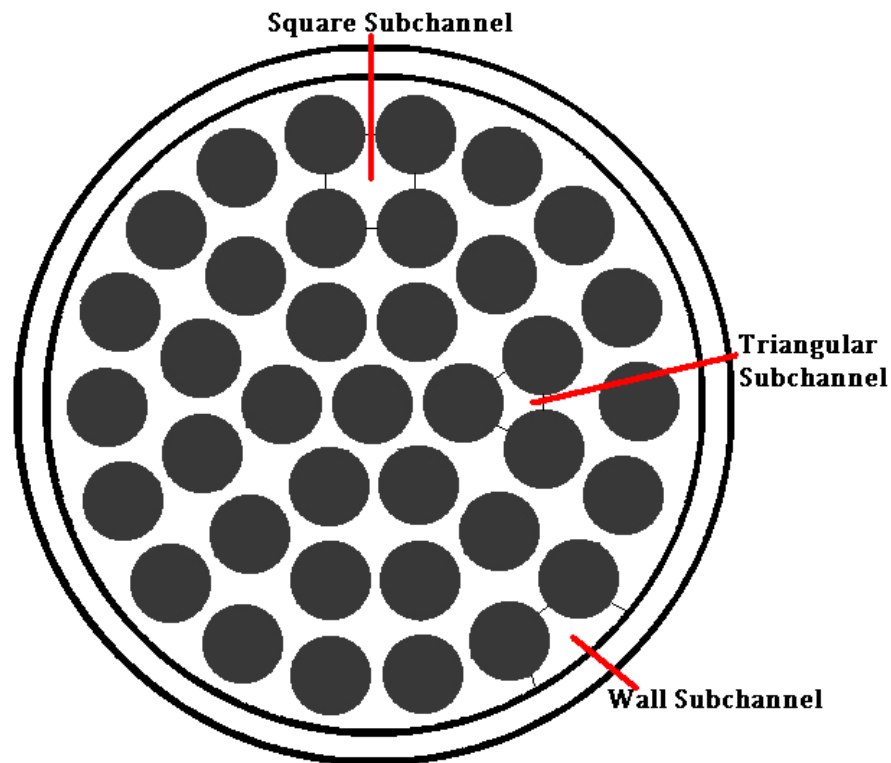


Figure 1.1: Cross-section of a 37 element fuel rod bundle. The rods are represented by gray circles, and the walls of the pressure tube are represented by thick black lines. The main flow direction is into the page. Adapted from Eiff and Lightstone [4].

The positioning of the rods results in a variation in the flow areas between the rods. The larger areas, known as subchannels, are defined as the flow regions surrounded by rod surfaces or the walls of the pressure tube. These flow regions are subdivided from each other by imaginary lines which connect the centroids of adjacent fuel rods. These lines cross through the smaller regions, known as gaps. A gap exists mainly between two rods but also may be defined by the proximity of the rod to the wall of the pressure tube. In figure 1.1, there are three types of subchannels displayed. The first is a square subchannel, formed by four rods. The imaginary lines connecting the centroids of these rods form a square. Similarly, when three rods contain a subchannel, it is called a triangular subchannel. Lastly, a wall subchannel is formed when the wall and two rods form a boundary to a subchannel. In describing subchannel geometry, there are commonly used parameters which aid in non-dimensionalizing the configuration. The diameter of the rod is D , the distance between the centroids of two adjacent rods is the pitch, P . To describe the gaps, the letters S or δ are used to describe the minimum distance between two rods and W is used to describe the minimum distance between a rod and a wall.

The mixing between subchannels occurs in the gaps between the rods (indicated by the thin black lines in figure 1.1), where mass, momentum and heat may be exchanged. The current research focuses on the flow across these gaps. Greater understanding of the mixing process is needed so as to develop more accurate models in nuclear safety analysis codes. These codes are used in large numerical simulations of the reactor systems. The simulations consider heat transport systems, reactor physics, moderator flows, containment, atmosphere dispersion and fuel channel flows. Due to the large size and multidisciplinary nature of the simulations, integrated analysis models are used. As an example of this, the behaviour of the thermalhydraulics is modeled using one-dimensional codes which can predict the pertinent phenomenon reasonably

well, but use empirical correlations and models to calculate the details of the flow, since they are not solved for. Some of the codes employed to calculate the fuel temperatures are: CATHENA [4], TUF [4] and ASSERT-PV [4,5]. Currently, these codes use a large-spatial averaging in conjunction with empirical correlations to account for the higher mixing rates [4,6]. In ASSERT-PV, the averaging is done over an entire subchannel, with details like friction factors, heat transfer, turbulence and boundary layers modeled with constitutive correlations. More accuracy is desired both for better safety analysis as well as more efficient design of reactor cooling.

Investigation into the details of the mixing has been ongoing experimentally for the past fifty years or so [3,7-16], with numerical investigation having been around for the past thirty years [17-24]. The experimental approach has changed somewhat throughout the years. Initially, the analysis was concerned with the effect of subchannel mixing on the mean flow characteristics. Quickly, though, research shifted to trying to find what the cause of the enhanced subchannel mixing was. Until the mid 1980's, it was theorized that secondary flows were the cause of the mixing. At the same time as secondary flows were being investigated, enhanced turbulent transport was thought to be the cause of the mixing. However, it has been shown conclusively that subchannel mixing is a result of periodic motion of large scale structures. The pertinent studies will be discussed in greater detail in chapter 2.

1.2 Objectives of Research

The research objectives are to provide a numerical analysis of a recent laminar experimental investigation of subchannel mixing, using CFD tools to provide insight into the flow complexities. One of the advantages of employing a numerical approach is that once the

computational procedure has been experimentally validated and shown not to depend on the size of grid or timestep, it is able to capture highly detailed information on the transient fluid velocities and pressures. The first step in accomplishing the stated objectives is to select an appropriate experimental study to simulate and use for validation of the numerical results. The details of the selection can be found in section 2.4. The research objectives are summarized below.

1. Simulate the experimental conditions of the experimental study
2. Validate the numerical results by comparing predictions against the available experimental measurements.
3. Provide quantitative and qualitative insight into the complex nature of the pulsations, looking at axial and spanwise velocities, pressures and axial velocity gradients.
4. Analyze how the pulsations form from a mean flow field without any outside disturbance. This will be accomplished by comparing relevant quantities such as velocity magnitudes, pressure differences and velocity gradients. This analysis will start from a state where no pulsations exist, and continue until the pulsations are of a sufficient magnitude for it to be clear that they will grow into the fully evolved state.

1.3 Thesis Structure

After this introduction, the thesis is divided into four chapters. The second chapter is a review of the experimental and numerical studies performed. Experimental studies are broken down into four categories: mean flow, secondary flow, turbulent transport and periodic structures. These categories correspond to different experimental approaches, based on the prevailing theory as to

the cause of the subchannel mixing. The overview of the numerical studies considers Reynolds Averaged Navier Stokes (RANS) analysis and Unsteady Reynolds Averaged Navier Stokes (URANS) analysis, corresponding to use of steady-state or transient equations.

Chapter 3 gives the important details of the experimental study chosen for further investigation, as well as the details of the methodology used in the numerical simulations. A summary of the independence studies conducted is provided as well as details on the advection and temporal discretization schemes chosen.

Chapter 4 looks at the analysis of the results of the research presented. The first part deals with comparing the numerical results with the experimental measurements as well as discussion of the results. The bulk of the results look at various quantities within the pulsing flow to see how pressure, velocities (spanwise and axial) and axial velocity gradient are interconnected in the pulsations. These same quantities will be used to analyze the evolution of flow from a non-pulsing state until the velocities are such that it is apparent they will continue to grow until they are fully evolved.

The thesis concludes with chapter 5, which presents the conclusions of this work, as well as potential future direction from the current research.

Chapter 2

Literature Review

2.1 Introduction

This chapter presents an overview of previous experimental and numerical work on subchannel mixing with the goal of understanding the physical mechanism responsible for the high mixing rates seen in subchannel flows. Results of research into mean flow characteristics, secondary flows, the role of turbulence and periodic structures in these geometries are presented. The geometries, instrumentation and measured quantities of all experimental work presented here are summarized in table 2.1. Table 2.2 presents a summary of the Reynolds Averaged Navier Stokes work, and table 2.3 summarizes the Unsteady Reynolds Averaged Navier Stokes simulations.

2.2 Experimental work

2.2.1 Mean flow Investigation

Eifler and Nijsing [7], using a triangular array, found that there was a change in the local friction factor as they changed the pitch to diameter ratio (P/D). One of their key conclusions stated that analysis of subchannel flows was more complicated than merely using an equivalent hydraulic diameter and assuming the flow would behave similarly to a duct flow.

Van Der Ros and Bogaardt [1] investigated water flowing in square channels and four rods arranged in a square array with a heat flux of 170 W/cm^2 . They observed different mixing trends depending on the Reynolds number and gap size, as shown below in figure 2.1. At Reynolds numbers greater than 17,000, the larger gap size seems to employ a different mixing mechanism than can be found for the rest of the data. At Reynolds numbers below 6,000, a smaller gap size means the mixing rate drops off quite sharply from the trend followed for the larger gap size in the same Reynolds number range. This trend was found roughly to be true for both gap sizes for Reynolds numbers between 6,000 and 17,000.

Yu et. al.[25] ran experiments with air flowing through a subchannel formed by four rods in a diamond array. Their data showed that the relative velocity profile did not greatly depend on the tangential stresses at the walls. From this result, Yu et. al. use the tangential stresses to construct a relationship for the velocity which can be extended to an infinite rod array.

Ouma and Tavoularis [26] conducted experiments on a domain containing five rods, replicating an outer section of a full 37-rod bundle. They demonstrated that in subchannels with a non-constant velocity profile, the subchannel averaging approach taken by Nuclear Safety analysis codes will lead to "appreciable errors". This work was furthered by Guellouz and

Tavoularis [2] in 1992. They looked at heat transfer aspects, finding that for narrow gaps, which can be said to have similar P/D ratios to many typical rod bundles, the heat transfer coefficient is very sensitive to gap size.

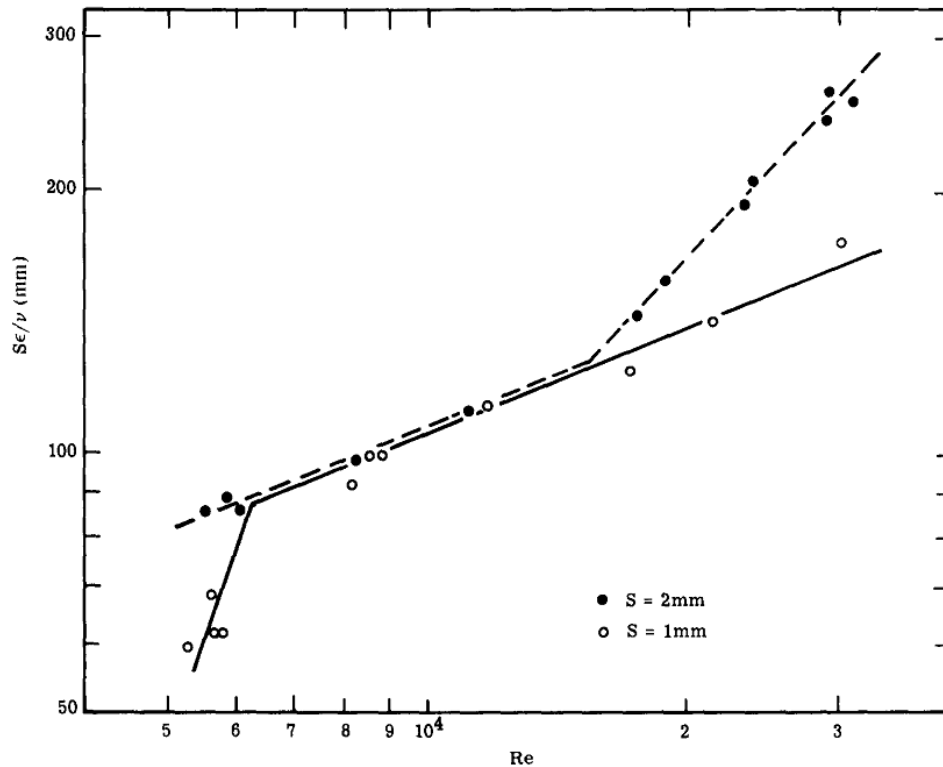


Figure 2.2: Mixing Coefficient vs. Reynolds number, taken from Van Der Ros and Bogaardt [3]. The s value represents different gap sizes

2.2.2 Secondary Flow Investigation

One of the theories proposed as to the cause of the increased mixing was that of secondary flows. These are spanwise flows caused by Reynolds stresses and are typically found in the corners of rectangular ducts. These flows would increase the mass transfer through the subchannel and therefore increase the amount of mixing seen in a duct geometry containing a subchannel. There is no inherent pulsatile nature to these flows.

Gessner and Jones [27], in 1965, conducted experiments in a rectangular channel that did not contain any subchannel geometry. Their results showed that when the secondary flow velocities were non-dimensionalized with the bulk velocity, they decreased as the Reynolds number increased. The source of the secondary flows are the differences between the magnitudes of Reynolds stresses and static pressure gradients. Wall shear stress skewness is at a maximum in the corners and surrounding area.

Skinner et. al. [28] conducted experiments designed to investigate possible magnitudes of secondary flows in rod bundles. They used a rod bundle containing six rods inside a pipe with a circular cross section, with one set of experiments using "smooth" rods, and one set using "rough" rods. The "rough" rods were made by running ribs of height 0.015 inches down a rod with a diameter of 0.5 inches. They state that secondary flows of approximately two percent of the centreline mean velocity would suffice to account for the mixing rate found in a smooth rod cluster, with the magnitude rising to six percent for a rough rod cluster. The smooth rod value is in agreement with contemporary data for secondary flows in pipe flows. The rough cluster value is higher than would be expected in smooth clusters, but is in agreement with data passed along in a private communication from Hanjalic and Launder in 1968.

Tachibana et. al. [29] used two different domains for their experimental results. One was an eccentric annulus, the other a cluster containing seven rods - a central rod, and six evenly spaced rods around it. Their data was found to correspond well with contemporary heat transfer correlations and in the case of the seven rod cluster, they found a sinusoidal circumferential variation, which was taken to imply the presence of secondary flows around all the rods. They conclude that to account for this periodicity, greater emphasis should be placed on the secondary flows as well as anisotropy in the eddy conductivity .

Rowe et. al. found similar periodicity in their experimental work, published in 1974[8]. Their domain was a square array, with pitch to diameter ratios of 1.25 and 1.125. They only observed periodic pulsations for their smaller rod spacing indirectly, through some of their autocorrelation functions. They also noted that any area where pulsatile behaviour was observed, secondary flows were present. Rowe et. al. also found that a weak dependence between rod spacing and crossflow mixing as well as between Reynolds number and turbulence intensity.

Trupp and Azad [30] investigated triangular array rod bundles with pitch to diameter ratios of 1.20, 1.35 and 1.50. The secondary flows they found had magnitudes of less than 0.5% of the mean bulk velocity. For the pitch to diameter ratio of 1.35, they found that the secondary flows were smaller than for the other P/D ratios (1.20 and 1.50) and were unable to posit an explanation as to why this was true. They found that for the largest P/D ratio of 1.50, the effectiveness of secondary flows increases as Reynolds number decreases.

Carajilescov and Todreas [17] analyzed a subchannel formed by four rods in a triangular array setup. They used laser doppler anemometry to measure velocities, turbulence intensities and pressure drop and despite the potential scattering introduced by having curved surfaces, found a technique which worked well to obtain quality data. Their secondary flow predictions were found to agree with their predictions of the wall shear stress distribution.

Melling and Whitelaw [31] looked at flow in a rectangular duct, in an attempt better to understand measurement devices and techniques as well as to gain insight into turbulence modeling, particularly with secondary flows. They found that data on all three mean velocities and all Reynolds stresses in the developing region is very important for prediction of turbulent

flows. They concluded that the approach defined by Launder in 1975 is likely to lead to an optimum turbulence model for non-circular duct flows.

Similarly to Melling and Whitelaw [31], Aly et. al. [32] looked at flow in a triangular duct, with no rods inside. The wall shear stress in the centre of each wall was found to be nearly constant. This result was said to be due to secondary flows. They found that the Launder-Ying model for secondary flow analysis was a valuable asset to solving flow and heat transfer patterns in the life size fuel bundles.

Seale published results [33] from an experimental setup consisting of two rods within a rectangular duct such that two interconnected subchannels were created. He found friction factors were 2% lower than would be expected for a smooth axisymmetric duct. He defined laws of the wall for the direction normal to the flat wall and radial from the curved walls for y^+ up to 1500. Seale also measured secondary velocities and found a maximum of 1.5% of the mean axial velocity to exist near the corners of the duct.

Renksizbulut and Hadaller [11] published experimental results for six rods arranged in three rows with two columns, with water at 80 C as the working fluid. They found that the gap size did not significantly affect the turbulent mixing. Secondary flows were found to be most prevalent in the corner subchannels, and almost non-existent in the wall and central subchannels. The results for turbulence and velocity intensity profiles within the central subchannels are found to be identical to those previously observed in pipe flows. However, higher intensities exist in the wall and corner subchannels. The intensity profiles both show a peak within the central subchannels and a relative minimum within the gap region.

Vonka [34] performed experiments with a mixture of diethyl ether and toluene running in four rods arranged in a triangular array. This geometry meant he captured two triangular subchannels. The fluid was chosen because it has the same index of refraction as glass. It was found that if the secondary vortex velocities are non-dimensionalized with the friction velocity, they become independent of Reynolds number - in this experiment, Reynolds number ranged between 60,000 and 175,000. It was also found that the profiles of the secondary flow velocities had a similar shape for the different Reynolds numbers. These secondary flow vortices have an average tangential velocity which is a little bit less than 0.1% of the bulk mean velocity.

A year later, Vonka [35] continued the work started in his previous paper [34]. The issue inherently raised previously [34] is addressed immediately - that despite the secondary flow vortices being so weak, they can still play a role as a transport mechanism responsible for momentum transport in rod bundle flows. The reason for the apparently weak flow contributing so much stems from the observation that there are two transports in opposite directions. Vonka averaged each directional transport separately. From this, he posits that the rate of axial momentum transport due to secondary flows is approximately 30% to 50% of the total transport when the secondary flows are normalized by wall shear stress.

Wu and Trupp [36] looked at flow in a trapezoidal duct with a moveable central rod. They found that secondary flows are sufficient to explain axial momentum transport within the subchannel but cannot explain the transport across the gap. Figure 2.2 supports their conclusion, as the secondary flows can be seen within the subchannel, but no flow loops are in the gap region. From their spectral analysis, they proposed that the transport between subchannels and thus through the gap is due to large scale eddy motion which has a frequency defined by geometry and flow parameters.

Further work on the same geometry by Wu and Trupp [37] showed that by looking at conservation of mass, secondary flows in the cross section of the subchannel areas are not constrained to stay in a particular subchannel. However, the authors recognized the need for experimental and numerical evidence to support this theoretical hypothesis. They also see that the cross-gap large scale eddy motion exists without too much dependence on the shape of the subchannel, and the details of that periodicity are dependent on the subchannel geometry.

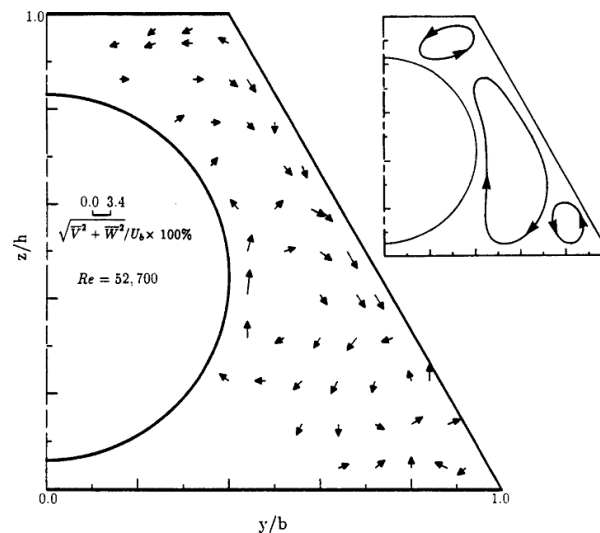


Figure 2.3: Secondary flows measured by a x-probe, with the flow direction stylized in the image in the top left. Adapted from Wu and Trupp[36].

2.2.3 Turbulent Transport Investigation

In addition to secondary flows, it was also proposed that enhanced turbulence transport may be responsible for increased mixing in subchannel geometries. This mechanism, like secondary flows, does not involve a periodic nature to the cross flow.

Castellana et. al. [38] investigated water flowing in a 5 x 5 square array of unequally heated rods. Their analysis of experimental results found no real correlation between a turbulent mixing coefficient and Reynolds number.

Rehme [9] ran an experiment with air in a rectangular duct containing four parallel rods. For the first time, detailed data was found for eddy viscosities parallel to the walls in rod bundle geometries. It was found that momentum transport in rod bundles has a high degree of anisotropy, with the highest factors found in the gaps. From the axial velocity contours, reproduced below in Figure 2.3, Rehme could detect no sign of secondary flows from this velocity distribution

Seale [39], like Rehme [9] used an experimental domain consisting of rectangular ducts with parallel rods. He used three, four and five rods so as to give different pitch to diameter ratios with air as the working fluid. His data affirmed that subchannel mixing is higher than traditional turbulent mixing would allow. Seale also confirmed that the mixing flow rate does not change much with gap width. He found that decreasing the gap width greatly increased the degree of anisotropy - factors increased tenfold between the largest gap ($P/D = 1.833$) and the smallest gap ($P/D = 1.1$).

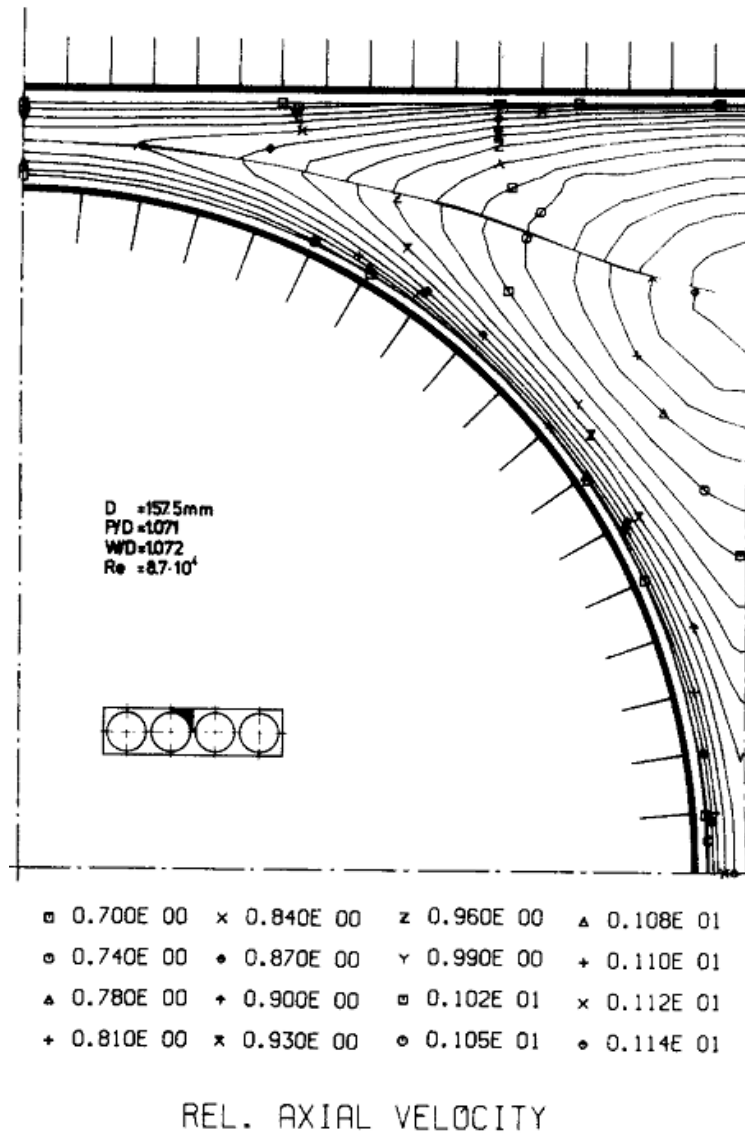


Figure 2.4: Contours of axial velocity, non-dimensionalized by a reference velocity of 27.74 m/s. Adapted from Rehme [9].

Hooper [40] published results from a square array containing six rods, with two different gap spacings used - $P/D = 1.194$ and 1.107 . He found that, as expected, the turbulent flow structure in the rod-gap region is very different from the structure expected for pipe flow. This difference is accentuated for the angular turbulent shear stress in a cylindrical coordinate system. Also, the turbulent kinetic energy was found to increase for the smaller gap size.

Rehme [41], used the same geometry as in [9], but with a wider range of Reynolds numbers and gap sizes. He found discrepancies when trying to validate the VELASCO code with his results, attributing the differences to the isotropic assumptions the code makes, specifically about the circumferential eddy viscosity. He recognized that the distributions of the mean velocity and wall shear stress are not greatly affected by secondary flows, at least not as much as other contemporary experimentalists had thought. Rehme found the axial turbulence intensity and kinetic energy exhibited characteristics consistent with secondary flows, especially in the wall and corner subchannels with a small gap size ($P/D = 1.07$).

Meyer [42] investigated a heated 37-rod bundle with air as the working fluid and a pitch to diameter ratio of 1.12. Measurements were taken within a central triangular subchannel. In all comparable quantities, he found little difference between the heated and unheated cases. The calculated wall shear stress reached a plateau as it reached the symmetry line of the channel, which was also found in the wall temperature distribution. He observed that the angular and radial velocity intensities in the central channel vary less according to angular position than has been found in similar wall channels. A decreased turbulent heat flux in the radial direction was found than would typically be expected in pipe flow.

2.2.4 Periodic Structures Investigation

Hooper and Rehme [10] investigated two different experimental domains. One was a rectangular duct with four parallel rods, the other was two connected subchannels formed from six rods arranged in a square array. They found a periodic velocity component which flowed through the gap, which had no relationship to any secondary flow velocities. They discounted the following mechanisms for the subchannel mixing: rod vibration, vortex shedding from spacer pins, acoustic

resonance in the test section and a large scale structure being present in the fluid before entering the test section. Instead, they see intersubchannel instability as the driving mechanism. A year later, Rehme [43] concluded, based on experiments on a geometry of four parallel rods in a rectangular duct with air as the working fluid, that "It is necessary to investigate this pulsating flow in more detail."

Wu and Rehme [44], continued to use the same basic geometrical approach that Rehme had been using for previous papers [9,41]. They used a P/D ratio of 1.148, and two wall to diameter ratios - 1.045 and 1.074. From a number of their results, it was concluded that the higher amounts of axial turbulence intensity are dependent only on the gap geometry. They again found that the VELASCO code is not a robust enough predictor of the flow in rod bundles, mainly because the code does not model the interchannel momentum transport as cyclical.

Möller [12] considered a geometry similar to Rehme [9,41,43], using air as the working fluid. The wall to diameter ratios ranged from 1.045 to 1.223 and the pitch to diameter ratios ranged from 1.007 to 1.224. He demonstrated that the pulsations which are behind the intersubchannel exchange of mass and momentum have a frequency which has a dependency on the gap geometry, specifically the dimensionless distance between the rods. These pulsations are correlated to large eddy motion through the gap. Subsequently, Möller[45] calculated mixing factors from a range of experiments. He showed that the mixing factor decreases with an increase in the dimensionless gap width. However, he does say that further investigation into Reynolds number dependency is needed, given that some assumptions were made in the calculation of the mixing factor around the trend with Reynolds number.

Meyer and Rehme [46] investigated air flowing through rectangular ducts connected by a thin rectangular gap, with pitch to diameter ratios ranging from 1.065 to 1.25. They observed a "strong large-scale quasi-periodic flow oscillation" in most of the geometrical configurations they ran experiments on. They found a frequency of these oscillations to depend linearly on Reynolds number, increasing as Reynolds number increases. However, when the frequency was non-dimensionalized with the square root of gap size multiplied by rod diameter, the Strouhal number showed no variance with Reynolds number, only on the geometry of the gap. The Strouhal number is defined as: $Str = \frac{fD}{U_b}$, where f is the frequency of pulsations, D is the rod diameter and U_b is the bulk velocity. Both these trends can be seen in Figure 2.4. They also found that the Reynolds shear stresses reach a maximum near the gap which is much greater than levels found elsewhere in the flow regime.

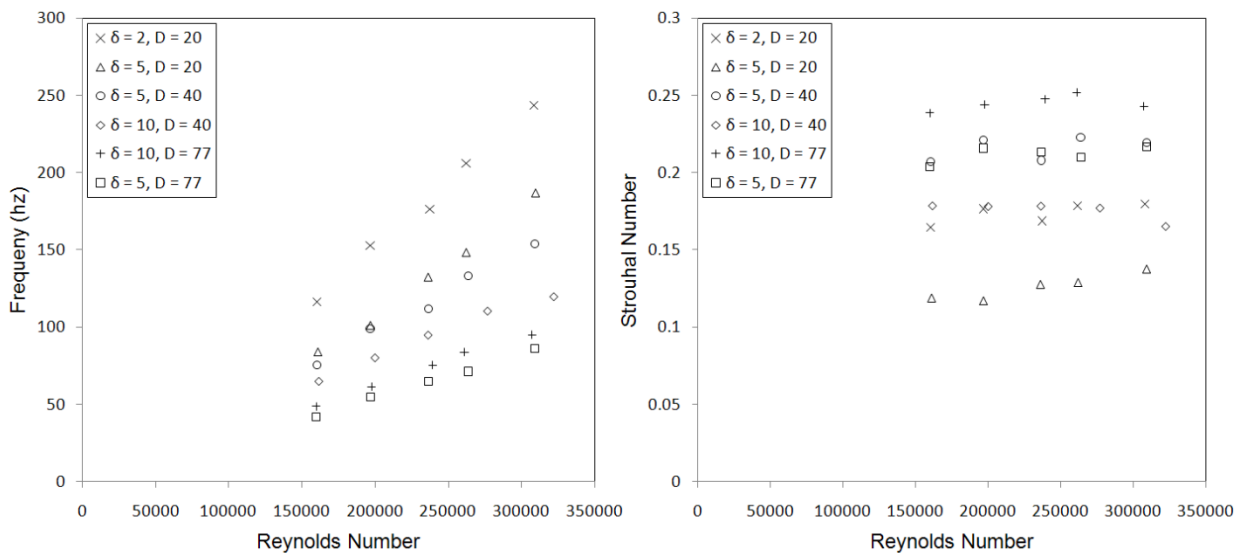


Figure 2.5: Reynolds number vs Frequency and Strouhal number. The gap size is represented by δ , and the gap width is represented by D . The data was taken from Meyer and Rehme [46] and adapted to show the trends against Reynolds number.

Wu [47] used the same experimental domain found in the previous experimental work of Wu and Trupp [36,37], a moveable rod within a trapezoidal duct. He used wall to diameter ratios of 1.22 and 1.079, placing the rod in an asymmetric arrangement. The Reynolds number was 26,300, with air at atmospheric conditions used as the working fluid. Wu found that the magnitude of the pulsations are dependent on the geometry of the subchannel and gap. Based on the wall shear stress and turbulent kinetic energy distributions he concludes that secondary flows are an important part of the analysis of subchannel mixing. This statement contradicts his results which demonstrate the key role played by large scale eddy motion in transport across the gap.

Kraus and Meyer [48] analyzed a full 37 rod bundle having a wall to diameter ratio of 1.06 and a pitch to diameter ratio of 1.12. This experimental setup used heated air at a Reynolds number of 65,000, with most of the measurements being taken in and around a wall subchannel. Kraus and Meyer found the same velocity and wall shear stress distributions as was found previously for isothermal flow. They again found the existence of quasi periodic pulsations, as evidenced by characteristic frequencies being found in the turbulent velocity and temperature fluctuations. Within the wall subchannel, they found that the axial and angular velocity fluctuations are higher and have greater dependency on angular position than in more central channels. Similarly, the fluctuations of the turbulent temperature were found to be larger than values found in central subchannels.

Guellouz and Tavoularis looked at a rectangular channel containing a rod, with data and analysis divided into two parts. Part one [14] looked at Reynolds-averaged measurements and part two [15] looked at phase averaged measurements. The working fluid for the experiments was air, with a Reynolds number equal to 108,000, and wall to diameter ratios ranging from 1.00 to 1.25. Their simple geometry yielded results which clearly show coherent structures forming

and interacting as a part of the periodic pulsations. They conclude, in the first part [14], that the structures arise not from the asymmetry of subchannels, as has been stated previously but instead as a fundamental part of the flow instability in subchannel/gap geometries. They also found empirical relationships for the speed and spacing of the structures, which are not meant to apply to rod bundles but as a method of quantifying the phenomenon. In the second part [15] of their paper they examined the structures in detail, finding that the vortices remain together for a relatively long period of time. The formation of the structures is hypothesized to be linked to the "quasi-two-dimensional vortices" that are found in mixing layers, both laminar and turbulent. Guellouz and Tavoularis go on to say that this explanation from mixing layers does not account for the subchannel mixing. They theorize that subchannel mixing is a result of a pattern very similar to von Karman vortex shedding, with the spacing of the vortices across the gap such that they reinforce each other.

Silin et. al. [49] looked at three rods arranged in a triangular array, $P/D = 1.33$, contained within a pipe. One of the rods contained a heating strip, with the heating power inputs of 300 watts, 745 watts and 755 watts. Their working fluid was water, with Reynolds numbers of 10,000, 35 000 and 68 000. The use of the heat transfer was as a tracer so that the mixing could be quantified - this data was non-dimensionalized using the Stanton number. They concluded that the gap Stanton number does not depend on the Reynolds number, which agrees with previous work.

In 2005, for the first time, work was published showing that subchannel mixing occurred under laminar conditions. Lexmond et. al. [50] used a simplified subchannel geometry which contained pulsations under laminar and turbulent conditions. Their domain consisted of two rectangular ducts, connected at the top by a thin rectangular gap. This resembles that of Meyer

and Rehme [46], split in two horizontally. The working fluid is water, with Reynolds numbers, based on the hydraulic diameter, ranging from 320 to 10,000. They estimated mass transfer by injecting a solution of 50% acetic acid into one channel, with the other channel having water. Their results show that above a Reynolds number of about 2,000, there is little change in structure size - a standard deviation of about 25% was calculated for the structure size. The amount of mass transferred from one subchannel to another was about 10% for a Reynolds number of 2,000, to a maximum of about 70% for a Reynolds number of 8,000. They also found that cross flow and vortices contributed to the formation of coherent structures at Reynolds numbers above 800. Above a Reynolds number of 3,000, the structure velocity was measured to be about 79% of the superficial velocity, which is much greater than the measured average gap fluid velocity. As Reynolds number increases, so does the gap velocity, whereas the structure velocity remains constant.

The domain used by Ouma and Tavoularis [26] and Guellouz and Tavoularis [2] was used by Baratto et. al. [51] to investigate the spatial correlations of coherent structures in gap flow. They varied the rod to wall thickness ratio (W/D) from 1.02 to 1.30. The frequency of the circumferential velocity increased as W/D increased from 1.02 to 1.25, but decreased again when W/D increased to 1.30. From this trend, and previous work [14,15], Baratto et. al. conclude that the frequency is dependent on the overall geometry of the duct as well as the gap size.

Silin and Juanicó [52] utilized the same geometry as their previous work [49], with a different pitch to diameter ratio of 1.196. Their Reynolds numbers ranged from 1,400 to 130,000, with flow temperatures of 25 and 65 degrees Celsius. They found an increase in mixing rate at the lower Reynolds numbers - their Stanton number for $Re = 1,400$ is approximately five times their Stanton number for $Re = 2,000$. They also found that as Reynolds

number increases, the mixing rate, characterized by the Stanton number, decreases. The Stanton number is defined as: $St_g = \frac{Nu}{RePr}$. Silin and Juanicó did not find a change in Stanton number for the different flow temperatures.

Gosset and Tavoularis [53] demonstrated that, under laminar conditions, flow pulsations occur in subchannel geometries. Their domain had the same dimensionless ratios as the previous papers [14,15] released by Guellouz and Tavoularis, but smaller actual dimensions. The working fluid was water, with Reynolds numbers ranging from 388 to 2,223. The dimensionless gap size ranged from 0.025 to 0.7. To visualize the flow, they injected dye into the centre of the gap - this allowed them to obtain an estimate of the frequency and wavelength of the pulsations. This is the first time that frequency data was estimated for laminar pulsations in subchannel geometries. A plot was made by Gosset and Tavoularis of the dimensionless frequency, or Strouhal number, estimated for each Reynolds number, which can be found below as figure 2.5. Given that this data is laminar, Gosset and Tavoularis were able to observe a critical Reynolds number, below which pulsations cannot be observed since at low Reynolds number the viscous shear (i.e., friction) will dominate over inertia. As such, the inertial forces will not be strong enough to push the fluid through the gap, thus no pulsations will be seen. Gosset and Tavoularis conclude that their laminar data is good evidence for the driving force of the pulsations being related to vortex shedding, as stated in the previous work of Guellouz and Tavoularis [14,15]. This shows that the pulsations cannot be a purely turbulence based phenomenon.

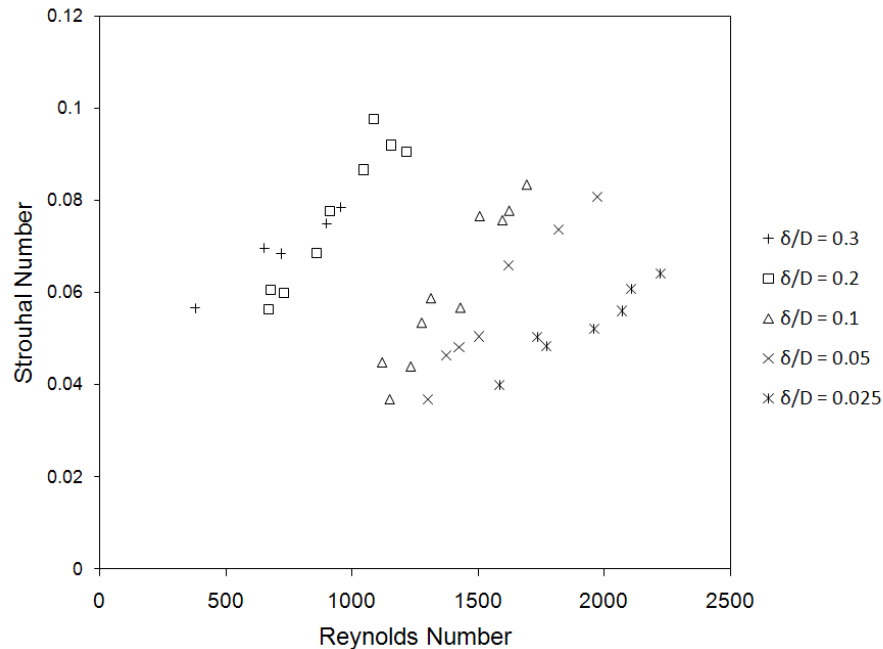


Figure 2.6: Reynolds number vs Strouhal number. The gap size is represented by δ , and the gap width is represented by D . Adapted from Gosset and Tavoularis [53].

Mahmood et. al. [54] used an experimental domain of two rectangular ducts connected by a wall with a semi-circle to create a curved wall gap. A subset of their results were in the laminar regime, but most of the data published is turbulent. Their working fluid was water, with Reynolds numbers ranging from 850 to 21,000, with minimum pitch to diameter ratios of 1.14 and 1.09. They performed another set of experiments at a Reynolds number of 10,000, looking at the variation in gap height, with pitch to diameter ratios ranging from 2.11 to 1.05. They measured inter-channel mass transfer by injection of a tracer solution, sodium chloride, into one of the channels, while water was injected into the other. The impedance of the fluid exiting each channel was measured so as to calculate the concentration of sodium chloride and thus the mass transfer. They found that mass transfer increases from their lowest Reynolds numbers until Reynolds numbers of about 7,000, at which point, it roughly plateaus. The smaller gap size resulted in a decrease in the mass transfer between the channels and an increase in the spanwise

velocity fluctuations. Coherent structures were observed to form in the gap region and these structures increase the mixing from that found from turbulent mixing by a factor of 63%.

Piot and Tavoularis looked at laminar flow instability in eccentric annuli [16]. They had water flowing at Reynolds numbers between 320 and 1,420, with the eccentricity of the annuli ranging from 0 to 0.8. The eccentricity is defined as one minus twice the gap thickness divided by the diameter difference. To visualize the flow, and obtain results for the frequency, Piot and Tavoularis injected dye into the gap. They found that there are two different mechanisms for instability in annular flows. The one which is of greater interest to subchannel mixing arises in narrow gaps, coming from two unstable shear layers which form on either side of the gap.

Table 2.1: Summary of Experimental Investigations

Investigators	Geometry	Reynolds Number	Fluid	Measured Data	Measurement Method
Gessner and Jones (1965)	Rectangular duct	50,000 - 300,000	Room temperature air	Velocity Secondary Flow velocities Reynolds stresses	Total head tube Single-wire rotation method X-wire array
Eifler and Nijssing (1966)	Triangular Array, P/D = 1.05 - 1.15	15,000 - 50,000	Water, 20 C - 80 C	Velocity Pressure Drop	Probe, manometer U-tube manometer
Skinner, Freeman and Lyall (1969)	Six 1.35" rods in 3.625" tube, equally spaced, with 0.5" tube in centre	20,000 - 80,000	Air	Velocity Pressure (static/differential)	Pitot Static probes Pitot static probes
Tachibama, Oyama, Akiyama and Kondo (1969)	Seven rod cluster, P/D = 1.125	8,000 - 45,000	Air at 45 C	Local and average heat transfer factors	Naphthalene sublimation
Van Der Ros and Bogaardt (1970)	Low Pressure: Compound square channels High Pressure: Four rods in square duct, P/D = 1.33	5,000 - 30,000 76,000 130,000 270,000	Water, 20 C - 50 C Water, with 170 W/cm ²	Pressure, multiple locations Velocity Temperature	Manometers Pitot tubes Chromelalumel thermocouples
Levchenko, Subbotin and Ushakov (1973)	Four rods in a diamond arrangement, P/D = 1.05, 1.1, 1.15	15,000 - 115,000	Air	Local velocities Static pressure	Pitot glass tubes Manometers
Castella, Adams and Casterline (1974)	25 rod square array, P/D = 1.33	90,000 - 289,000	Water	Temperature	Thermometers, accuracy: ± 0.30 F

Rowe, Johnson and Knudsen (1974)	Square array, focusing on: side, interior and corner subchannels, P/D = 1.125, 1.25	50,000 - 200,000	Water	Axial Velocity Turbulence intensity Eulerian autocorrelation function	Laser Doppler velocimetry Laser Doppler velocimetry Fluctuating velocity & signal correlator
Trupp and Azad (1975)	Triangular arrays, P/D = 1.20, 1.35, 1.50	12,000 - 84,000	Air	Wall shear stresses (local) Mean axial velocity Reynolds stresses Eddy Diffusivities	Pitot tube/subminiature flush-mounting probe/anemometer Pitot tube, static pressure probe, differential pressure manometer Linearized constant temperature anemometry
Melling and Whitelaw (1976)	Square duct, 40 mm x 41 mm x 1.8 m	42,000	Water	Mean velocities Turbulence intensity Reynolds stresses	Laser doppler anemometer
Carajilescov and Todreas (1976)	Triangular array, P/D = 1.12	27,000	Water	Axial Velocity distribution Turbulent kinetic energy Reynolds stresses Pressure Drop	Laser Doppler anemometer
Aly, Trupp and Gerrard (1978)	Equilateral triangular duct, 12.7 cm sides	53,000 - 107,000	Air	Mean Axial velocity Wall shear stress Axial velocity fluctuations Secondary velocities Turbulent Kinetic energy	Pitot Tubes Pitot Tubes Single-wire probe Miniature X-array probe Hot-wire anemometry
Rehme (1978)	Wall subchannel in a bundle of four parallel rods, P/D = 1.071, W/D = 1.072	87,000	Air	Time-mean velocity Turbulence intensities Turbulence kinetic energy Shear stresses normal and parallel to the walls Wall shear stress	Pitot Tubes Hot wire measurements/DISA Hot wire measurements/DISA Hot wire measurements Preston Tubes
Seale (1979)	Three (P/D = 1.833), four (P/D = 1.375) and five (P/D = 1.1)	3-Rod: 34,369 - 299,603	Heated Air	Detailed velocity and temperature distributions	Velocity: Pitot-temperature probe Temperature: Calibrated thermocouple

	rod assemblies (row)	4-Rod: 45,870 - 189,500 5-Rod: 46,920 - 91,120			
Rehme (1980)	Wall and corner subchannels in a rod bundle of four parallel rods, P/D = 1.07 - 1.4	60,000 - 200,000	Air	Mean fluid velocity Turbulent shear stresses Distribution of turbulent intensity Distribution of the wall shear stress	Pitot Tubes Hot wire measurements Hot wire measurements/DISA Preston Tubes
Hooper (1980)	Square Pitch, P/D = 1.194, 1.107	48,000 - 156,000	Air	Mean Velocity distribution Wall shear Reynolds Stress Tensor	Pitot Tubes Preston Tubes Hot-wire anemometry
Rehme (1982)	Four asymmetrically arranged rods in a rectangular duct. Main subchannel: P/D = 1.072, wall subchannels: P/D = 1.048, 1.096	75,700 - 106,800, depending on D_H of channel	Air	Mean velocity Turbulent shear stress Turbulent intensity, turbulent k energy Wall shear stresses	Pitot tubes Hot wire measurements Hot wire measurements Preston tubes
Seale (1982)	Two interconnected rod subchannels, P/D = 1.20	82,800 - 346,700	Air	Pressure Gradient Axial Velocities Wall Shear Stresses Secondary Velocities Reynolds stresses	Pitot Tube Pitot Tube Pitot Tube/hot-wire anemometer
Hooper and Rehme (1984)	Four rods in rectangular duct, with P/D = 1.026, 1.036, 1.048, 1.072, 1.096, 1.118	54,600 - 105,000 22,600 - 207,600	Air	Mean velocity Reynolds stresses Turbulence intensities Wall shear stress	Pitot tube Normal/slant wire DISA hot wire anemometer Preston tubes

	Six rods in square array, $P/D = 1.107$				
Renksizbulut and Hadaller (1986)	Square pitch, $P/D = 1.15$, $W/D = 0.62$	500,000	Water, 80 C	Wall shear stress Mean axial velocity Turbulence intensity	Preston Tubes Laser Doppler Velocimetry
Rehme (1987)	Four parallel rods in a rectangular channel, $P/D = 1.148$	117,000		Mean velocity Wall shear stress Reynolds stresses	Pitot tubes Preston tubes Normal/slanting hot wires
Vonka (1987)	Four rods, triangularly arranged, $P/D = 1.3$	60,000 - 175,000	Diethyl ether/toluene mixture	Velocity vectors Secondary flow vortices	Laser Doppler anemometry
Vonka (1988)	Four rods, triangularly arranged, $P/D = 1.3$	60,000 - 175,000	Diethyl ether/toluene mixture	Velocity vectors Secondary flow vortices	Laser Doppler anemometry
Rehme (1989)	Four rod row, $P/D = 1.036 - 1.40$, $W/D = 1.026 - 1.40$	61,100 - 119,000	Air	Time-mean velocity vectors Wall shear stresses Full Reynolds stress tensor	DISA constant temp anemometer bridge Preston tube DISA hot-wire anemometers
Wu and Rehme (1990)	Four parallel rods, with $P/D = 1.148$, and $W/D = 1.045, 1.074$	61,100 70,700	Air	Mean axial velocity Wall shear stress Reynolds stresses	Pitot tubes Preston tubes Normal/slanting hot wires
Ouma and Tavoularis (1991)	5 rods, meant to mimic the outer segment of a 37-rod bundle, with $P/D = 1.15$, $W/D = 1.00$ to 1.15	48,000	Air	Wall static pressure Wall shear stress Mean velocity Turbulence 'parameters' (R stresses, turbulence scales)	Pressure holes Preston tubes Pitot tubes Cross wire probes
Guellouz and Tavoularis (1991)	5 rods, meant to mimic the outer segment of a 37-rod bundle, with $P/D = 1.15$	48,000	Air	Wall temperature Fluctuating air temperature Wall shear stress Mean velocity	Thermistors Resistance thermometer Preston tubes Pitot tubes

Möller (1991)	Four parallel rods in a rectangular channel, P/D = 1.007 - 1.224, W/D = 1.045 - 1.223	85,000	Air	Mean velocity Wall shear stress Reynolds stresses Turbulence intensities Fluctuating velocities Wall pressure fluctuations Power spectra	Pitot tubes Preston tubes Constant temp anemometers Normal/slanting hot wire Double hot wire probes Condenser microphone Microphones/hot wires
Möller (1992)	Four parallel rods in a rectangular channel, P/D = 1.007 - 1.224, W/D = 1.045 - 1.223	74,200	Air	Mean velocity Wall shear stress Reynolds stresses Turbulence intensities Fluctuating velocities Wall pressure fluctuations	Pitot tubes Preston tubes Constant temp anemometers Normal/slanting hot wire Double hot wire probes Condenser microphone
Wu and Trupp (1993)	Trapezoidal duct with rod, W/D = 1.020 - 1.220	21,300 - 55,200	Air	Mean Axial velocity Local wall shear stress Turbulence intensity Secondary flows	Pitot Tube Preston Tube Hot-wire anemometry X-wire probe
Wu and Trupp (1994)	Trapezoidal duct with rod, W/D = 1.039 - 1.240	21,300 - 52,700	Air	Power spectral density Fluctuating velocities	X-wire probe
Meyer (1994)	Triangular array, 37 rod bundle in symmetric hexagonal channel, P/D = 1.12, W/D = 1.06	66,500, 71,500	Heated air	Mean velocity Mean temperature Wall shear stresses Wall temperature Turbulent kinetic energy Reynolds stresses Turbulent heat fluxes	Pitot Tube Sheathed Thermocouples Preston Tube Infrared pyrometer Hot wire anemometry with three wire probe
Meyer and Rehme (1994)	Compound Rectangular channels, gap height 1.80 - 10.00 mm, subchannels roughly the same width	Data given for 250,000	Air	Axial mean velocity Wall shear stresses Reynolds stresses (5 of 6) Auto and cross spectral densities	Pitot Tube Preston Tube Hot-wire anemometry, x-wire probe Fluctuating velocities + FFT

Wu (1995)	Rod asymmetrically mounted in a trapezoidal duct. Large gap size: $P/D = 1.22$, smaller gap: $1.039 - 1.079$	26,300	Atmospheric air	Mean Axial velocity Local wall shear stress Turbulence intensity	Pitot Tube Preston Tube Hot-wire anemometry
Krauss and Meyer (1996)	Wall Subchannel within 37 rod bundle, $P/D = 1.12$, $W/D = 1.06$	65,000	Heated air	Mean velocity Mean temperature Wall shear stresses Wall temperature Turbulent kinetic energy Reynolds stresses Turbulent heat flux	Pitot Tube Sheathed Thermocouples Preston Tube Infrared pyrometer Hot wire anemometry with three wire probe
Guellouz and Tavoularis (2000)	Rectangle ($2d \times 3d$) with rod ($d = 101$ mm), $W/D = 1.025 - 1.35$	108,000	Air	Wall shear stress Mean Velocity Turbulent stresses Velocity fluctuations	Preston Tubes Hot wire probes (three sensor) Preston Tubes Hot-wire three sensor probe
Sillin, Juanicó, Delmastro (2004)	Triangular array, $P/D = 1.33$, heated strip on one rod	10,000 - 68,000	Water	Temperature Applied current/voltage	1 mm diameter resistance thermometers Input data
Baratto, Bailey and Tavoularis (2006)	5 rods, meant to mimic the outer segment of a 37-rod bundle, with $P/D = 1.15$, $W/D = 1.00$ to 1.15	42,000	Air	Wall shear stress Mean Velocity Turbulent stresses Velocity fluctuations	Preston Tubes Hot wire probes (three sensor) Preston Tubes Hot-wire three sensor probe
Lexmond, 2005	Small gap connecting two subchannels	800 - 10,000	Water	Velocity Field Mass transfer between subchannels Coherent structure visualization	2D particle image velocimetry 50% acetic acid in one subchannel Velocity vectors viewed from top-down view, shading to help visualization

Silin and Juanicó (2006)	Triangular array, $P/D = 1.2$, $d = 10$ mm	1,400 - 130,000	Water	Total Flow rate Heating power Temperature difference between two points	Input data 1 mm diameter thermometers
Gosset and Tavoularis (2006)	Rectangular channel with rod, small gap (δ) $\delta/D = 0.025 - 0.70$	388 - 2,223	Water	Dye injection to visualize flow instabilities	Dye Injection
Chang, Choo, Moon and Song (2007)	5x5 square array, $P/D = 1.31$	49,000	Water at 35 C	Cross flow velocity	PIV and LDV measurements
Chang, Moon, Baek and Chung (2008)	5x5 Rod bundle array, $P/D = 1.31$	50,000	Water	Velocity vectors and streamlines	LDA
Mahmood (2009)	Subchannels connected by a small gap	850 - 21,000	Water	Time averaged velocity Structure velocity Inter-channel mass transfer	2D particle image velocimetry Time lapsed PIV measurements NaCl tracer injection
Piot and Tavoularis (2011)	Eccentric annular channel, $e = 1 - 2\delta/(D-d) = 0 - 0.8$. $d/D = 0.6$	320 - 1,420	Water	Dye injection to visualize flow instabilities	Dye Injection

2.3 Numerical Work

2.3.1 Reynolds Averaged Navier Stokes (RANS) Numerical Work

Trupp and Aly [55] simulated triangular arrays which had P/D ratios ranging from 1.12 to 1.35 and Reynolds numbers of 27,000 - 250,000. For turbulence modeling, they used a transport equation for the turbulent kinetic energy (k) and the Launder-Ying model was used for the secondary flows. Their results indicate that secondary flows weaken with an increase in P/D but strengthen with an increase in Reynolds number.

Seale used his experimental work published in 1979 [39] as validation for numerical analysis [18]. A k - ϵ model was used, which coupled with the assumption of isotropic diffusivity, under predicted the gap Stanton numbers by an order of magnitude and could not predict the hydrodynamic details of the flow or the temperature distributions. Despite these errors in validation, Seale still was able to conclude that secondary flow does not play a major role in subchannel mixing.

Rapley and Gosman [19] looked at triangular array geometries, simulating the work of a number of experiments, including the work of Carajilescov and Todreas [17] as well as Trupp and Azad [30]. Rapley and Gosman used the k - ϵ turbulence model, along with the secondary flow model of Launder and Ying, since previous investigations had found these to provide a good general approach. Their predictions were in quite good agreement with the experimental work, as long as the secondary flow model was turned on. Rapley and Gosman showed that the secondary flow has a pronounced effect on the wall shear stress, removing a lot of the variation in the stress, as well as shifting the point where the maximum stress is seen. They stress that the

transport provided by secondary flows near the walls necessitates the use of anisotropic diffusivities in any predictions.

Wu [20] simulated the results of Hooper and Rehme [10], Seale [39] and Wu and Trupp [36]. He used the k - ϵ turbulence model, along with the model of Launder and Ying for the modeling of 'algebraic stresses', which previously were denoted as secondary flows. However, for the anisotropic factor, he developed his own model, based on experimental results. This model was based on the theory that the subchannel mixing was due to periodic eddy motion across the gap. Wu achieved very good agreement between measurements and predictions, which underlines the assumptions made in the formulation of the anisotropy factors.

Lee and Jang [56] used a nonlinear k - ϵ turbulence model which was based on work done in 1987 by Speziale. They modeled the geometry of Carajilescov and Todreas [17], finding reasonably good agreement without tweaking the model for geometrical considerations. Their work showed that although secondary flow in the cross plane provided good explanation for the convective mass transport, the gap region's turbulent stresses could not adequately be simulated using a theoretical model based on secondary flows. A model which considers macro scale eddy motion across the gap is thought to be needed, with the caveat that the underlying physics may require more than a gradient style model.

Rock and Lightstone [57] furthered the numerical analysis of Seale [18], using an isotropic k - ϵ model to examine Seale's experimental work [39]. Their model gave good predictions for both the velocity and friction factor, but under predicted the inter-subchannel mixing. They saw the need for a turbulence model which would accurately predict the anisotropy of the flow in the gap, suggesting an algebraic turbulent stress model would be a

logical step towards this goal. Continuing the work of Rock and Lightstone [57], Suh and Lightstone [58] used both the k - ϵ model and, as previously recommended, an algebraic turbulent stress model. The specific algebraic model chosen was the Reynolds stress model, developed by Launder, Reece and Rodi. Four main areas of agreement were examined - velocity distribution, angular turbulence intensity near the gap, temperature gradients near the gap and the inter-subchannel mixing. As might be expected, the Reynolds stress model better predicted the velocity distribution, due to modeling of secondary flows. However, the Reynolds stress model could not reproduce the angular turbulence intensity, the temperature gradients or the inter-subchannel mixing.

Baglietto and Ninokata [59] compared three turbulence models; the k - ω model, shear stress transport (SST) model and a non-linear adaptation of the k - ϵ model, developed by Shih, Zhu and Lumley (SZL) in 1993. They compared their results to experimental work done in 1976 by Mantlik, Heina and Chervenka. It was found that the SZL model predicted velocity distributions, shear stress distributions and secondary flows quite accurately, leading Baglietto and Ninokata to conclude that the SZL model was a viable model for use in subchannel mixing applications. They also disagree with previous researchers who used a non-linear k - ϵ model, Lee and Jang [54], in that modeling the effect of eddy motion across the gap is not needed.

Tóth and Asózdí [60,61] conducted a two stage investigation; firstly looking at a number of turbulence models, then using the best model to look into the effects of the spacer grid in rod bundle flows. The turbulence models under consideration were the k - ϵ model, the shear stress transport model, and two Reynolds stress models - the baseline model and the one developed by Speziale, Sarkar and Gatski in 1991 (SSG). Using data from Trupp and Azad [30] as their validation study, Tóth and Asózdí chose the baseline Reynolds stress model, because it was able

to predict the turbulence kinetic energies with greater accuracy than any other model. Additionally, the Reynolds stress models were able to reproduce secondary flow, which the other models cannot. Tóth and Asózdi modeled a rod bundle with and without a spacer grid, finding that the spacer grid affects the velocity distribution as well as the outlet temperature. They concluded that future models should take into account the spacer grid in order to be accurate in calculating the flow and heat transfer in rod bundles.

Table 2.2: Summary of numerical work based on steady Reynolds Averaged Navier Stokes (RANS)

Investigators	Experimental Validation	Momentum Model	Turbulence Model	Anisotropy Factor	Additional Secondary Flow Model
Carajilescov and Todreas (1976)	Carajilescov and Todreas (1976)	Vorticity stream conservation equation	k-transport equation model	None	Launder and Ying (1973)
Aly, Trupp and Gerrard (1978)	Aly, Trupp and Gerrard (1978)	Vorticity Stream conservation equation	k-transport equation model	None	Launder and Ying (1973)
Trupp and Aly (1979)	Kjellstrom (1971) Carajilescov and Todreas (1976) Trupp and Azad (1975) Subbotin, Ushakov, Levchenko, Alexandrov (1971)	Vorticity stream conservation equation	k-transport equation model	None	Launder and Ying (1973)
Seale (1979)	Seale (1979)	Vorticity stream conservation equation	k- ϵ transport equation model	Empirical correlations	Launder and Ying (1973)
Seale (1982)	Seale (1982)	Vorticity stream conservation equation	k- ϵ transport equation model	Empirical correlations	Seale (1982)
Rapley and Gosman (1986)	Carajilescov and Todreas (1976) Trupp and Azad (1975) Subbotin, Ushakov, Levchenko, Alexandrov (1971) Fakory and Todreas (1979)	Navier-Stokes Equations	k- ϵ transport equation model	None	Launder and Ying (1973)
Wu (1994)	Hooper and Rehme (1984) Seale (1982) Wu and	Navier-Stokes Equations	k- ϵ transport equation model	Wu (1994)	Launder and Ying (1973)

	Trupp(1993)				
Rock and Lightstone (2001)	Seale (1979)	Navier-Stokes Equations	k- ϵ transport equation model	None	None
Suh and Lightstone (2004)	Seale (1979)	Navier-Stokes Equations	k- ϵ transport equation model, Reynolds stress model (Launder, Reece and Rodi, 1975)	None	None
Baglietto and Ninokata (2005)	Mantlik, Heina, Chervenka (1976)	Navier-Stokes Equations	Shih, Zhu and Lumley (1993) k- ω transport equation model Shear-Stress Transport model	None	None
Tóth and Asózdi (2010)	Trupp and Azad (1975)	Navier-Stokes Equations	k- ϵ transport equation model Shear-Stress Transport model BSL Reynolds Stress Model SSG Reynolds Stress Model	None	None

2.3.2 Unsteady Reynolds Averaged Navier Stokes (URANS) Numerical Work

Chang and Tavoularis simulated the geometry of Guellouz and Tavoularis [14,15] three different times, adding a new physical effect to each successive simulation. Each time, the RNG k - ϵ turbulence model was used as the initial conditions for a transient Reynolds stress turbulence model simulation.. They started with an isothermal simulation of the domain [22], where they showed the existent of coherent structures with the Q-criterion. The gap region had significant contributions from the coherent structures to the kinetic energy measured there, with the contributions being greater in the spanwise and streamwise directions compared to the transverse direction. These structures greatly influence the transient velocity fields within the domain, especially the gap region, and are responsible for the increased mass and momentum transport through the gap. Their second paper [62] introduced heat transfer in two ways - firstly by heating the central rod to a constant temperature and secondly by introducing a constant heat flux in the rod. Chang and Tavoularis found that the coherent structures which greatly increase the transport through the gap serve to moderate the time-averaged temperature field while also creating large local fluctuations in the transient temperature and heat transfer coefficient. Lastly, Chang and Tavoularis looked at varying dimensionless gap size in a heated domain [63]. The dimensionless gap sizes investigated were $\delta/D = 0.10, 0.03$ and 0.01 . They found that temperature fluctuations and turbulent kinetic energy increased when the gap size was decreased from $\delta/D = 0.10$ to 0.03 , but decreased when the gap size dropped to 0.01 . This demonstrates that for a given geometry and Reynolds number, there is a threshold gap size below which the viscous effects will damp out any pulsating nature to the flow. Logically, as one increases the gap size, the strength of the pulsations will also fade, as the velocity gradient decreases. This

theory contradicts the extrapolation of current empirical correlations, but is well supported by experimental evidence in narrow gaps.

As well as doing simulations in a simplified rod geometry, Chang and Tavoularis ran simulations of a 37-rod bundle [64], taking one sixth of the total bundle and applying symmetry boundary conditions. They simulated the experimental work of Ouma and Tavoularis [27] and Baratto et. al. [51], using the Reynolds stress model. Their measurements show that the velocity fluctuations and the coherent structures weren't randomly distributed, but were connected to each other. Using Q-criterion visualization, they also showed the structures within the simulated bundle. From the few images provided by Chang and Tavoularis, it can be seen that the structures wrap around the rods and appear to be interacting with each other. However, the agreement attained by Chang and Tavoularis with experimental results is quite poor in some parts, with a predicted Strouhal number about twice that of the experimentally calculated Strouhal number. They also used quite a high residual of 1×10^{-3} , which could imply that they had some issues with convergence.

Merzari et. al. simulated a subchannel bounded by four rods in a triangular array [65]. The experimental work they used for validation of their model was Krauss and Meyer (1998), almost identical to Kraus and Meyer's earlier work from 1996 [41]. Using the Q-criterion method of structure identification, they found alternating structures in a gap plane, as Chang and Tavoularis also found and commented upon earlier [22]. Merzari et al. concluded that any simulations involving pulsating flow within the subchannel require the use of URANS modeling, since RANS cannot accurately predict the time-dependent nature of the flow. They also conclude that anisotropic modeling is greatly superior to isotropic modeling and thus recommend that future work use anisotropic models. Within their own work, however, they do impose flow

conditions on the gap edges of their domain which enforce an unsupported assumption of flow through the gap region. Any simulation of a multi-rod experiment can run into this issue and so either should simulate the entire bundle or choose a simpler geometry which won't raise the same problem.

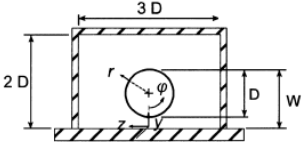
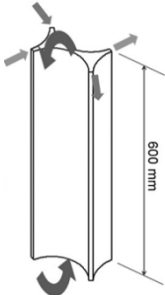
Abbasian et. al. combined numerical and experimental work on a 43 rod bundle [23]. They utilized three approaches - detached eddy simulation (DES), large eddy simulation (LES) and a URANS approach using the Reynolds stress model. They found that the LES approach most accurately predicted the experimental results, and recommended using this as the sole approach to numerical subchannel analysis. The LES approach utilized the Dynamic Smagorinsky Model (DSM), which was able to capture eddy movement within subchannels. It also captured the different fluid forces acting upon the rod bundle, the combination of which was found to be able to produce transverse motion of the bundle. They concluded that geometrical asymmetry will give rise to strong vortices and that accurate modeling of up and downstream flow is required fully to understand the complexities of the subchannel mixing phenomenon.

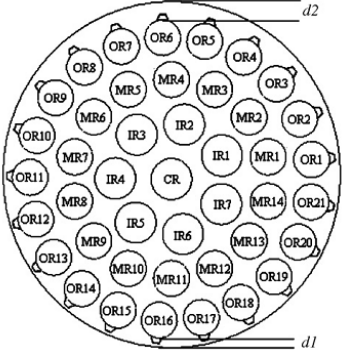

Home et. al. [24] simulated the work of Meyer and Rehme [46] using the Spalart-Allmaras model. This model is isotropic, and mainly has been used in aerospace applications. The authors see a similarity between the vortex street phenomenon of subchannel mixing and the vortex shedding phenomenon well known in aerospace applications. Since the Spalart-Allmaras is a one equation model, it is much more cost effective in terms of computational time than two equation models or the Reynolds stress model. Home et al. compared the Spalart-Allmaras model to the standard $k-\epsilon$ model. The main difference between the $k-\epsilon$ model and the Spalart-Allmaras model was found in the prediction of frequency. For a given Reynolds number, the $k-\epsilon$ model found different frequencies depending on the position of the monitor point. As such,

Home et al. conclude that the Spalart-Allmaras model is an excellent choice for simulations of subchannel mixing. Despite the isotropic nature of the model, it is concluded that the anisotropic effects of secondary flows are not important to mixing, as the secondary flows have been shown experimentally to be of a low magnitude in comparison to the mean axial flow [30,33].

Table 2.3: Summary table of Unsteady Reynolds Averaged Navier Stokes investigations

Investigators	Experimental Validation	Grid/Time Step/ Residual Information	Turbulence Model	Geometry
Chang and Tavoularis (2005)	Guellouz and Tavoularis (2000)	10.2x10 ⁶ nodes 1.3x10 ⁶ nodes 0.3x10 ⁶ nodes $t = 1.9 \times 10^{-3} L/U_b$ $t = 3.81 \times 10^{-4} s$	RNG k- ϵ transport equation model used to generate initial conditions, then Reynolds Stress Model	
Chang and Tavoularis (2006)	Guellouz and Tavoularis (2000)	1.3x10 ⁶ nodes $t = 1.9 \times 10^{-3} L/U_b$ $t = 3.81 \times 10^{-4} s$ Residuals: 10 ⁻⁴ Temp Residuals: 10 ⁻⁶	RNG k- ϵ transport equation model used to generate initial conditions, then Reynolds Stress Model	
Chang and Tavoularis (2007)	Ouma and Tavoularis (1991) Baratto, Bailey, Tavoularis (2006)	0.2x10 ⁶ nodes 0.8 x10 ⁶ nodes 2.2x10 ⁶ nodes $t = 3.9 \times 10^{-4} L/U_b$ $t = 1.01 \times 10^{-4} s$ Residuals: 10 ⁻³	Reynolds Stress Model	

<p>Chang and Tavoularis (2008)</p>	<p>Guellouz and Tavoularis (2000)</p>	<p>$\delta/D = 0.1:$ 1.2×10^6 nodes</p> <p>$\delta/D = 0.03:$ 1.4×10^6 nodes</p> <p>$\delta/D = 0.01:$ 1.5×10^6 nodes</p> <p>$t = 1.9 \times 10^{-3} L/U_b$</p> <p>$t = 3.81 \times 10^{-4} s$</p>	<p>RNG k-ϵ transport equation model used to generate initial conditions, then Reynolds Stress Model</p>	
<p>Merazi, Ninokata, Baglietto (2008)</p>	<p>Krauss and Meyer (1998)</p>	<p>600 000 nodes $t = 10^{-5} s$, chosen to satisfy $\Delta t \ll \frac{1}{f}$</p>	<p>Anisotropic k-ϵ transport equation model</p>	

<p>Abbasian, Yu and Cao (2009)</p>	<p>Abbasian, Yu and Cao (2009)</p>	<p>6.5×10^6 nodes $T = 5 \times 10^{-5}$ s</p>	<p>Reynolds Stress Model Detached eddy simulation Large eddy simulation with Dynamic Smagorinsky Model</p>	
<p>Home, Arvanitis, Lightstone, Hamed (2009)</p>	<p>Meyer and Rehme (1994)</p>	<p>0.634×10^6 nodes 1.27×10^6 nodes 1.28×10^6 nodes 0.278×10^6 nodes $t = 10^{-4}$ s</p>	<p>Spalart-Allmaras Model</p>	

2.4 Summary

The previous research discussed above has focused on examining the enhanced mixing found in subchannel geometries. It has been found that the mixing increases with a decrease in the gap spacing, represented by the pitch to diameter ratio, P/D . This mixing was originally thought to be caused by secondary flows, but these have since been shown to be small [9,33,34,36,41] and do not have a significant impact on the phenomenon. The enhanced mixing cannot be explained by turbulence alone [39]. It has been observed that periodic flow pulsations are the cause of this mixing [10,12,43-46]. The vast majority of experimental work has utilized a simplified geometry, with experimental domains becoming as simple as a rod in a rectangular [14,15,53] or circular duct [16].

Experiments have shown that subchannel flow pulsations can occur under laminar flow conditions. This provides a logical starting point for studying the underlying causes of the pulsations since it removes the complication of turbulence modelling. As can be seen from the numerical investigations, there are numerous turbulence models available and no consensus has been reached within the research community as to which approach is unilaterally the best to use. There are not a great deal of laminar experimental papers on offer for use in validation of numerical results, but of the few which have been published [16,50,53,54], the work of Gosset and Tavoularis [53] in 2006 has the most laminar flow data and represents the best results for good comparison with numerical analysis. To the author's knowledge, previous numerical studies of laminar flow pulsations have not been reported.

Chapter 3

Methodology

3.1 Introduction

This chapter presents the details of the simulations which have been performed. The experiment used for validation is discussed in section 3.2 and the simulation details are given in section 3.3. Analysis of the numerical results and comparison with the experimental data of Gosset and Tavoularis [53] will be given in chapter 4.

3.2 Details of Experiment

As discussed previously in section 2.2, Gosset and Tavoularis [53] performed experiments in a greatly simplified subchannel geometry. The geometry consisted of a horizontal rectangular channel containing a rod. Asymmetry was deliberately created within the domain by varying the distance between the rod and the top wall. The total length of their experimental domain was approximately 1168 mm, which gave a L/D_H equal to approximately 56. Their geometry is shown below in figure 3.1.

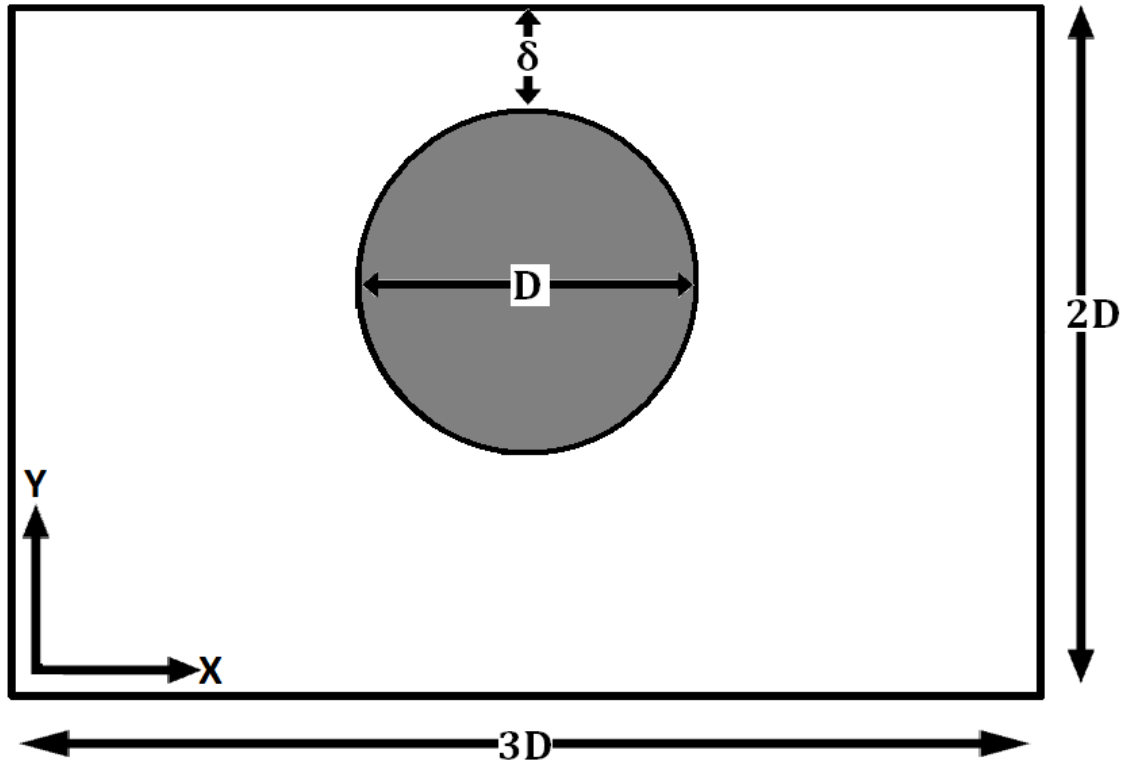


Figure 3.7: Cross-section of the experimental domain of Gosset and Tavoularis [53]. Flow is into the page. The central rod, with diameter D , is the basis of the width and height of their domain. The gap size, δ , was varied in their experimental work.

The experiments, which used water at approximately 25 C as the working fluid, considered a number of different gap sizes and Reynolds numbers. Some of the Reynolds numbers included were within the fully laminar flow regime. For non-dimensionalized (δ/D) gap sizes 0.3, 0.2, 0.1, 0.05 and 0.025, they produced a diagram of Strouhal number vs. Reynolds number. They also showed dye streak images for some of the Reynolds numbers used for each gap size. These dye streak images, where the dye is released at the midpoint of the gap, range from showing clear pulsations to showing a smearing of the dye which makes it difficult to see

any pulsatile nature to the flow. The gap size for which the clearest dye streak images are shown is $\delta/D = 0.3$. As such, three Reynolds numbers at this gap size were chosen for the numerical simulations, since these conditions resulted in the best data for validation. These Reynolds numbers (718, 900, 955) were taken from the diagram of Strouhal number vs. Reynolds number produced by Gosset and Tavoularis [53], reproduced below in figure 3.2.

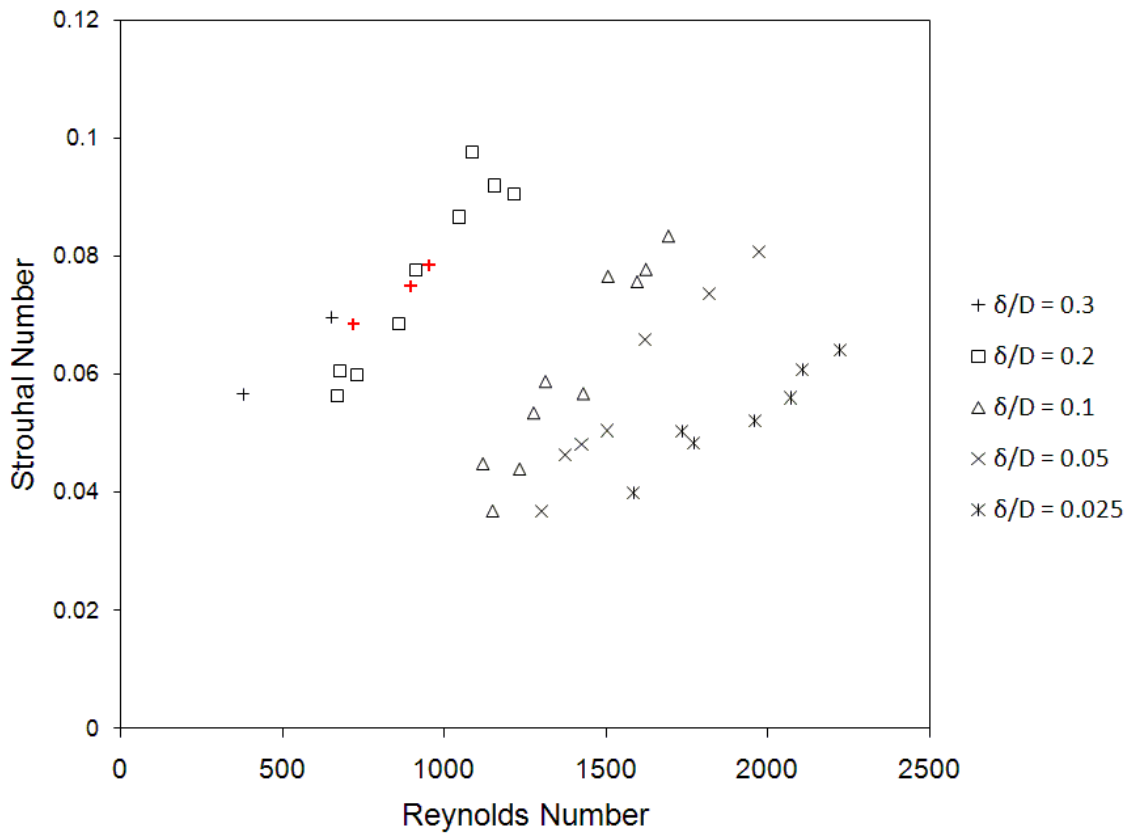


Figure 3.8: Reynolds number vs Strouhal number. Adapted from Gosset and Tavoularis [53]. The red symbols represent the Reynolds numbers at which simulations were run.

Gosset and Tavoularis used these dye streaks as a means to estimate the frequency of the pulsations by counting the number of directional changes the dye made in the spanwise direction during a given period of observation. This gave an average frequency, for which they report a

standard deviation of 20%. They similarly used the dye streaks to obtain an average value for the wavelength of the pulsations, which had a reported standard deviation of 10% [53].

3.3 Simulation Details

3.3.1 Spatial and Temporal Grid setup

The mesh used for all simulations was a structured mesh, designed to give reasonable refinement in the gap area without being unnecessarily fine in the far gap region. The cross section of the mesh contained 2772 nodes, and is shown below in Figure 3.3.

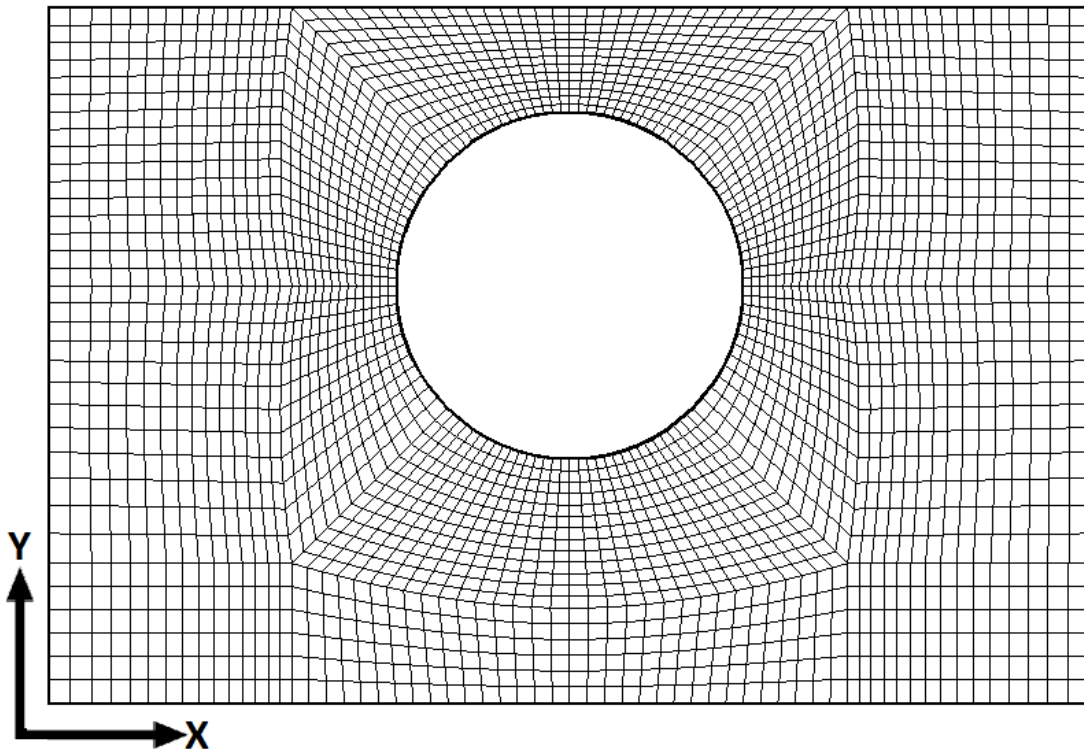


Figure 3.9: Cross-section of mesh used in all simulations. The thicker lines indicate boundaries within the domain, the details of the boundary conditions will be given in section 3.3.4. The mesh is structured, with refinement in the gap region to ensure enough resolution to capture the flow. Axial flow is normal to the page.

It can be observed from figure 3.3 that aspect ratios of individual elements were kept reasonably small, even in the most extreme case. This was done so as to mitigate against any numerical errors that might otherwise occur. In the axial direction, elements were equally spaced every 0.8 mm, which for a total numerical domain length of 1168 mm, this gives a mesh size of 4,047,120. In order to capture the temporal details of the flow, the time step used was calculated by inverting the expected frequency from Gosset and Tavoularis and dividing by 100. This means the time step was 0.05 s for the case where $Re = 718$, 0.04 s for $Re = 900$ and 0.03 s for $Re = 955$. It was felt that this would give adequate resolution of the pulsations without being unnecessarily fine.

3.3.1.1 Independence Tests

Independence tests for the spatial and temporal grid were performed by doubling the number of elements in each direction (x,y,z,t). Both of these tests were done using a much smaller length domain, to reduce unnecessary computational effort. The baseline grid was 200 mm in length, having 693,000 spatial elements, with a timestep of 0.05 seconds. The spatial independence test grid had 5,544,000 elements, and the temporal independence test used a timestep of 0.025 seconds. Each simulation ran for 110 seconds

The evaluated properties for each test came from a series of points which monitored the velocities and pressure at discrete locations throughout the domain. For the independence tests, the local RMS long-time value of the spanwise velocity (u) was evaluated for eleven of these discrete points. The points used were located at the midpoint of the gap and were evenly distributed throughout the rod diameter. A summary of the RMS values of spanwise velocity and percentage differences is found in Table 3.1. To aid in discussion of the data, the points are

numbered 1-11, with point 6 being the centre of the gap. A diagram showing the location of these points is seen below in figure 3.4

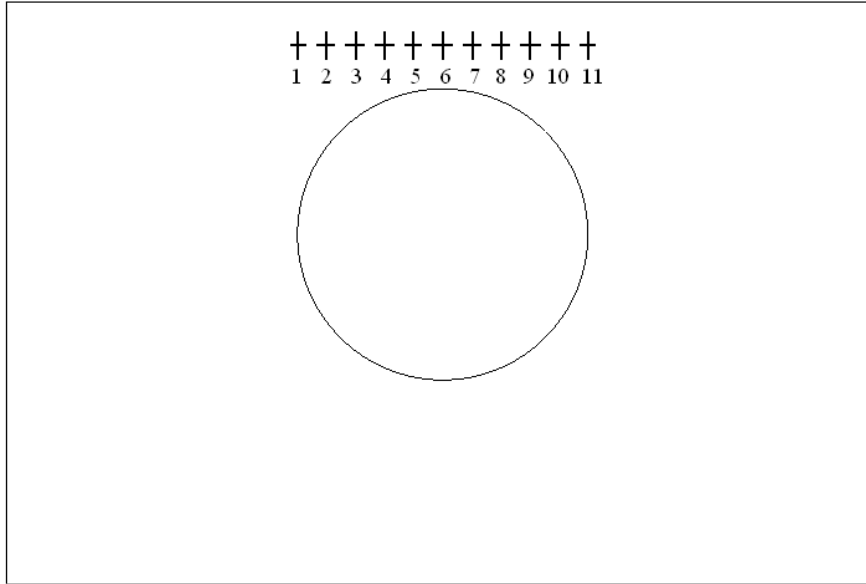


Figure 3.10: Diagram of the discrete points used in the independence tests.

Table 3.4: Details of the independence tests conducted.

Point	1	2	3	4	5	6	7	8	9	10	11
RMS Values of u-velocity for spatial independence test (mm/s)											
Fine	3.19	3.89	4.66	5.30	5.76	5.89	5.60	5.44	4.64	3.94	3.24
Coarse	3.13	3.79	4.67	5.29	5.72	5.79	5.70	5.26	4.64	3.93	3.12
% Diff	1.79	2.58	0.24	0.31	0.66	1.84	1.88	3.39	0.01	0.25	3.98
RMS Values of u-velocity for temporal independence test (mm/s)											
Fine	3.17	3.81	4.64	5.26	5.70	5.77	5.69	5.23	4.59	3.87	3.07
Coarse	3.13	3.79	4.67	5.29	5.72	5.79	5.70	5.26	4.64	3.93	3.12
% Diff	1.06	0.40	0.64	0.56	0.44	0.25	0.27	0.55	1.04	1.55	1.51

As can be seen from table 3.1, the independence tests show a sufficient resolution in the coarser spatial and temporal grids. The fine grid shows a greater percent difference than the fine time grid. The average differences for the percent differences are 1.54% and 0.75% , for the fine grid and fine timestep respectively. These values are also used to give a rough estimation of the error present in the calculation of dominant frequency, which will be used to compare the numerical results to the experimental results. Sample graphs of the spanwise velocity time trace are shown in figures 3.4 to 3.6.

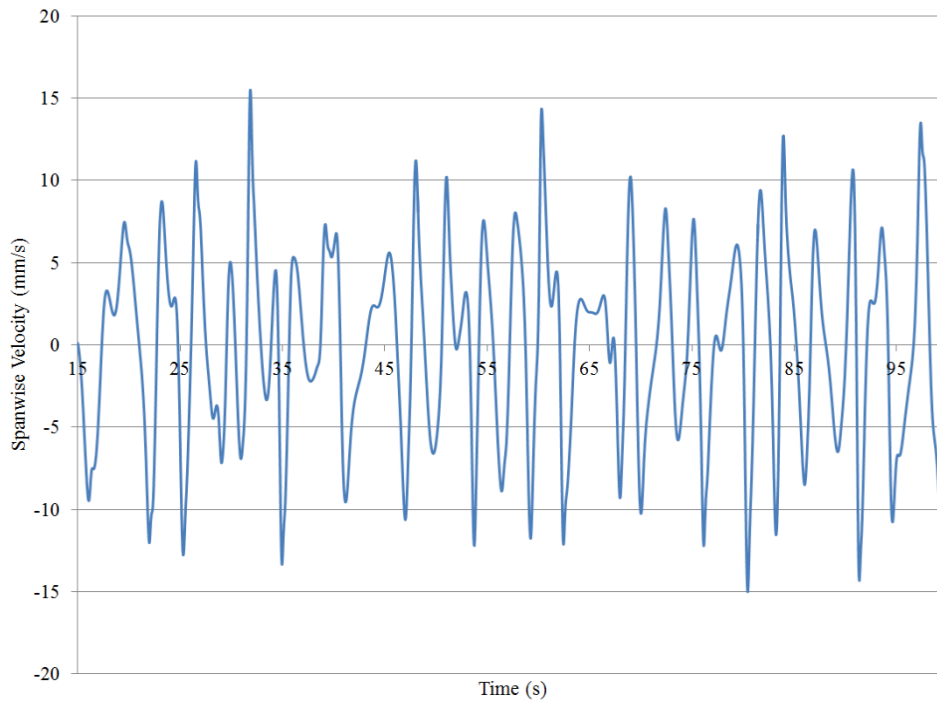


Figure 3.5: Time trace of spanwise velocity for the coarse grid. The point from which the data is point 6 from table 3.1. Time starts 15 seconds into the true transient.

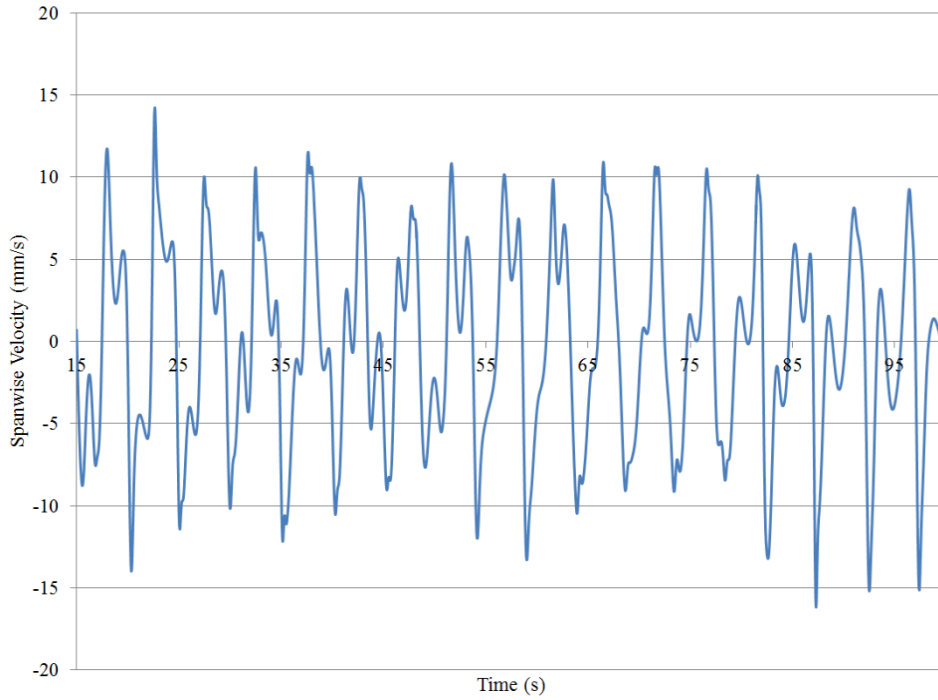


Figure 3.6: Time trace of spanwise velocity for the fine grid. The point from which the data is point 6 from table 3.1. Time starts 15 seconds into the true transient.

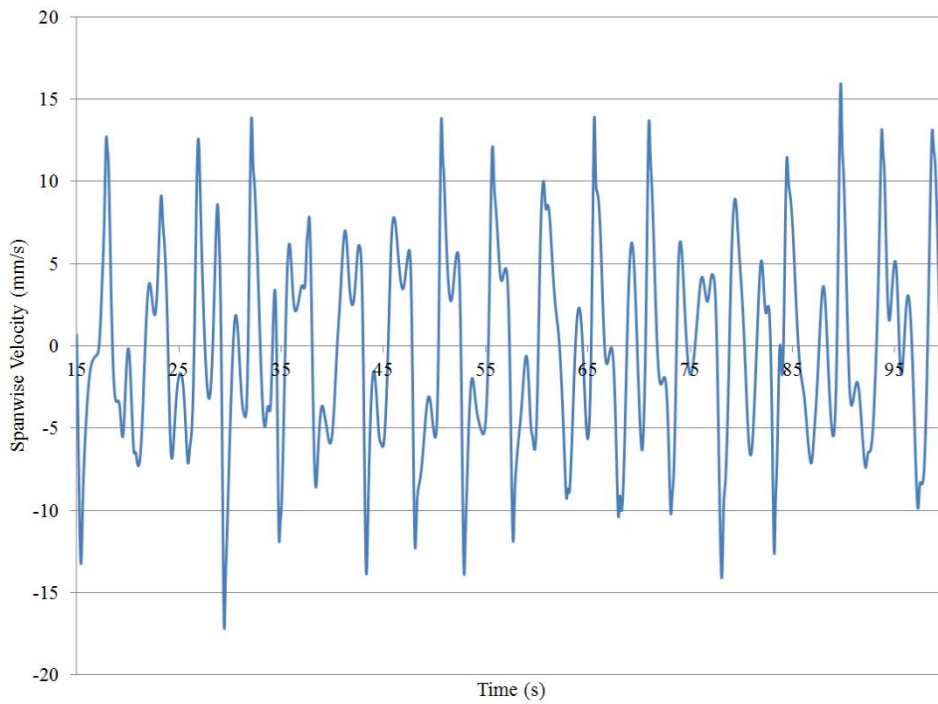


Figure 3.7: Time trace of spanwise velocity for the fine timestep. The point from which the data is point 6 from table 3.1. Time starts 15 seconds into the true transient.

The graphs shown in figures 3.5 to 3.7 are samples from the independence tests conducted. The coarse grid, shown in figure 3.5, does not reproduce the refined details seen in the fine grid or fine timestep. One of the prominent features of the refined solutions, seen in figures 3.6 and 3.7, is what appears to be a somewhat out of phase signal with a similar frequency which reduces the height of velocity peaks. The full details of this signal would not be predicted as accurately with the lower resolution in space and time.

However, the extrema of velocity magnitudes are quite similar between the traces. Although having visually nearly identical signals would be desirable, it is less likely to occur with a flow that is highly transient in nature. The RMS values of velocity within the signals are extremely close, which demonstrates that the signals are statistically similar.

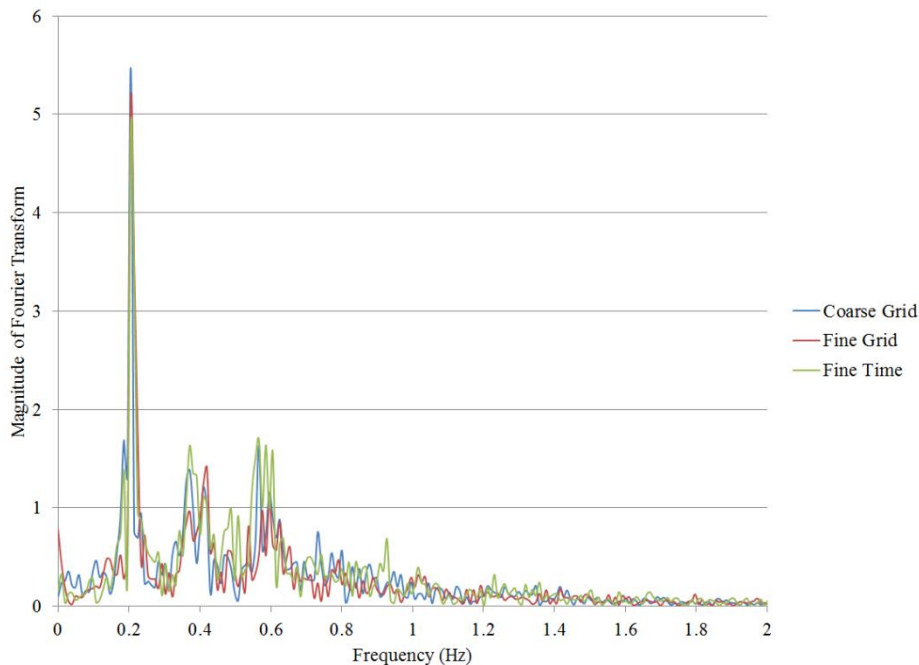


Figure 3.8: Frequency spectra for each independence study conducted. The spectra correspond to the appropriate time trace in figures 3.5, 3.6 and 3.7.

Figure 3.8 above compares the frequency spectra for the independence studies conducted. The time traces shown in figures 3.4, 3.5 and 3.6 were Fourier transformed, and display the same dominant frequency of 0.21 Hz. The coarse grid has the highest magnitude at 0.21 Hz, followed by the fine grid and then the fine timestep.

3.3.2 Fluid Properties

The fluid used in all simulations was water at 25degrees Celsius. The thermophysical properties used in the simulations can be found in Table 3.2 below.

Table 3.5: Fluid properties used in simulations

Property	Value	Units
Fluid	Water	
Temperature (T)	25	C
Density (ρ)	997	kg/m ³
Dynamic Viscosity (μ)	8.90 x10 ⁻⁴	Pa.s

3.3.3 Boundary and initial conditions

All simulations were performed with the same boundary conditions. Walls were considered to be no-slip walls with a velocity of zero. The inlet and outlet were given periodic boundary conditions. The simulation was given a mass flow rate, \dot{m} , which was maintained throughout the domain. This allows there to be spanwise and transverse velocities, without imposing a streamwise velocity which might be different from the bulk velocity. The mass flow rate was calculated from the Reynolds numbers for each simulation, which are based on the bulk velocity

and hydraulic diameter of the channel. This is consistent with the data presented in Gosset and Tavoularis [53].

The initial conditions for the fully transient simulations were obtained from a steady state run, which ran for 3,000 iterations. The same results could be obtained by running the transient case from an initial guess of zero velocity, but this would have added approximately a week to the simulation time without adding much, if any accuracy. The simulations were all run for at least 300 seconds. This was to allow the flow to flush out the effects of the initial conditions. Since ANSYS CFX 12.0 is an implicit code, it is not necessary to have the Courant number be below unity for stability to be achieved.

3.3.4 Advection Scheme

The advection scheme used was the high-resolution scheme. This scheme calculates the transported values between nodes using a spatial gradient and a blending factor. This blending factor, β , is designed to be as close to unity as possible without introducing local oscillations that arise from errors in the solution. The central differencing scheme is similar to the high resolution scheme, with the exception that β is set equal to 1. The blending factor, β , is calculated by evaluating the fluxes at all integrating points adjacent to the node and selecting the minimum value. This scheme is second-order accurate, which is essential for flows with low velocity or turbulence [65]. It has been shown by previous numerical researchers [6,24] that the high resolution scheme works well for predicting flows in subchannel geometries, as it will be more accurate in predicting steep spatial gradients.

3.3.5 Modeling of the Transient term

The transient term was modeled using the second-order backwards Euler method. The change in time of the volume integral of any transported quantity is estimated by taking a weighted average of the transported value over the previous two values in time. Like the advection scheme, the second-order backwards Euler method is implicit and it also carries no limitation on the time step.

3.3.6 Equipment and Resources

The simulations were run on a remote accessed HP Z800 workstation, part of the SHARCNET (Shared Hierarchical Academic Resource Computing Network) at McMaster University. This machine has two Intel Xeon 5560 quad-core chips, running at 2.8 Ghz. There are 12 sticks of 4GB DDR3/1333 Mhz RAM on the machine.

Typically, the simulations were run using four processors only, using about 1.5 GB of RAM per processor. The initial conditions took approximately a day and a half to solve, while the full transient runs to 300 seconds took approximately ten days to complete.

Chapter 4

Results and Discussion

4.1 Overview

This section presents analysis of the results from the numerical simulations performed which were based on the experimental results of Gosset and Tavoularis [53]. The simulations used a dimensionless gap size (δ/D) of 0.3, with Reynolds numbers of 718, 900 and 955. The first part of this section deals with comparing the numerical results with the experimental measurements as well as discussion of the results. After the results have been validated against the experiments, a sensitivity of the predictions to the computational domain length is presented. The majority of the results are used to look at various quantities within the pulsing flow to see how pressure, velocities (spanwise and axial) and axial velocity gradient are interconnected with the pulsations. These same quantities will be used to analyze the evolution of flow from a non-pulsing state until the velocities are such that it is apparent they will continue to grow until they are fully evolved.

4.2 Contour Plots of Velocity and Pressure Fluctuations

Flow pulsations are often visualized using contour plots on a horizontal plane that passes through the middle of the gap, as shown below in figure 4.1. Figures 4.2, 4.3 and 4.4 show contour plots of total velocity, spanwise velocity and pressure fluctuations. The pressure fluctuations are defined as the difference between the local instantaneous pressure and the local time average, which here can be determined from the local axial position and the imposed mean pressure gradient so that:

$$p_{Fluctuating} = p - z \left(\frac{dp}{dz} \right)$$

This is simply the pressure with the mean pressure gradient removed.

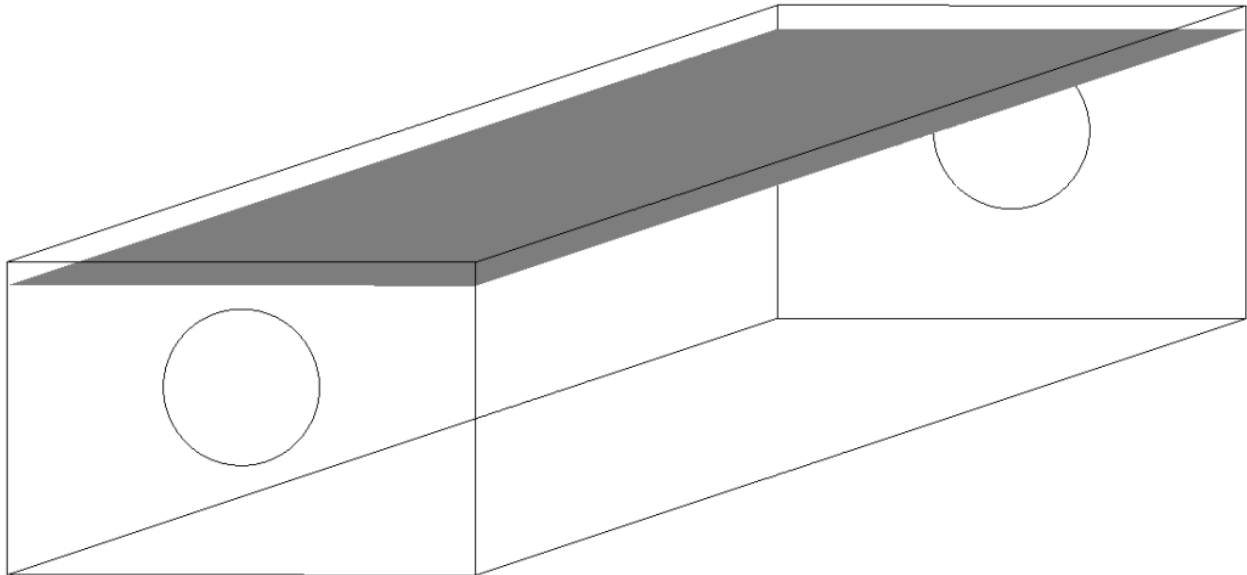


Figure 4.1: Visualization plane used for contour plots viewed from the top down. The axial flow is diagonally from front left to back right. The plane is located at a distance of $0.15D$ from the top wall, midway through the narrowest part of the gap.

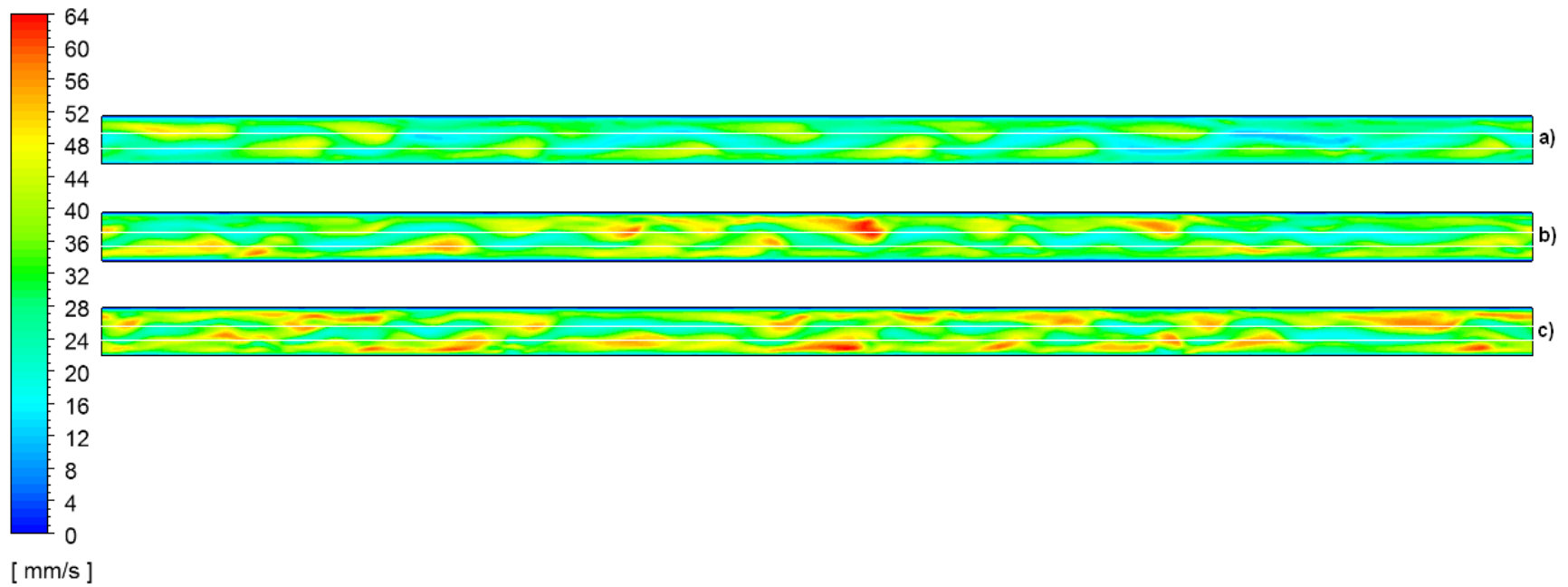


Figure 4.211: Contour plots of total velocity for the three different cases. The plots are taken from the visualization plane seen in figure 4.1. White lines indicate rod position. Flow is from left to right in all cases. Plots taken about 70 seconds after initial conditions have convected out. a) $Re = 718$, b) $Re = 900$, c) $Re = 955$.

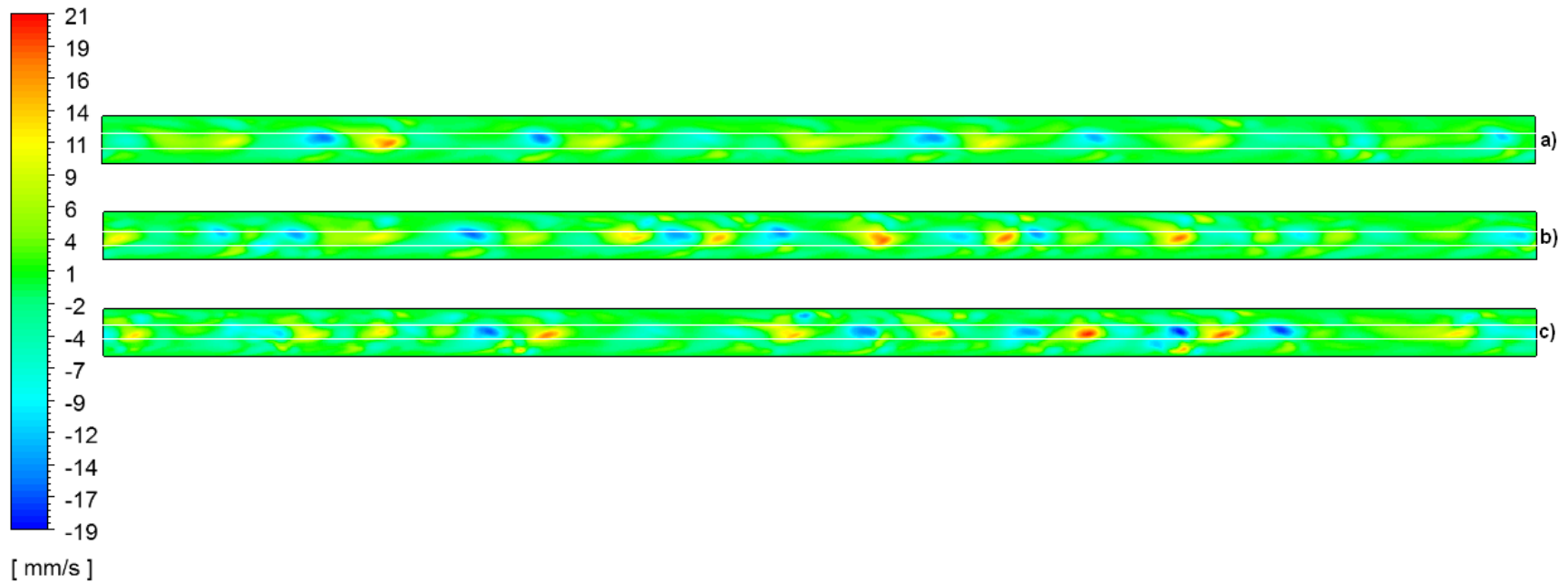


Figure 4.3: Contour plots of spanwise velocity for the three different cases. The plots are taken from the visualization plane seen in figure 4.1. White lines indicate rod position. Flow is from left to right in all cases. Positive velocities are upwards. Plots taken about 70seconds after initial conditions have convected out. a) $Re = 718$, b) $Re = 900$, c) $Re = 955$.

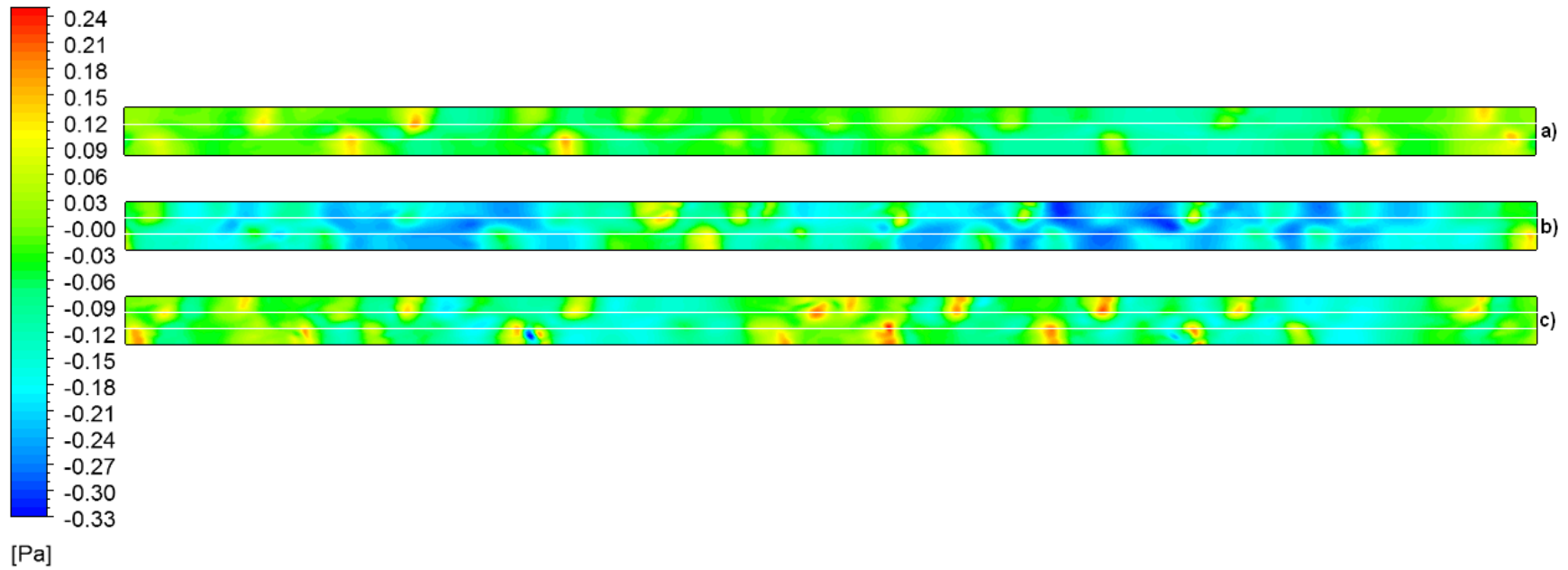


Figure 4.4: Contour plots of pressure fluctuations for the three different cases. The plots are taken from the visualization plane seen in figure 4.1. White lines indicate rod position. Flow is from left to right in all cases. Plots taken about 70seconds after initial conditions have convected out. a) $Re = 718$, b) $Re = 900$, c) $Re = 955$.

All three Reynolds numbers show the same trend of having the lowest total velocities (which aren't forced to be low because of the no slip condition) in the gap region. The flow has a clear quasi-periodic pulsatile nature to it. Figures 4.2 and 4.3 are qualitatively similar to what was observed in the work of Arvanitis [6] and Home et. al. [24], which simulated turbulent gap flows. The relative magnitude of the spanwise velocity is about a third of the total velocity, compared to about an eighth of the total velocity, seen in [6,24]. As the Reynolds number increases, so do the extreme magnitudes of the total and spanwise velocities as well as the change in pressure fluctuations. Table 4.1 below lists the total velocity magnitudes (figure 4.2), the ranges of spanwise velocities (figure 4.3) and the pressure fluctuations differences (figure 4.4) for each Reynolds number.

Table 4.6: Range of the measured quantities seen in figures 4.2, 4.3 and 4.4 respectively.

Re	718	900	955
Total Velocity	52 mm/s	64 mm/s	64 mm/s
Spanwise Velocity	-16 to 18 mm/s	-16 to 18 mm/s	-19 to 21 mm/s
Pressure fluctuations	0.32 Pa	0.50 Pa	0.60 P

The highest total velocities are seen at the edges of the gap, where there is the greatest rate of change in cross-sectional axial flow area. The locations of extreme values of spanwise velocity are such that the flow is moving into the gap region - positive velocities (up) are located on the bottom part of the gap in figure 4.3 and vice versa for negative velocities. These spanwise flows are toward the regions of high total velocity on either edge of the gap.

The high pressure regions extend from the walls, across the channel towards the adjacent gap edges. The total velocity decreases at these high pressure locations, with the locations of high spanwise flow magnitudes also being stopped by the regions of high pressure. The dominant part of the total velocity is the axial velocity, so when the high pressure decreases it, to

conserve mass, there must be a consequent change in spanwise or transverse velocity. The areas of high total velocity are on the edges of the gaps, so with the pressure increase spreading out from the walls, the spanwise velocity will more easily flow through the gap. This serves to slow down the spanwise velocity through the gap, eventually changing the direction of pulsation.

4.3 Spanwise Velocity Time Traces

Transient predictions of velocities at discrete points within the gap region were obtained for analysis of the pulsations. Time traces are shown below for points located at the edges of the gap and the centre of the gap. Each time trace is shown after the initial conditions have been convected out of the domain. The time duration shown in figures 4.5 to 4.13 is a small portion of the total simulation time, which ran for approximately 300 seconds from the start of transient simulations. To traverse the domain, a particle which travelled at the average velocity would take about 33 seconds, 27 seconds and 25 seconds for $Re = 718, 900$ and 955 respectively.

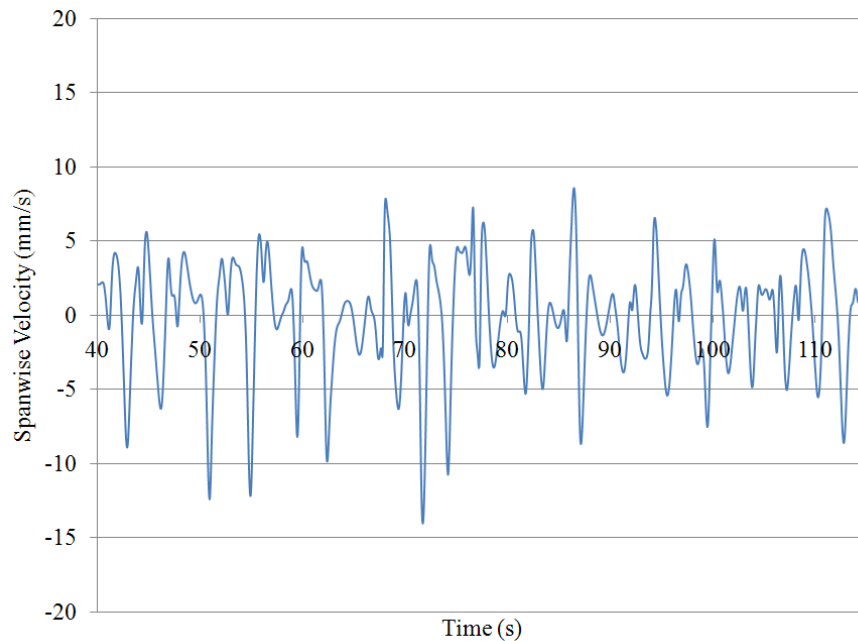


Figure 4.12: Spanwise Velocity time trace for $Re = 718$. Taken from a point at the far left of the gap, point 1 in figure 3.4. Data starts at 40 seconds into true transient.

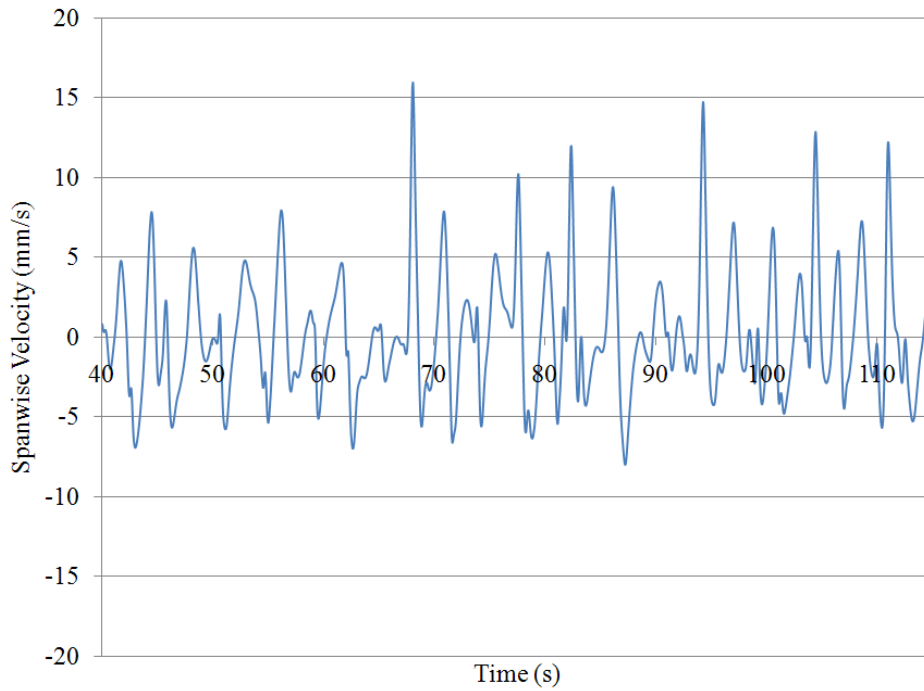


Figure 4.13: Spanwise Velocity time trace for $Re = 718$. Taken from a point at the far right of the gap, point 11 in figure 3.4. Data starts at 40 seconds into true transient.

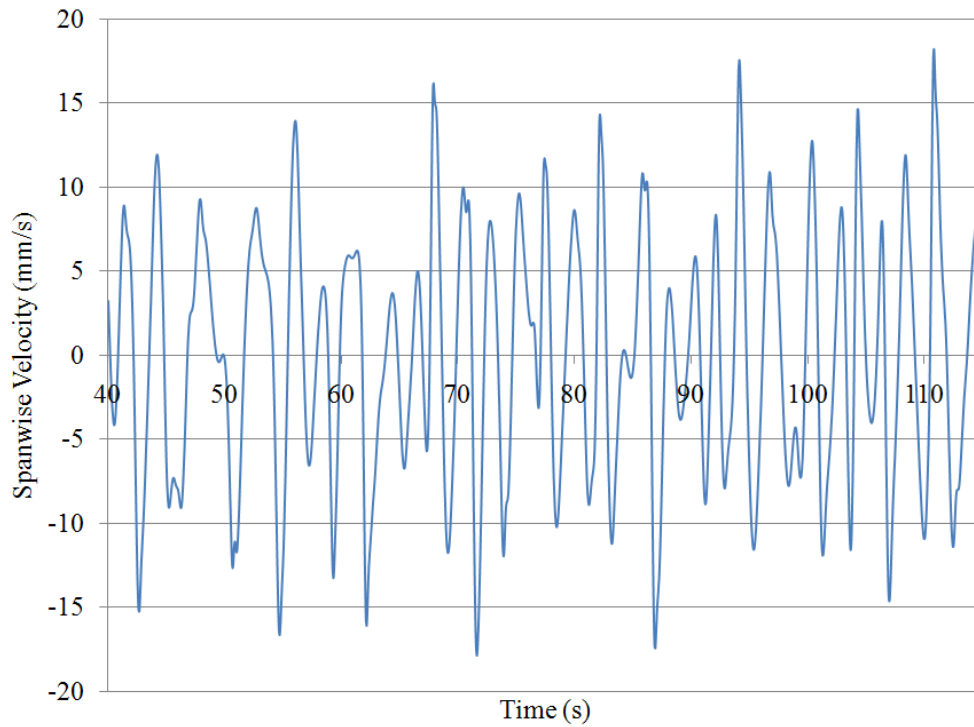


Figure 4.7: Spanwise Velocity time trace for $Re = 718$. Taken from a point at the centre of the gap. Data starts at 40 seconds into true transient.

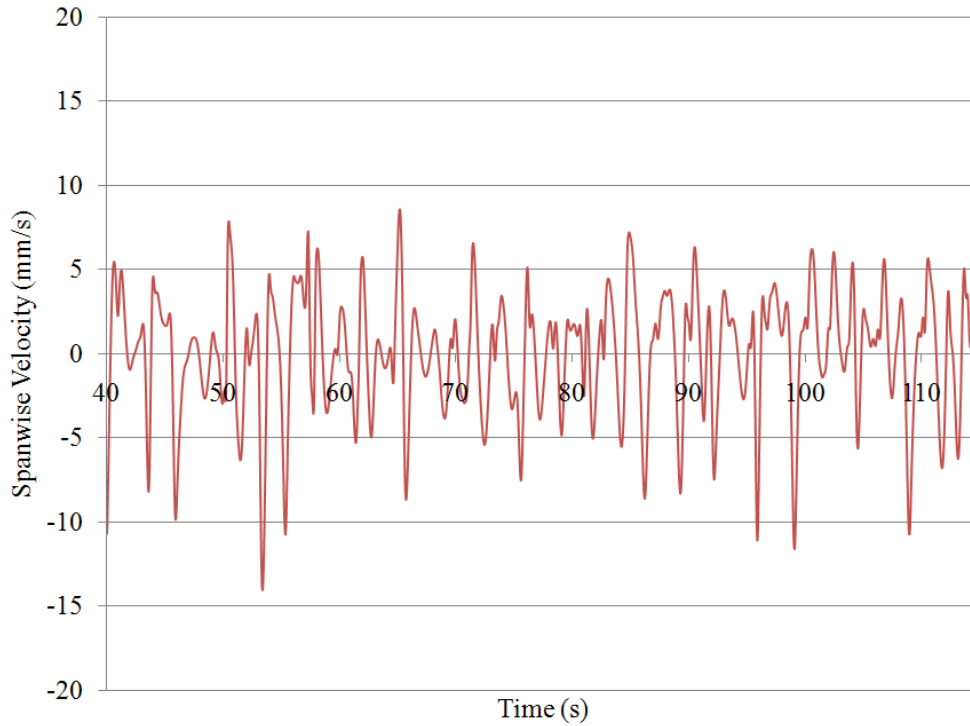


Figure 4.8: Spanwise Velocity time trace for $Re = 900$. Taken from a point at the far left of the gap, point 1 in figure 3.4. Data starts at 40 seconds into true transient.

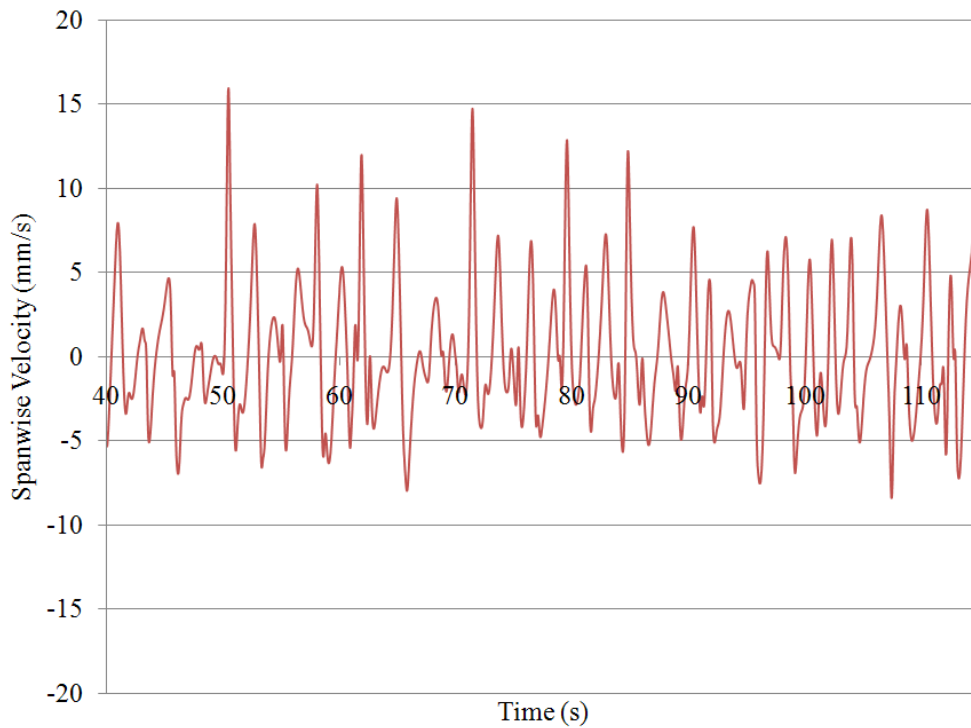


Figure 4.9: Spanwise Velocity time trace for $Re = 900$. Taken from a point at the far right of the gap, point 11 in figure 3.4. Data starts at 40 seconds into true transient.

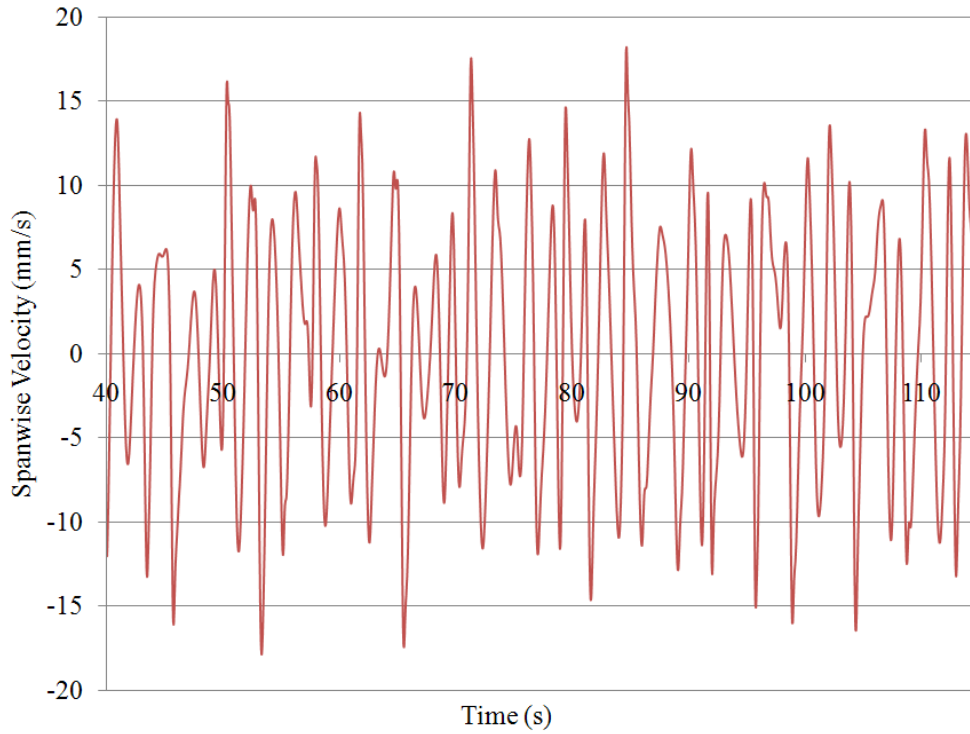


Figure 4.10: Spanwise Velocity time trace for $Re = 900$. Taken from a point at the centre of the gap. Data starts at 40 seconds into true transient.

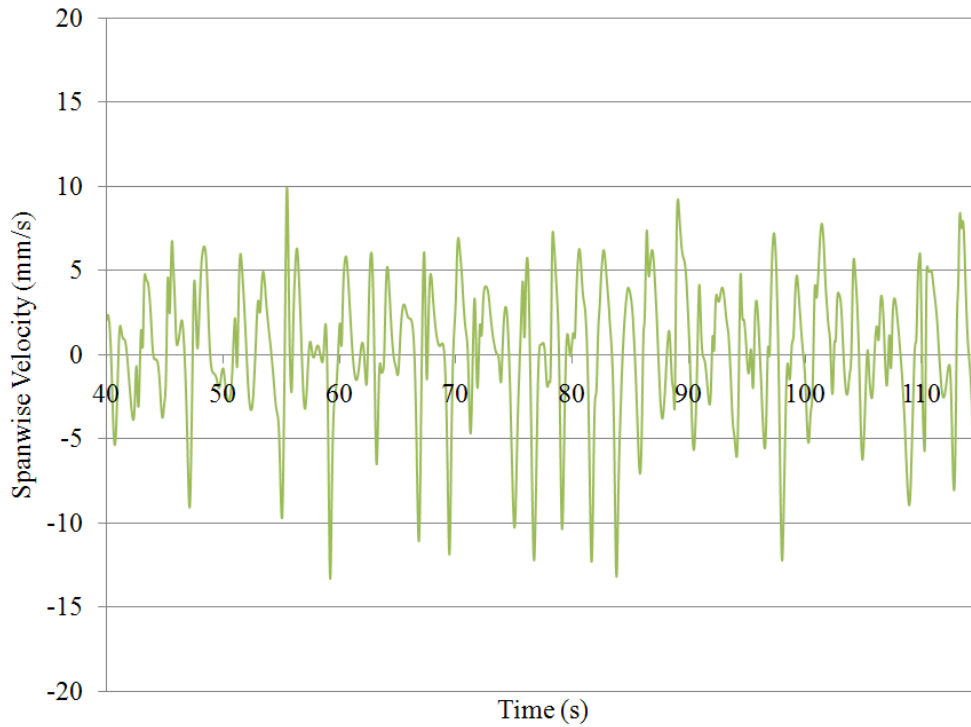


Figure 4.11: Spanwise Velocity time trace for $Re = 955$. Taken from a point at the far left of the gap, point 1 in figure 3.4. Data starts at 40 seconds into true transient.

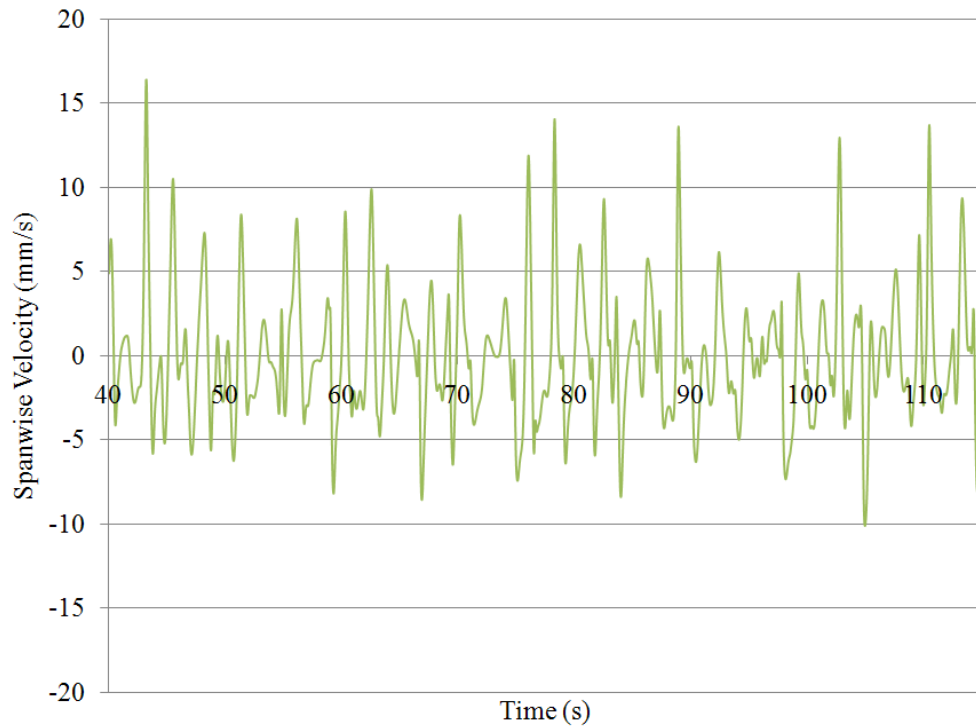


Figure 4.12: Spanwise Velocity time trace for $Re = 955$. Taken from a point at the far right of the gap, point 11 in figure 3.4. Data starts at 40 seconds into true transient.

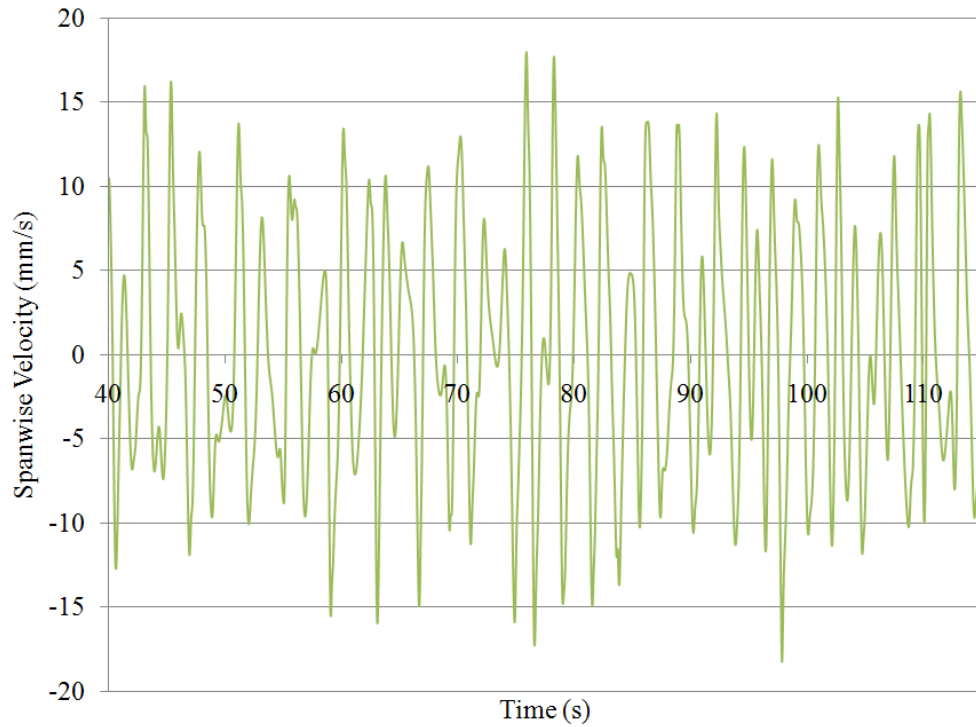


Figure 4.13: Spanwise Velocity time trace for $Re = 955$. Taken from a point at the centre of the gap. Data starts at 40 seconds into true transient.

The flow shown in these time traces is a quasi-periodic flow comprised of a range of frequencies. The time traces from the far left of the gap show a skew towards negative velocities, which would be traveling out of the gap. The corresponding pattern is seen in the time traces on the far right of the gap - a skew towards positive velocities, which again are travelling out of the gap. The time traces from the centre of the gap do not appear to have any significant skew to them. These are the same trends observed in the work of Arvanitis [6] and Home et. al [24]. As Reynolds number increases, the dominant frequency appears also to increase.

Figures 4.14 through 4.16 show distributions of spanwise velocities at three different locations within the gap - far left, centre and far right. These locations are the same as seen in figures 4.5 to 4.13.

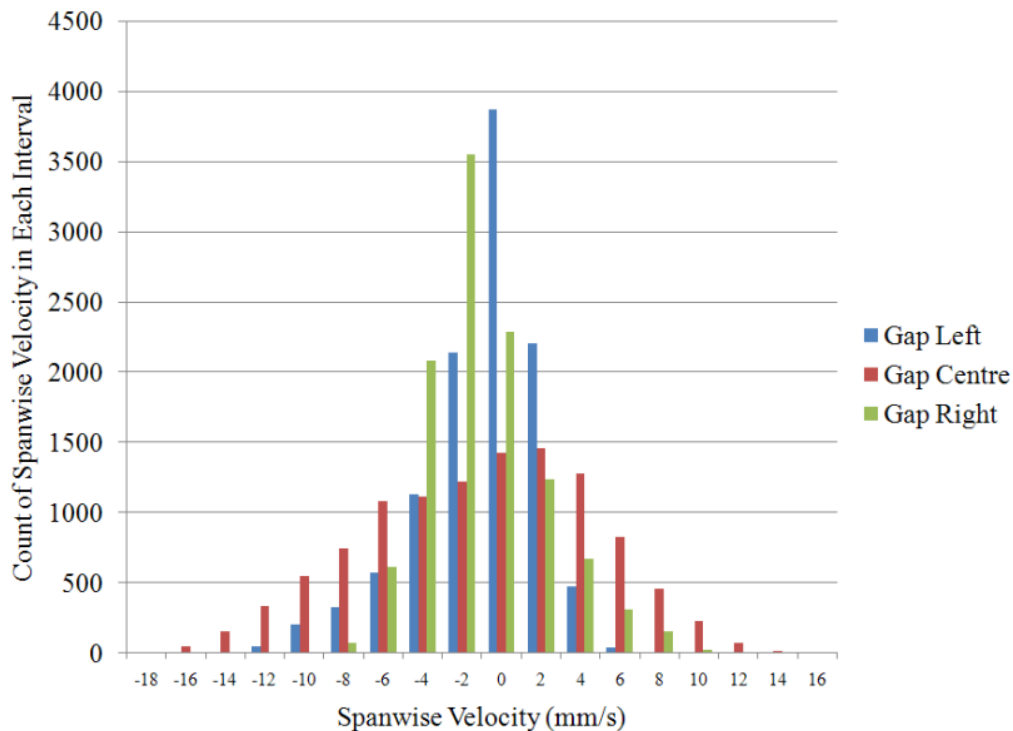


Figure 4.14: Distribution of Spanwise Velocity for $Re = 718$. Approximately 11,000 data points were used for the distribution.

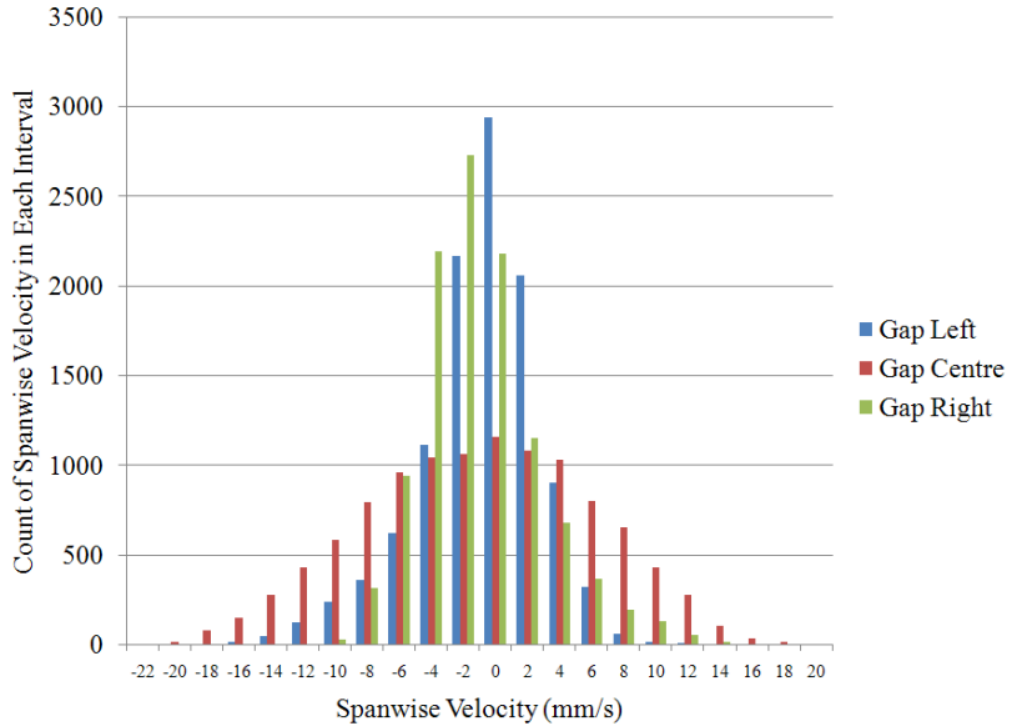


Figure 4.15: Distribution of Spanwise Velocity for $Re = 900$. Approximately 11,000 data points were used for the distribution.

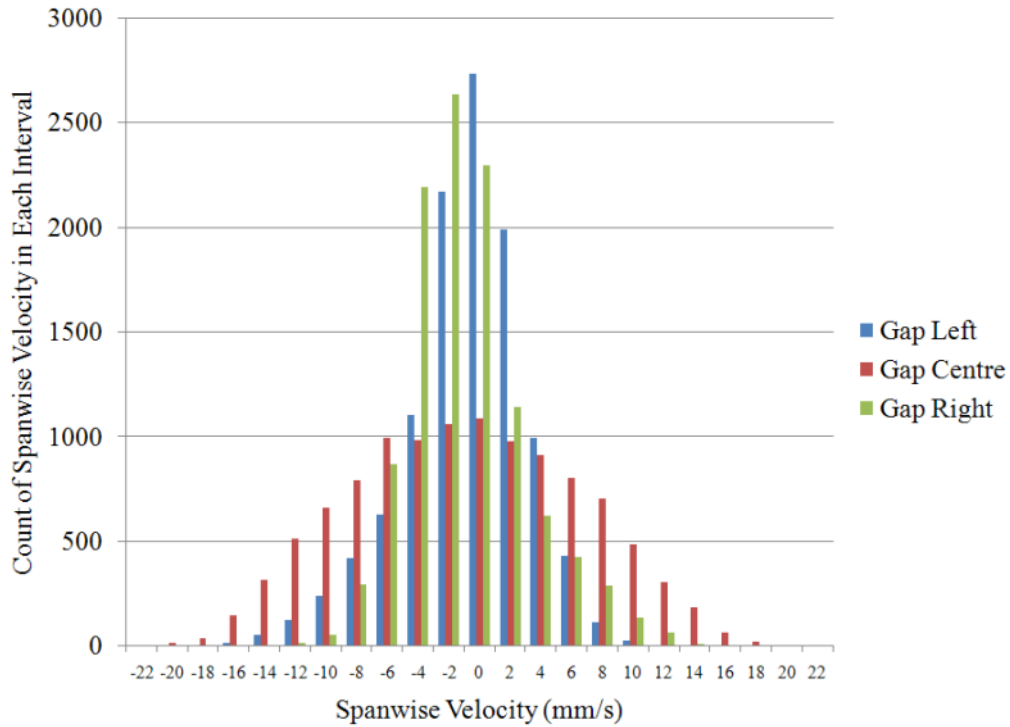


Figure 4.16: Distribution of Spanwise Velocity for $Re = 955$. Approximately 11,000 data points were used for the distribution.

For all Reynolds numbers and locations, the greatest concentration of points is around zero mm/s. All Reynolds numbers show a close to symmetrical velocity distribution for the gap centre point, whereas the points at the edges of the gap have a skewed velocity distribution consistent with the visual observation from the time traces. The distribution for the edges of the gap are more sharply peaked, with 75-80% of their velocities between -4 and 4 mm/s. As was also seen in the time traces shown figures 4.5, 4.8 and 4.11, the left edge of the gap is skewed slightly towards negative velocities, with the right edge of the gap (figures 4.6, 4.9 and 4.12) being skewed slightly towards positive velocities (i.e., skewed towards velocities that direct the gap fluid into the subchannel). For most Reynolds numbers, the gap centre has greater extent of both negative and positive velocities than either of the gap edges. The range of data obtained for the point at the left of the gap is higher than the range for the right of the gap, except for $Re = 718$, where it is the same. As the finer details of the graphs can be hard to read, due to the large scale, the maximum and minimum velocity ranges are summarized below in table 4.2.

Table 4.7: Summary table of maximum and minimum spanwise velocities observed in figures 4.14, 4.15 and 4.16

Re = 718			
Location	Left	Centre	Right
Max (mm/s)	6 to 8	16 to 18	12 to 14
Min (mm/s)	-14 to -16	-14 to -16	-8 to -10
Re = 900			
Location	Left	Centre	Right
Max (mm/s)	14 to 16	20 to 22	16 to 18
Min (mm/s)	-14 to -16	-18 to -20	-8 to -10
Re = 955			
Location	Left	Centre	Right
Max (mm/s)	16 to 18	20 to 22	16 to 18
Min (mm/s)	-18 to -20	-20 to -22	-10 to -12

Looking at both the time traces of spanwise velocity and the distribution of the velocities within the time traces, there seems to be some skewness to them for points on the edges of the gap. Figures 4.17, 4.18 and 4.19 are plots of the skewness for each Reynolds number.

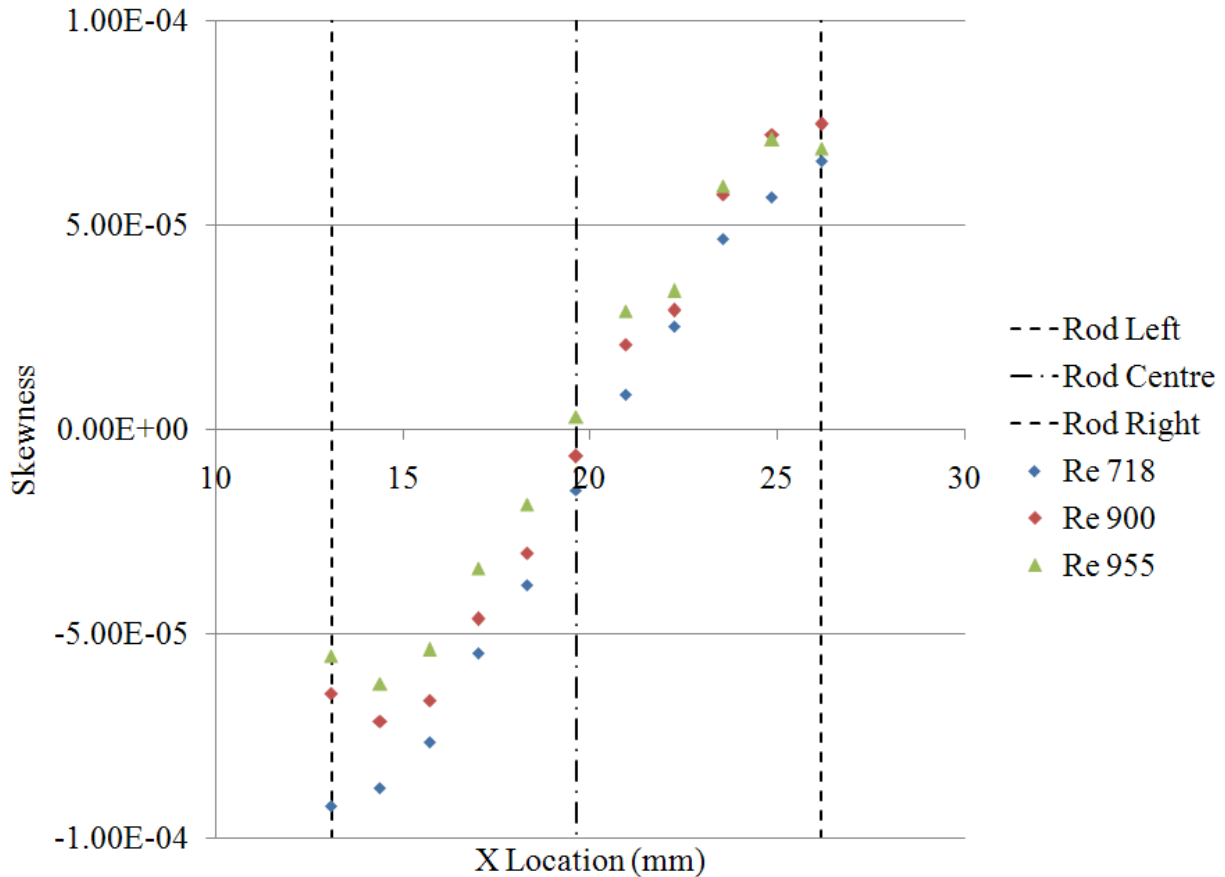


Figure 4.17: Skewness plot for Re = 718, 900 and 955. Approximately 11,000 data points were used for each distribution.

The sample skewness is calculated as:

$$Skew = \frac{\frac{1}{n} \sum_{i=1}^n (x_i - \bar{x})^3}{\left(\frac{1}{n} \sum_{i=1}^n (x_i - \bar{x})^2 \right)^{3/2}}$$

A positive skewness value indicates that there is a longer tail in the distribution where values are greater than the mean, with the bulk of the values being less than the mean. The opposite is true for a negative skewness value.

The skewness plots in figure 4.17 show data from a set of points at the midpoint of the gap, starting at the left edge and ending at the right edge, the same points shown in figure 3.4. Each point is one tenth of a rod diameter away from the next. As expected from the velocity distribution plots and time traces, the skewness goes from a negative value at the left of the gap to a positive value at the right of the gap. At the centre of the gap, the skewness is never exactly zero, but is always very close to being zero. Overall, the values of skewness are extremely low, probably due to the high density of points in regions close to zero, as seen in the velocity distribution plots. The skewness plots moves further away from a straight line fit as the Reynolds number increases. For $Re = 900$, the minimum skewness is found one tenth of a rod diameter inside the left gap. For $Re = 955$, both the minimum and maximum skewness are found one tenth of a rod diameter inside the gap.

A frequency analysis of the spanwise velocity transients was performed through application of a discrete fast Fourier transform. As mentioned in section 3.3.1, these timesteps were 0.05 seconds, 0.04 seconds 0.03 seconds for $Re = 718$, 900 and 955 respectively. The maximum frequencies which could be observed for each Reynolds number are 10 Hz, 12 Hz and 16 Hz. The time trace for the frequency analysis was taken from the centre of the gap, with at least 225 seconds of true transient time being used for each Reynolds number. The plots of the fast Fourier transform are shown below in figures 4.20, 4.21 and 4.22 for Reynolds numbers of 718, 900 and 955 respectively. Although the maximum frequency which can be observed is about ten hertz, there is no significant content above two hertz.

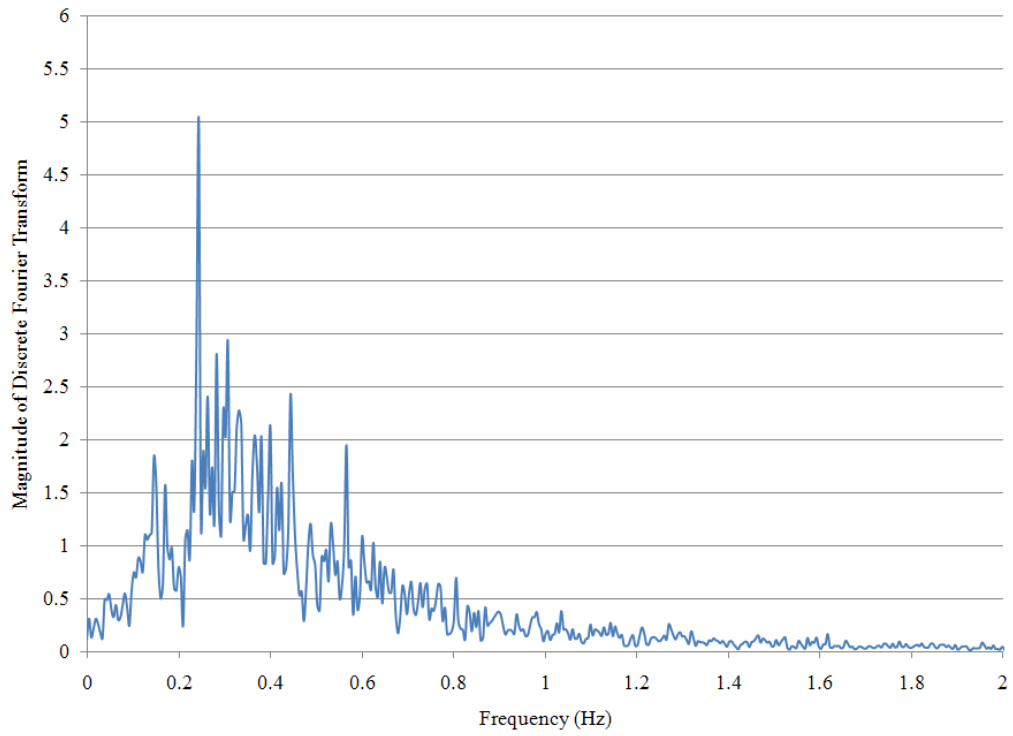


Figure 4.18: Discrete Fourier transform of the spanwise velocity time trace for $Re = 718$

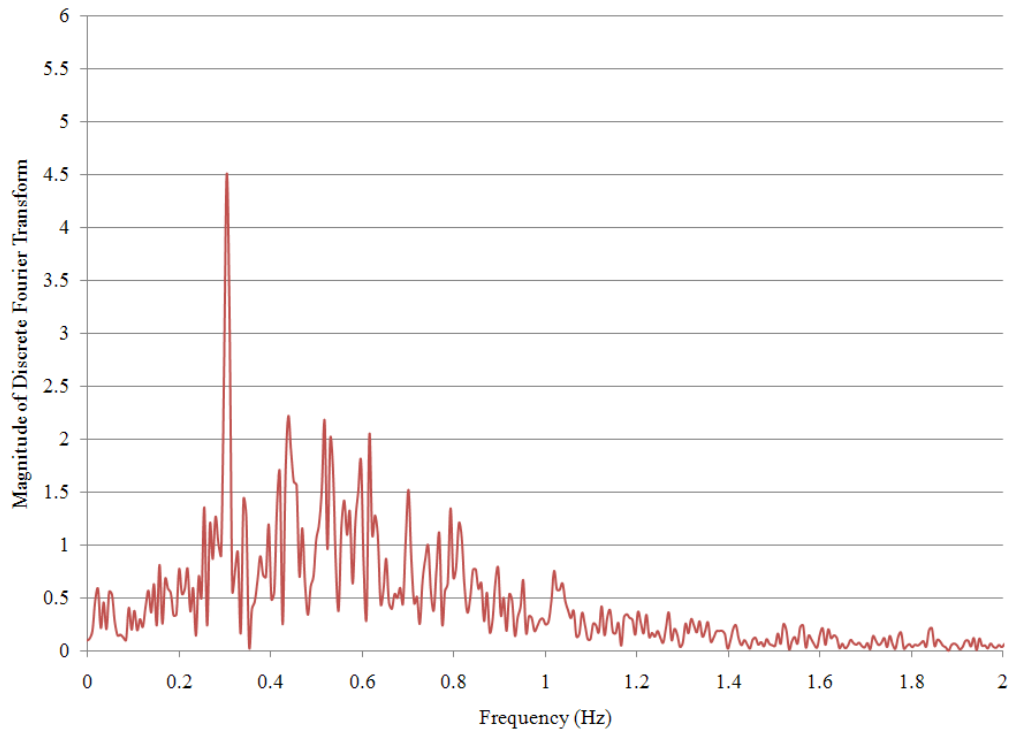


Figure 4.19: Discrete Fourier transform of the spanwise velocity time trace for $Re = 900$

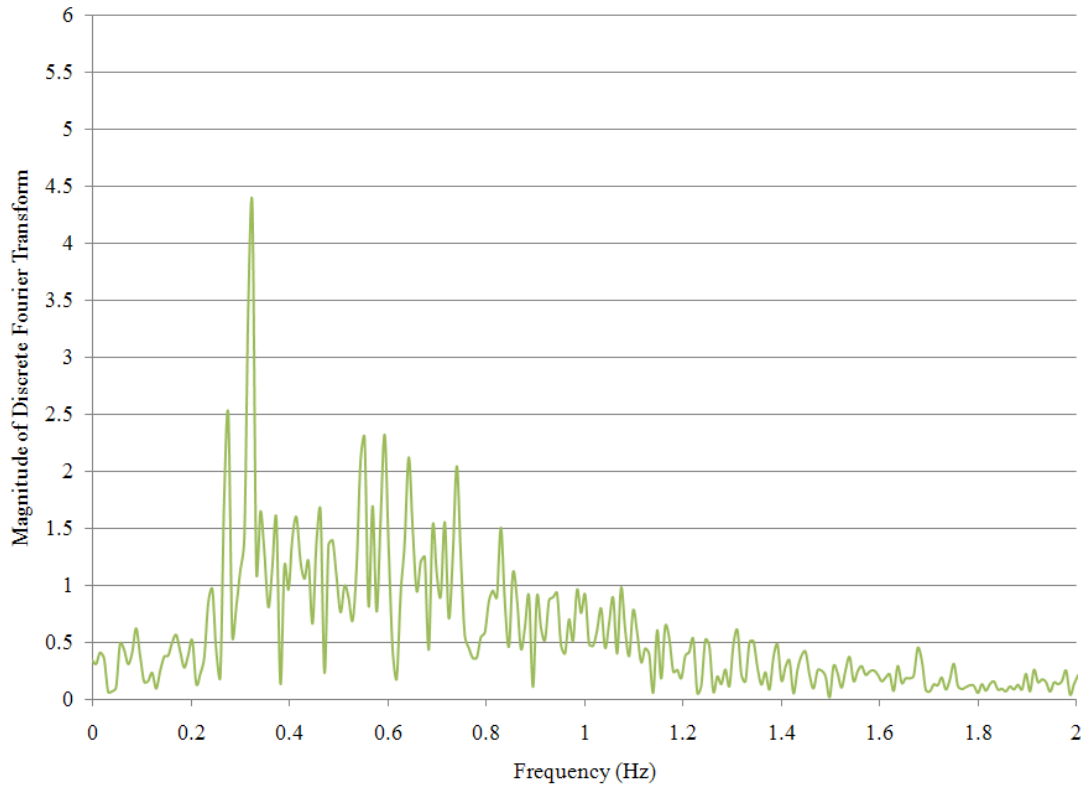


Figure 4.20: Discrete Fourier transform of spanwise velocity time trace for $Re = 955$.

Each graph shows a dominant frequency, with additional smaller frequency peaks also observed. The dominant frequencies are: $F_{Re718} = 0.24$ Hz, $F_{Re900} = 0.31$ Hz and $F_{Re955} = 0.33$ Hz. When the frequencies are non-dimensionalized by rod diameter (D) and bulk velocity (U_b), the Strouhal numbers, $St = \frac{fD}{U_b}$, are all 0.092. Gosset and Tavoularis [53] used dye streaks as a means to estimate the frequency of the pulsations by counting the number of directional changes the dye made in the spanwise direction during a given period of observation. This gave an average estimate of frequency, with a reported average standard deviation of 20%. Table 4.3 on the next page compares the percent increase in Reynolds number against the percent increase for the experimental and predicted frequencies.

Table 4.3 Comparison between experimental and predicted frequencies and Strouhal numbers.

Re	Increase	F _{Pred}	Increase	F _{Exp}	Increase	St _{Pred}	St _{Exp}
718	N/A	0.24 Hz	N/A	0.18 Hz	N/A	0.092	0.069
900	125%	0.31 Hz	125%	0.25 Hz	139%	0.092	0.075
955	106%	0.33 Hz	106%	0.28 Hz	112%	0.092	0.079

The predicted frequencies are 18 to 33% higher than those measured by Gosset and Tavoularis [53], who reported an experimental standard deviation of 20% in the precision of their method. They give no discussion as to the accuracy of their method for calculating frequency. The error in the numerical predictions of velocity can be roughly approximated by looking at the independence studies conducted, presented in section 3.3.1. The independence tests for the spatial grid found a maximum difference of 3.8% with the grid used in the present simulations compared to a grid which was twice as fine in each direction. The temporal grid showed a maximum difference of 1.6 % when using a timestep which was half of that used in the reported simulations. The experimental and predicted frequencies were calculated in a different manner, one based on the period seen in a dye streak and the other based on the spanwise velocity at a midgap point. It is not known how this affects the frequencies determined. A plot showing the Reynolds number vs Strouhal number for Gosset and Tavoularis [53], Meyer and Rehme [46] and the present numerical data is shown on the next page in figure 4.21.

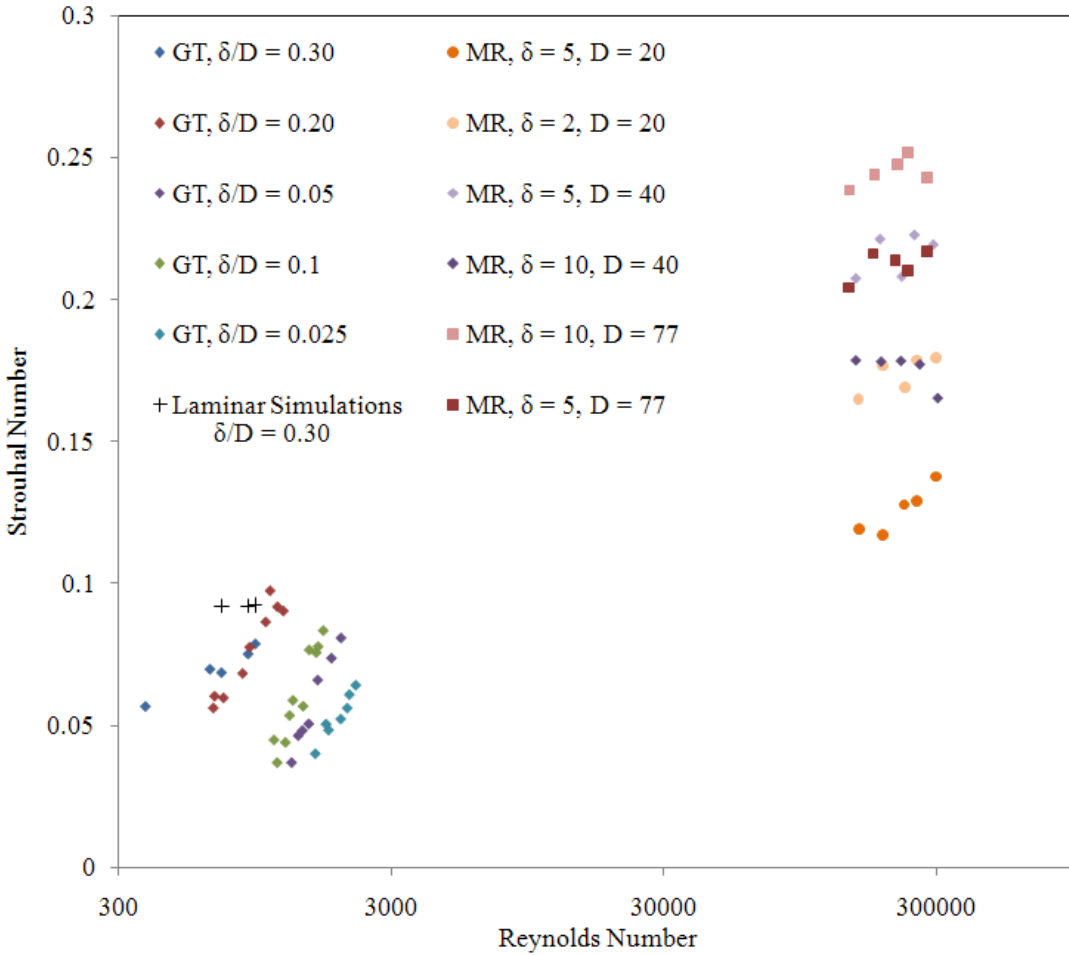


Figure 4.21: Strouhal number vs Reynolds number for the combined work of Gosset and Tavoularis (GT) [53], Meyer and Rehme (MR) [46] and the present work. The Strouhal number for all cases is based on D , the rod diameter for Gosset and Tavoularis and the width of the gap for Meyer and Rehme. Gap height is denoted by δ for all cases. The Reynolds number for all cases is based on the bulk velocity and hydraulic diameter of the domain. The Reynolds number reported by Meyer and Rehme was modified to fit this definition.

The predicted Strouhal numbers are in the same ranges that Gosset and Tavoularis [53] found for laminar flow, but like the frequencies, are over predicted. The predicted Strouhal numbers are constant over the range of Reynolds numbers simulated for the given gap size, unlike the roughly linear trend observed by Gosset and Tavoularis [53]. Gosset and Tavoularis [53] believe that pulsations start at a critical Reynolds number and Strouhal number, with a linear increase until an

asymptote at a high Reynolds number. They see this trend as resembling two dimensional cross flow past bluff bodies.

4.4 Sensitivity to Domain Length

One other source of error in the numerical predictions is the sensitivity of the predictions to the domain length. This arises from the use of periodic boundary conditions at the inlet and outlet which force there to be an integer multiple of periods of pulsations in the domain and previous work (Home et. al [62]) indicated that there can be a sensitivity to domain length. The effect is investigated here, using the $Re = 718$ case to see how many periods were found as domain length increased. Dividing the domain length by the number of periods will give the average wavelength. The following lengths used in the analysis: 352 mm, 428 mm, 492 mm, 576 mm, 652 mm, 764 mm, 892 mm, 1032 mm, representing non-integer divisors of the full domain length, 1168 mm.

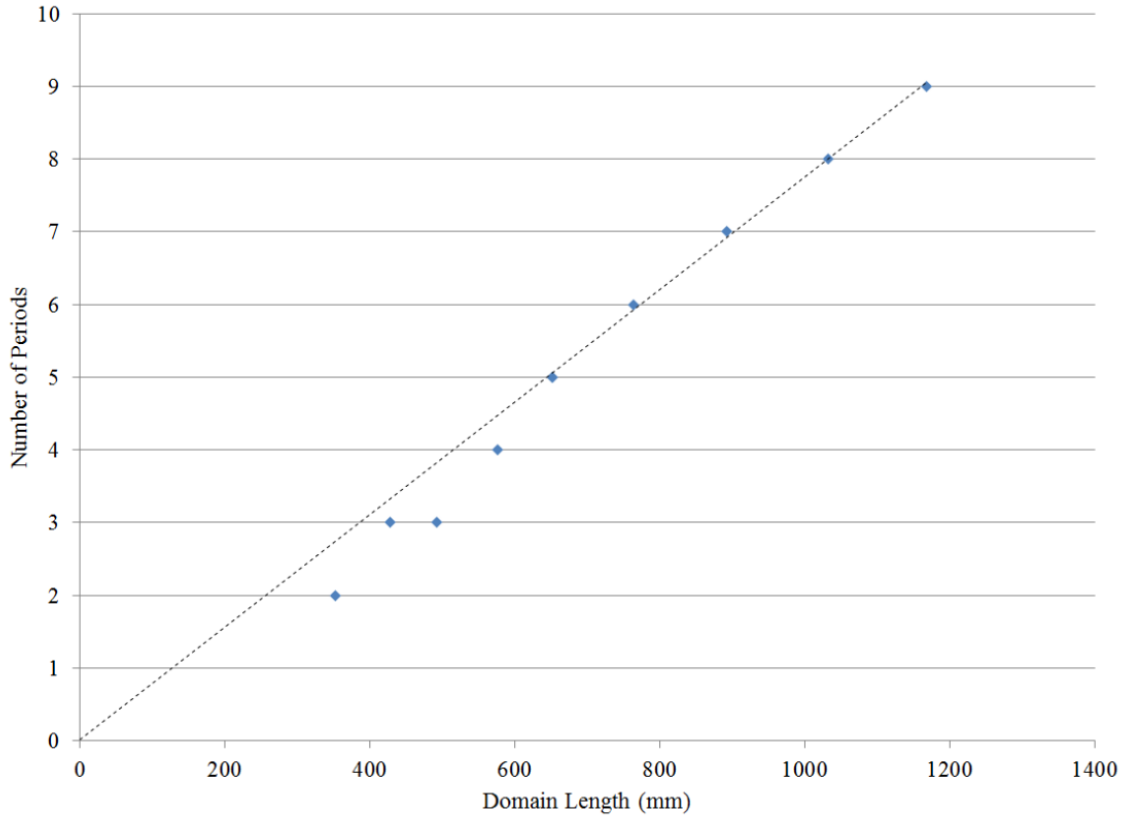


Figure 4.22: Number of periods of spanwise velocity vs domain length. Reynolds number for all cases was 718

As the domain length increases, the number of periods increases, which is exactly what would be expected. This trend would obviously continue if the length is increased beyond the limit of the experimental domain length. However, as the domain length increases, it is easier for a more constant wavelength to fit the length, which is the trend seen in figure 4.24. For L/D_H greater than approximately 30, corresponding to a length of 652 mm, the slope remains constant, as indicated by the dashed line on figure 4.22. For domain lengths greater than 652, the predicted wavelength should hold constant. This is shown in figure 4.23. This means that for the actual length of 1168 mm used in the numerical simulations for which detailed results are presented, the predictions are independent of domain length.

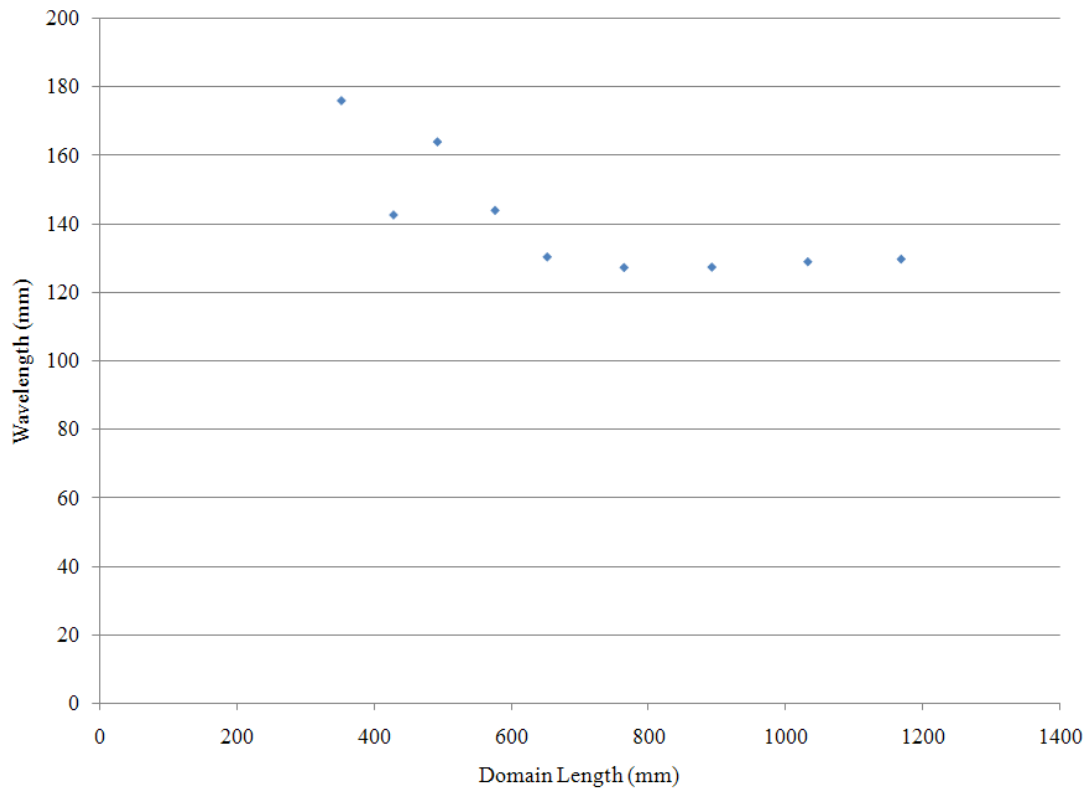


Figure 4.23: Average wavelength of spanwise velocity vs domain length. Reynolds number for all lengths is 718.

4.5 Particle Track Data

Since Gosset and Tavoularis [53] used dye streak images not only to characterize their flow, but also to give a visual representation of how the pulsations were behaving, another method of comparing the numerical predictions with experimental data is to use particle tracks, released at the same point where Gosset and Tavoularis released their dye. The images shown below in figures 4.24, 4.25 and 4.27 display tracks of mass less particles which were released at each timestep, at the centre point of the gap.



Figure 4.24: Particle tracks for $Re = 718$. Image is looking down on the domain, flow from left to right. Dashed black lines indicate location of the rod. Tracks are shown for particles over a time span of 2.25 seconds, starting at 70 seconds into the true transient. The particle tracks were set to stop once the particles had travelled about 750 mm.

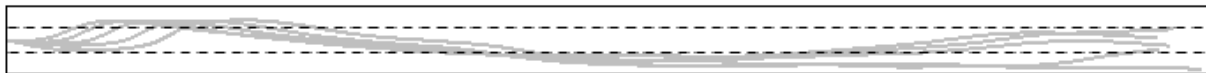


Figure 4.25: Particle tracks for $Re = 900$. Image is looking down on the domain, flow from left to right. Dashed black lines indicate location of the rod. Tracks are shown for particles over a time span of 1.8 seconds, starting at 75 seconds into the true transient. The particle tracks were set to stop once the particles had travelled about 750 mm.

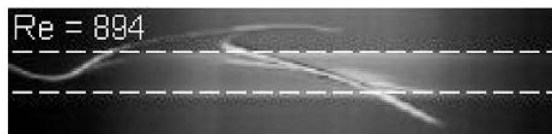


Figure 4.26: Dye streak image from Gosset and Tavoularis [53] for a Reynolds number of 894. Flow is from left to right. White dashed lines indicate rod position. Image is looking down on the domain.

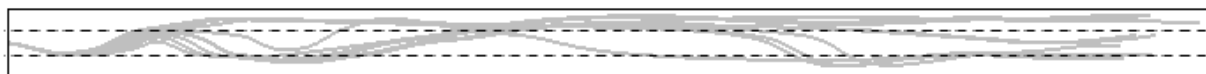


Figure 4.27: Particle tracks for $Re = 955$. Image is looking down on the domain, flow from left to right. Dashed black lines indicate location of the rod. Tracks are shown for particles over a time span of 0.3 seconds, starting at 85 seconds into the true transient. The particle tracks were set to stop once the particles had travelled about 750 mm.

The tracks for all three Reynolds numbers show that particles which are released in the middle of the gap are able to travel to both sides of the domain. They also demonstrate that within a short time span, the flow behaviour is changing enough that subsequent tracks are quite different from

each other. This is most obvious in figure 4.27, where in 0.3 seconds, particles are showing different wavelengths and movement from each other. The tracks shown for $Re = 900$ are qualitatively similar to the dye streaks observed by Gosset and Tavoularis [53], shown in figure 4.26.

The particle tracks may also be used to estimate wavelengths within the domain. These are defined as a particle which starts in the middle of the gap and moves in and out of the gap. The end point is defined as when the particle crosses through the middle of the gap a second time. Visual inspection of the images shows that there are quite different wavelengths between the different tracks, as well as within one track alone, which agrees with the frequency analysis. The visual estimates of wavelength are summarized in table 4.3 below, with the average wavelength obtained from the velocity traces given for comparison as well.

Table 4.4: Average wavelengths from particle track data

Reynolds Number	Average wavelength, particle tracks (mm)	Range of particle wavelengths (mm)	Average wavelength, velocity traces (mm)
718	313	180 - 220, 350 - 400	130
900	370	250 - 275, 530 - 555	90
955	320	110 - 175, 430 - 480	83

As can be seen from the data presented, the wavelengths found from the particle tracks are not consistent with each other. In all cases, the average wavelength sits outside of the range of wavelengths found from the tracks. More pertinently, the wavelengths obtained from the particle tracks are quite different from the wavelength obtained from the velocity traces. Correspondingly, frequencies obtained by these two methods would be different from each other.

The particle tracks obtained from the numerical results differ from the dye traces produced by Gosset and Tavoularis [53]. The dye streaks from Gosset and Tavoularis show the

instantaneous locations of many particles which were released from the same location at one instance in time. The particle tracks show the individual paths of each particle, released from the same point as the dye streaks of Gosset and Tavoularis [53]. The numerical particle tracks are essentially pathlines, whereas the dye streaks are streaklines. The pathlines will inherently carry in them the effect of the convective velocity. Direct visual comparison between the pathlines and streaklines is not possible, as they do not show the same thing.

4.6 Q-Criterion Plots and Cross-plane Visualizations

One method commonly used for visualizing vortices and coherent structures within the flow is the Q-criterion [66, 67]. The Q-criterion defines vortical structures as places in the flow where rotation dominates strain, and is calculated by taking the second invariant of the velocity gradient tensor.

$$Q = \frac{1}{2} \left(\left(\frac{\partial u_i}{\partial x_i} \right)^2 - \frac{\partial u_i}{\partial x_j} \frac{\partial u_j}{\partial x_i} \right)$$

For incompressible flows, such as exist in the present simulations, this equation may be simplified to:

$$Q = -\frac{1}{2} \frac{\partial u_i}{\partial x_j} \frac{\partial u_j}{\partial x_i}$$

From the above definition, the Q-criterion will have units of s^{-2} , given that it is calculated by multiplying two velocity gradients together. Isosurfaces of the Q-criterion are used to visualize the three dimensional nature of the flow. Subsequent series of velocity vectors on the crossplane (u and v velocity only, the axial velocity having been removed) are shown with shaded contours

of axial velocity, axial velocity gradient and pressure to understand how the flow structure relates to these different parameters.

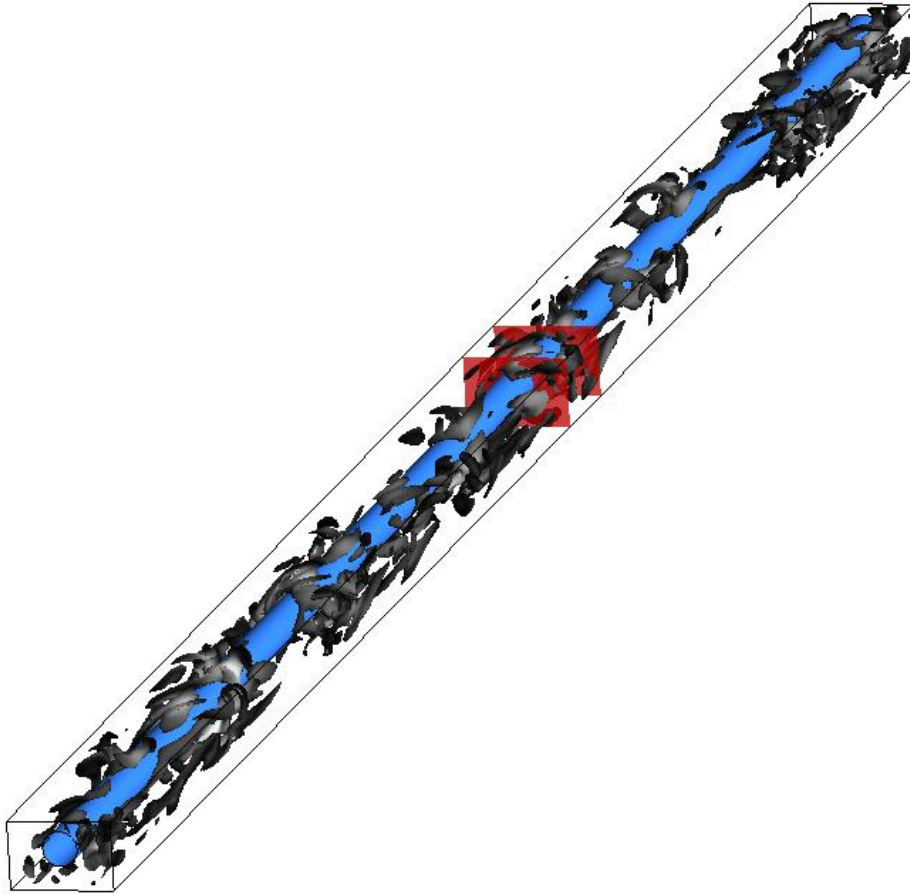


Figure 4.28: Isosurface plot of Q-criterion for $Re = 718$, 70 seconds into the true transient. $Q = 0.75 \text{ s}^{-2}$. Bulk flow is from bottom left to top right. The red planes show where the visualizations of figures 4.29 to 4.31 and 4.35 to 4.37 are taken. Figures 4.32 - 4.34 are taken in between the planes.

A snapshot of a Q-isosurface is shown in figure 4.28. Vortical structures can be seen throughout the domain, which are axially elongated and wrap around the rod. A gap vortex street [14,15,16] is not readily apparent in this flow. The amount of vortical structures and their interaction with each other is much more complex than typically would be expected from laminar flow.

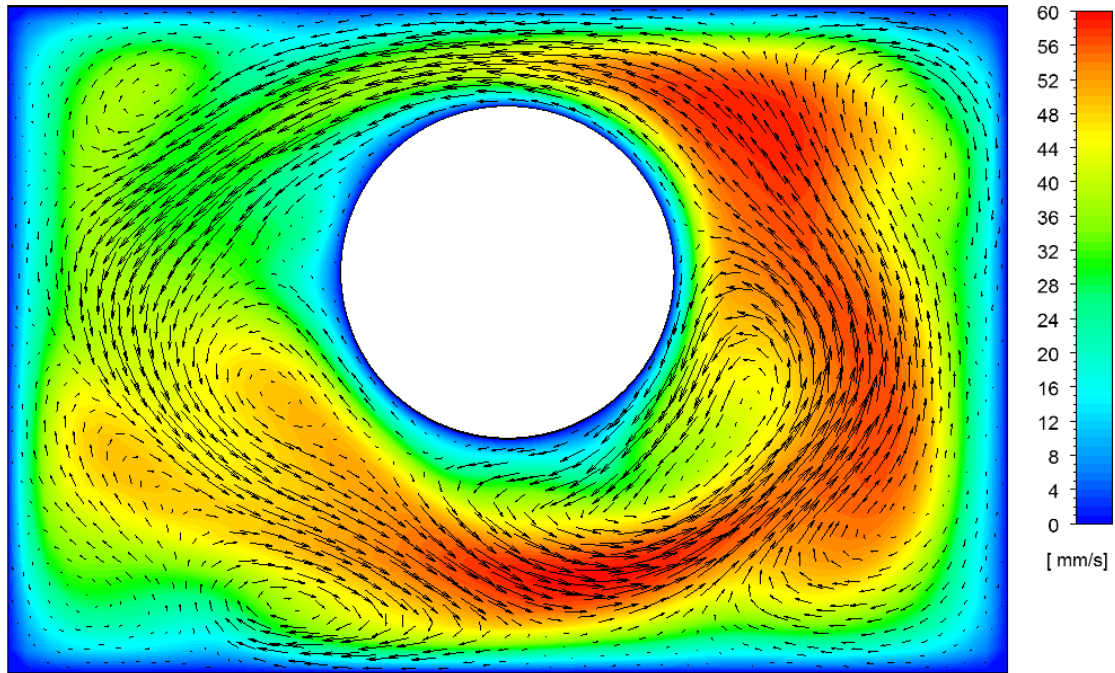


Figure 4.29: Vector plot of crossplane velocity (u and v) with shaded contours of axial velocity behind for $Re = 718$. Flow direction is into the page. Location is approximately 665 mm downstream of inlet, taken after 70 seconds of true transient time has elapsed.

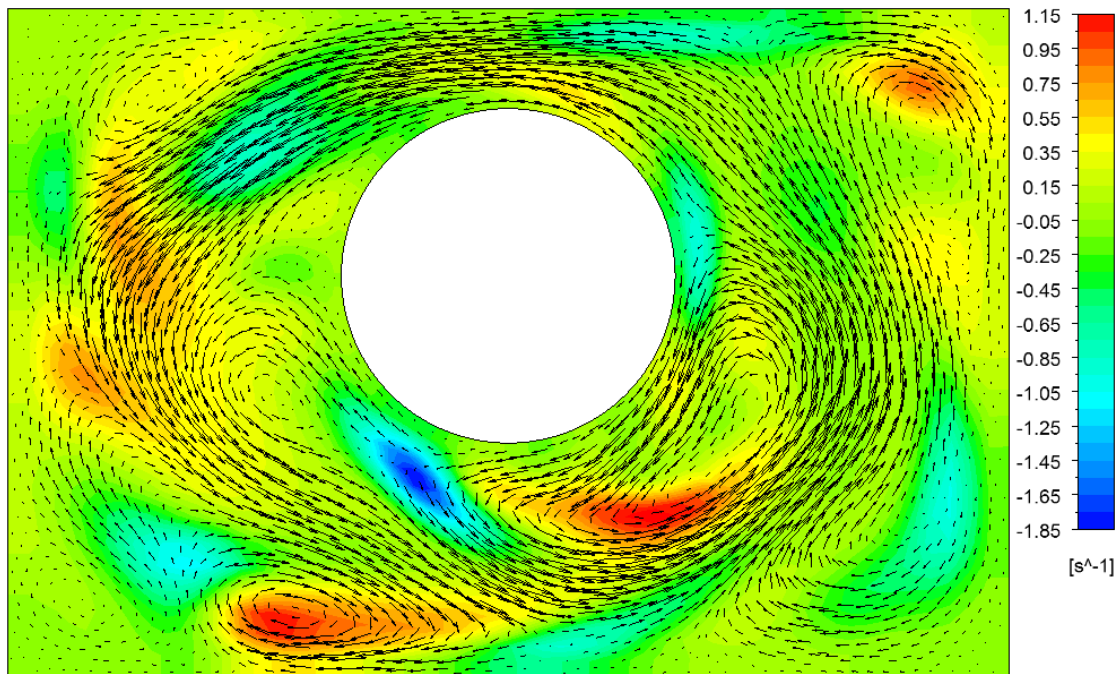


Figure 4.30: Vector plot of crossplane velocity (u and v) with shaded contours of axial velocity gradient behind for $Re = 718$. Flow direction is into the page. Location and time are the same as in figure 4.29.

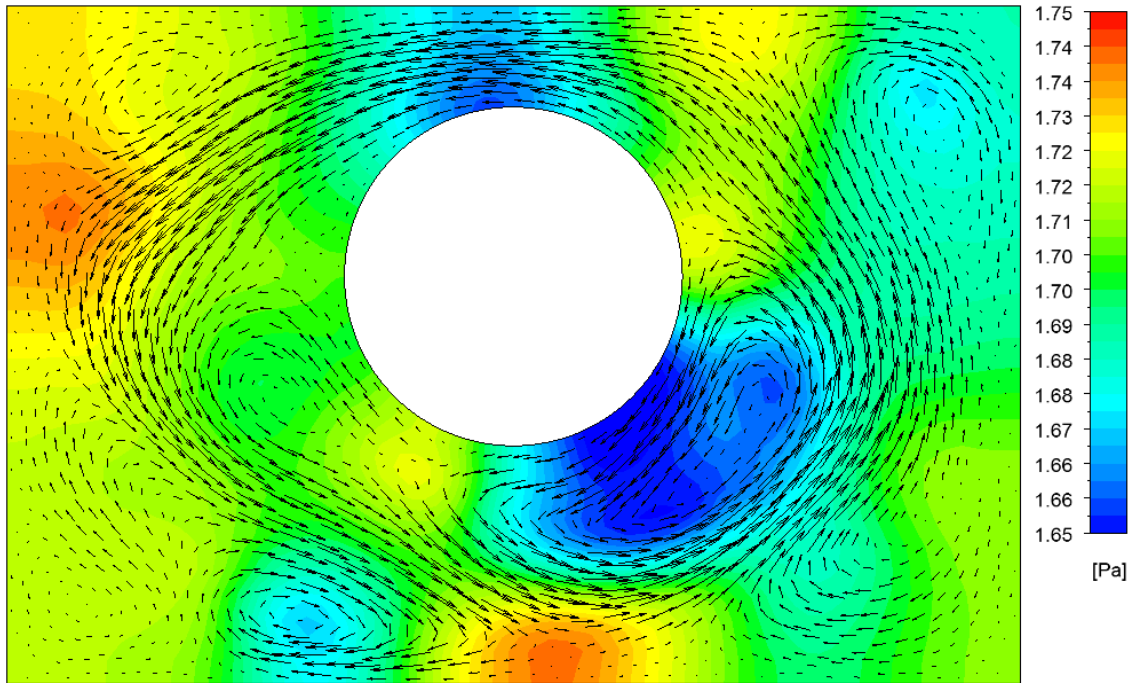


Figure 4.31: Vector plot of crossplane velocity (u and v) with shaded contours of pressure behind for $Re = 718$. Flow direction is into the page. Location and time are the same as in figure 4.29.

Figures 4.29 to 4.31 show that the flow does not merely pulse in and out of the gap, but circulates around the rod. In this case, it is circulating counter-clockwise. The flow exiting the gap is extremely strong. Where the flow has detached from the rod, circulation zones can be seen. These also exist near most of the corners. There is quite strong flow between the two recirculation zones in the right subchannel. This is a place where flow is starting to increase in velocity on the crossplane, towards the gap. The axial velocity is strongest below the rod and in the right subchannel, when it is moving into the gap. Upon exiting the gap, the axial velocity is considerably weaker.

The axial velocity gradient has a total change of about 3 s^{-1} in this snapshot. The distribution is centred about -0.2 s^{-1} . Most of the domain has close to zero axial velocity gradient, shown by light green. At the bottom of the rod, the axial velocity is decreasing (dark blue) coinciding with flow increasing in the crossplane. The pressure in the domain has a total change

of 0.10 Pa. The majority of the domain is close to the average pressure of 1.70 Pa, shown by the light green colour. Areas of lowest pressure are found in the left gap region and the bottom right of the rod. The area of low pressure near the bottom right of the rod corresponds to smaller area of positive axial velocity gradient.

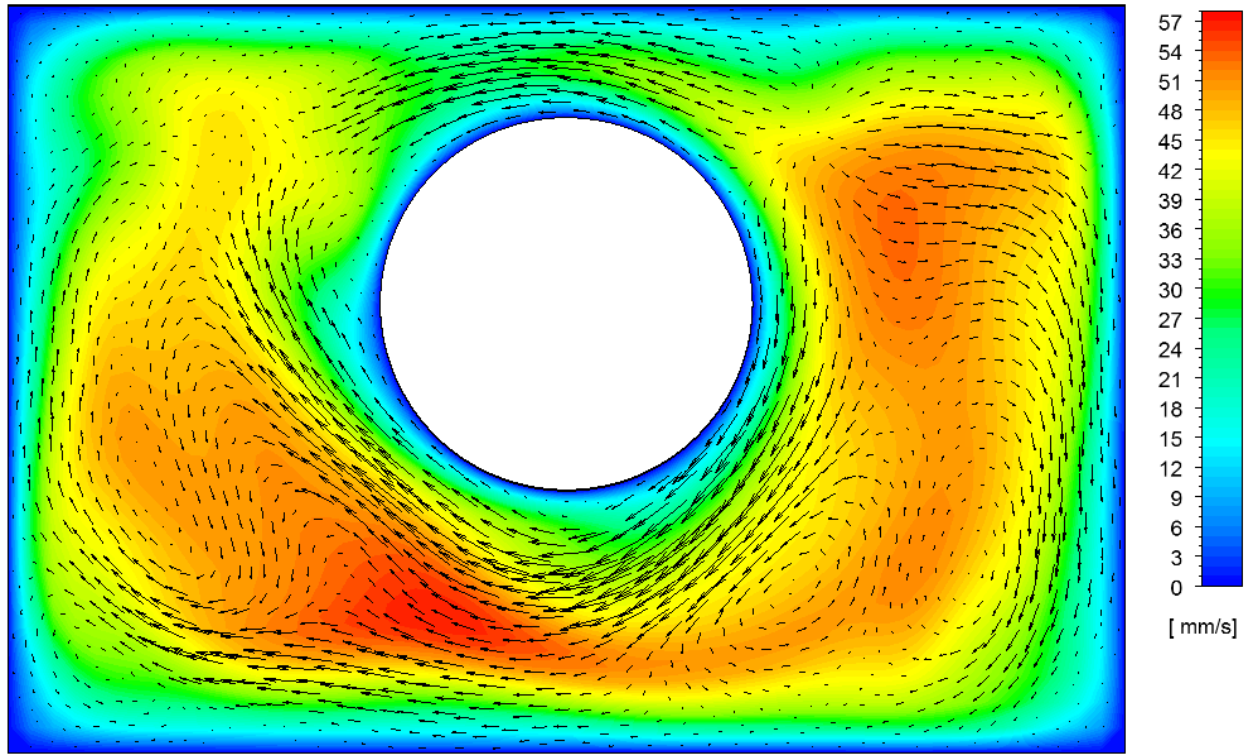


Figure 4.32: Vector plot of crossplane velocity (u and v) with shaded contours of axial velocity behind for $Re = 718$. Flow direction is into the page. Location is approximately 22 mm downstream of figure 4.29, taken after 70 seconds of true transient time has elapsed.

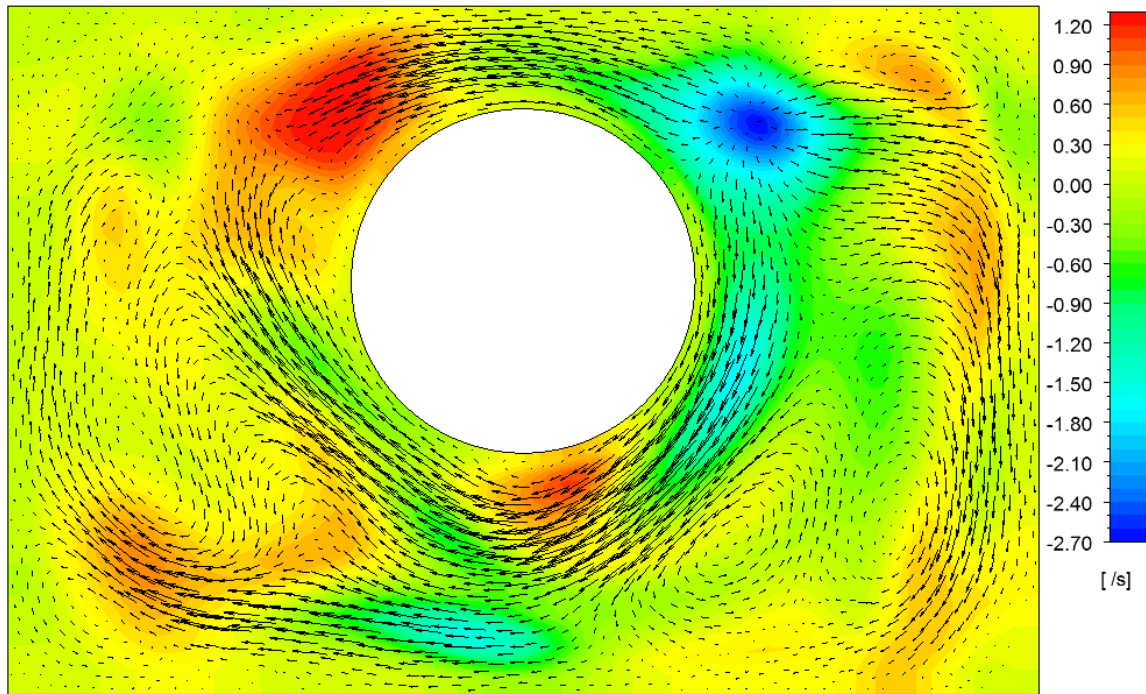


Figure 4.33: Vector plot of crossplane velocity (u and v) with shaded contours of axial velocity gradient behind for $Re = 718$. Flow direction is into the page. Location and time are the same as in figure 4.32

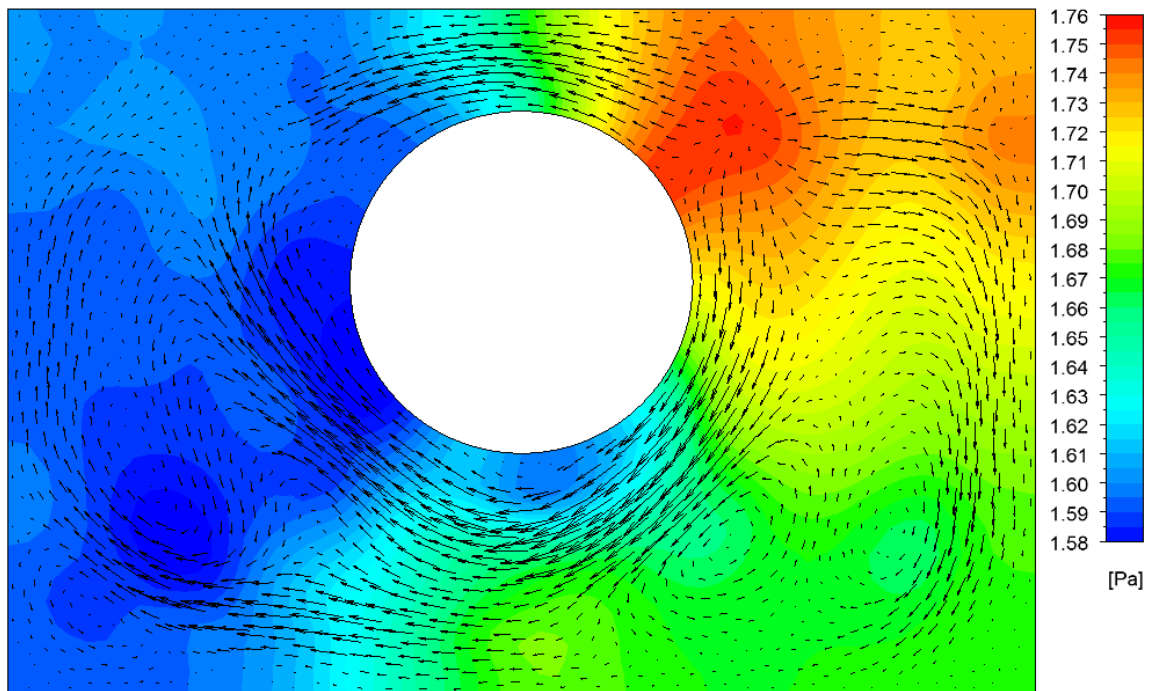


Figure 4.34: Vector plot of crossplane velocity (u and v) with shaded contours of pressure behind for $Re = 718$. Flow direction is into the page. Location and time are the same as in figure 4.32.

The flow on this crossplane (figures 4.32 to 4.34) is transitioning between pulsation directions and does not have a single rotational direction to it. The strongest flow is seen around the bottom of the rod, in a clockwise direction. This is opposite to the direction of flow seen in figures 4.29 to 4.31. The axial velocity is strongest below the rod and weakest through the gap. Within the subchannels, there is much greater equilibrium in axial velocity than was seen in figure 4.29.

The axial velocity gradient has a change of approximately 3 s^{-1} , the same as in figure 4.32. Maximum value is approximately half of the absolute value of the minimum value, with the distribution centred around -0.70 s^{-1} . Despite having quite large negative values, the majority of the plane has an axial velocity gradient of approximately 0.30 s^{-1} , shown by yellow. The extrema are located on either side of the gap. The minimum is on the right side of the gap where the axially flowing fluid slows down, due to the high pressure region. This high pressure results in fluid moving radially in the crossplane away from the location of the high pressure core. On the left side of the gap, the flow is increasing in the axial direction which results in the crossplane fluid flow being directed towards the location where the increase in axial velocity occurs. The pressure change in the crossplane is 0.18 Pa , with the distribution being roughly split down the middle of the rod. The highest pressure is found on the right side, and corresponds to the point of lowest axial velocity gradient. The lowest pressure is found on the left side of the plane and is correlated to the point of highest axial velocity gradient.

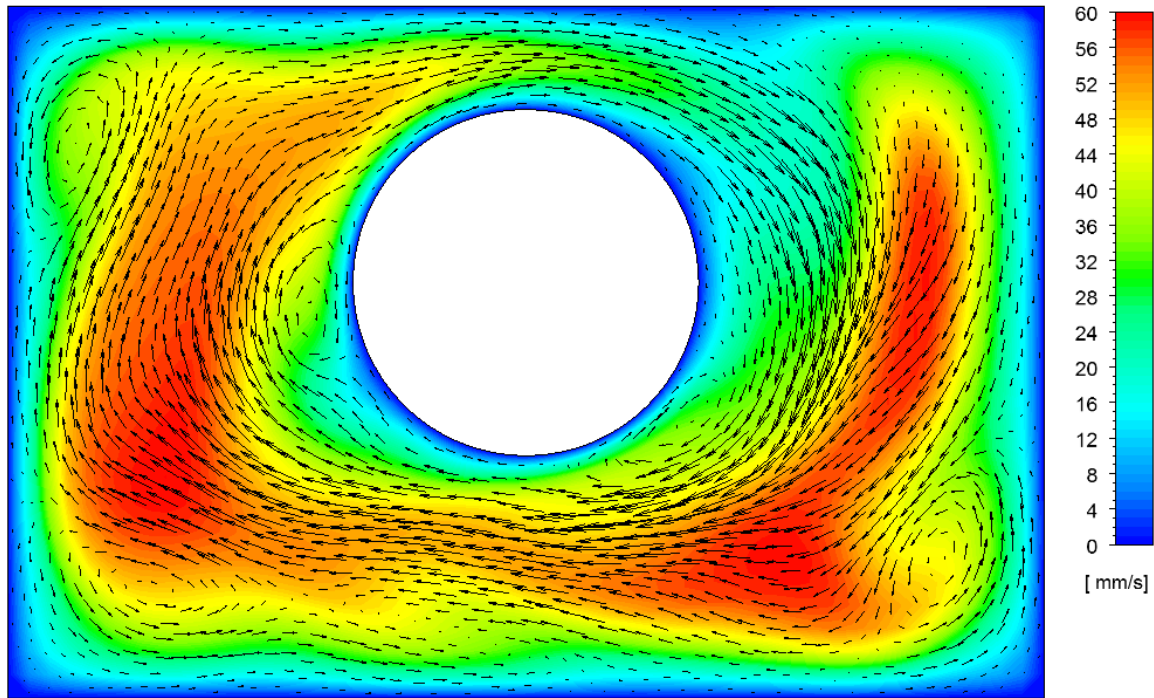


Figure 4.35: Vector plot of crossplane velocity (u and v) with shaded contours of axial velocity behind for $Re = 718$. Flow direction is into the page. Location is approximately 22 mm downstream of figure 4.32, taken after 70 seconds of true transient time has elapsed.

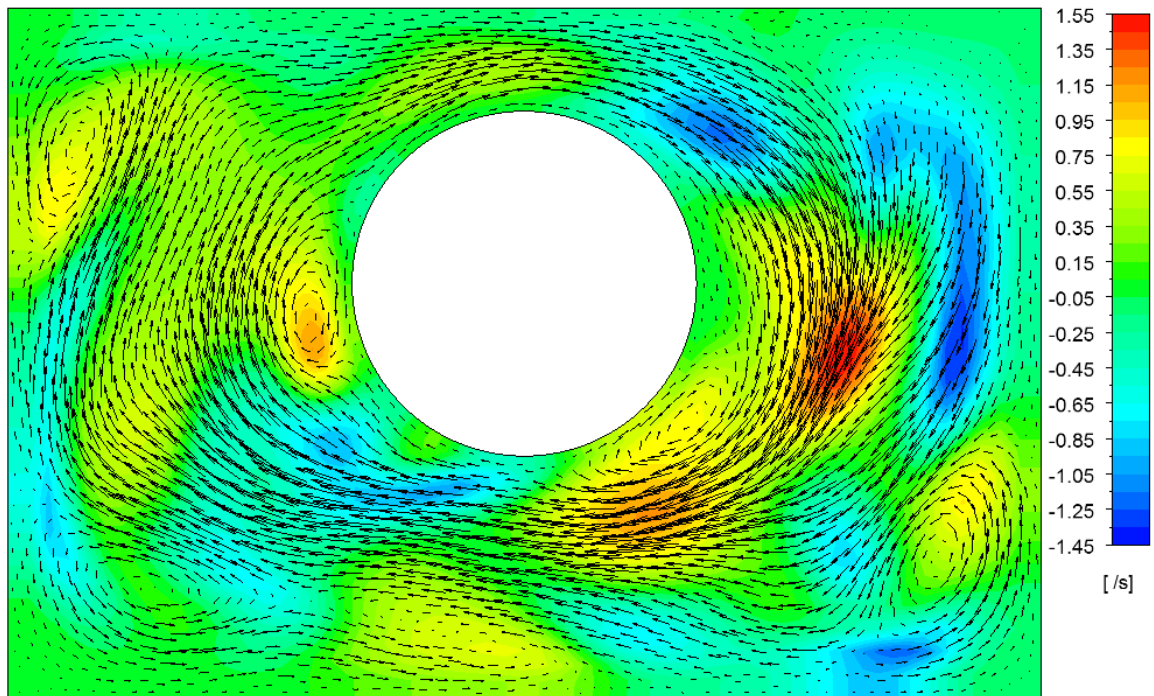


Figure 4.36: Vector plot of crossplane velocity (u and v) with shaded contours of axial velocity gradient behind for $Re = 718$. Flow direction is into the page. Location and time are the same as in figure 4.35

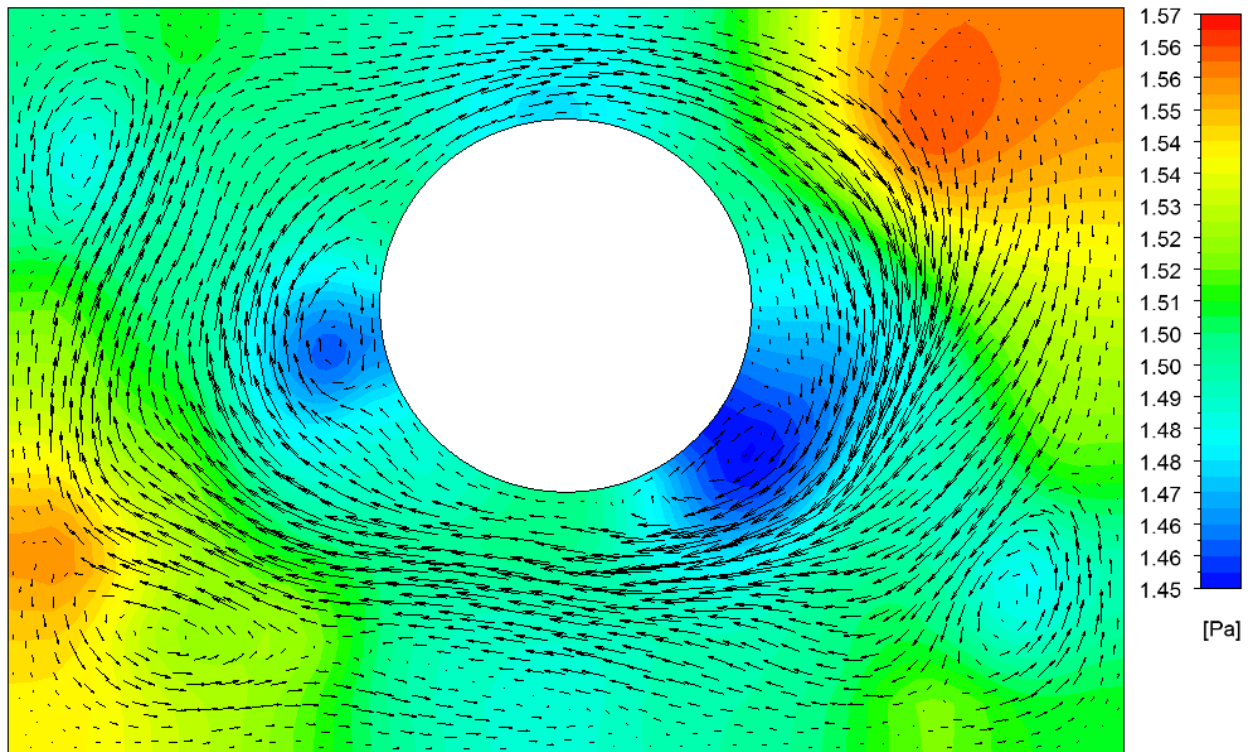


Figure 4.37: Vector plot of crossplane velocity (u and v) with shaded contours of pressure behind for $Re = 718$. Flow direction is into the page. Location and time are the same as in figure 4.35.

In figures 4.35 to 4.37, as was seen in figures 4.29 to 4.31, there is a very strong rotational direction to the flow. In figures 4.35 to 4.37, the flow rotates in a clockwise direction. As in figures 4.29 to 4.31, the flow exiting the gap is very strong and circulation zones exist where flow has detached from the rod, as well as near most of the corners. However, circulation zones near the rod in figures 4.35 to 4.37 are much smaller than the ones seen approximately 44 mm upstream (4.29 to 4.31). There is also strong flow in the secondary gap, below the rod. The axial velocity is strongest in the right subchannel, away from the gap and in the bottom of the left subchannel. As in figure 4.29, it is much weaker upon exiting the gap.

In figure 4.36, as in figures 4.30 and 4.33, the change in axial velocity gradient is 3 s^{-1} . However, the distribution is much more even than in figure 4.30 or 4.33. Most of the domain has close to zero axial velocity gradient, shown by light green. The dark blue area from figure 4.33

near the right edge of the gap is still in evidence, although it does have a much smaller magnitude.

In figure 4.37, the total change in pressure across the plane is 0.12 Pa, which is closer to the change seen in figure 4.31 than figure 4.34. The majority of the domain is close to the average pressure of 1.50 Pa, shown by light green. Areas of lowest pressure are found on either side of the rod, and are near the centre of the recirculation zones near the rod. The high pressure regions are found in diagonally opposing corners of the domain, bottom left and top right. The top right high pressure zone corresponds to the high pressure zone seen in figure 4.34.

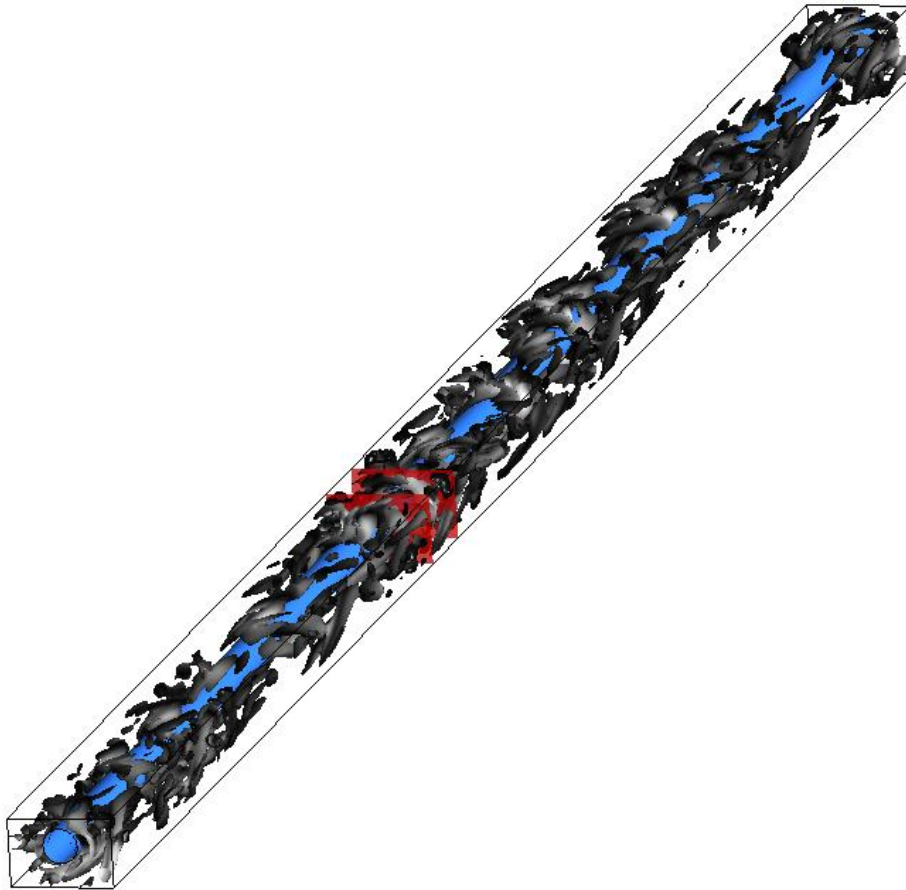


Figure 4.38: Isosurface plot of Q-criterion for $Re = 900$, 75 seconds into the true transient. $Q = 0.75 \text{ s}^{-2}$. Bulk flow is from bottom left to top right. The red planes show where the visualizations of figures 4.39 to 4.41 and 4.45 to 4.47 are taken. Figures 4.42 - 4.44 are taken in between the planes.

The three-dimensional visualization in figure 4.38 shows many more structures seen compared to figure 4.28. These structures are still wrapping around the rod, as before. Near the end of the domain, there is a region with a much lower density of structures. This region can be seen in figure 4.2b, where the total velocity shows that pulsations are less evident at that snapshot. Also, in figure 4.3b, the spanwise velocities are much smaller in this region than in the rest of the domain.

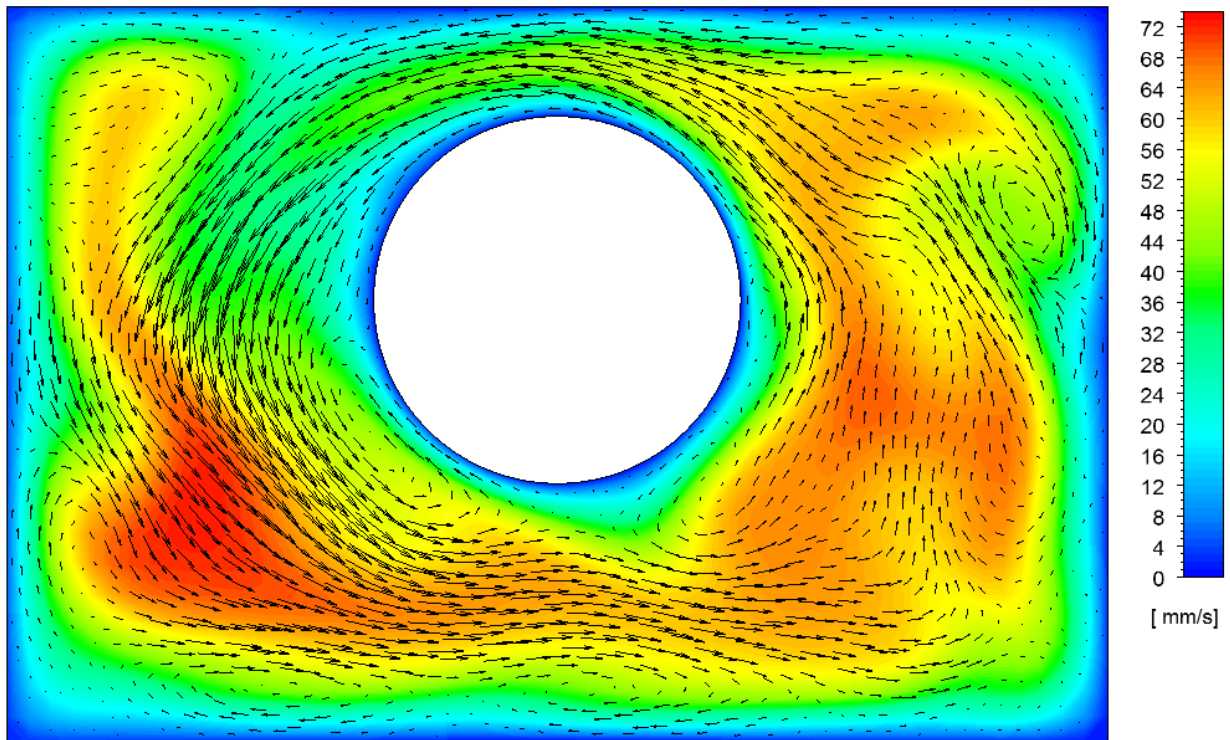


Figure 4.39: Vector plot of crossplane velocity (u and v) with shaded contours of axial velocity behind for $Re = 900$. Flow direction is into the page. Location is approximately 540 mm downstream of the inlet, taken after 75 seconds of true transient time has elapsed.

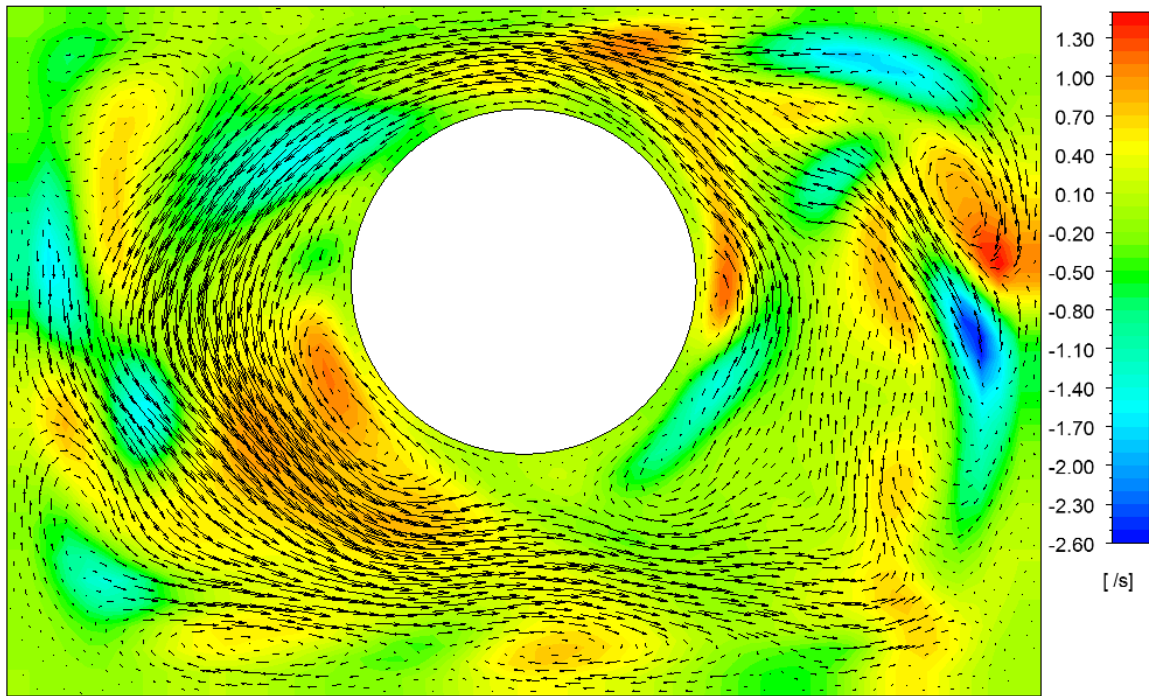


Figure 4.40: Vector plot of crossplane velocity (u and v) with shaded contours of axial velocity gradient behind for $Re = 900$. Flow direction is into the page. Location and time are the same as in figure 4.39.

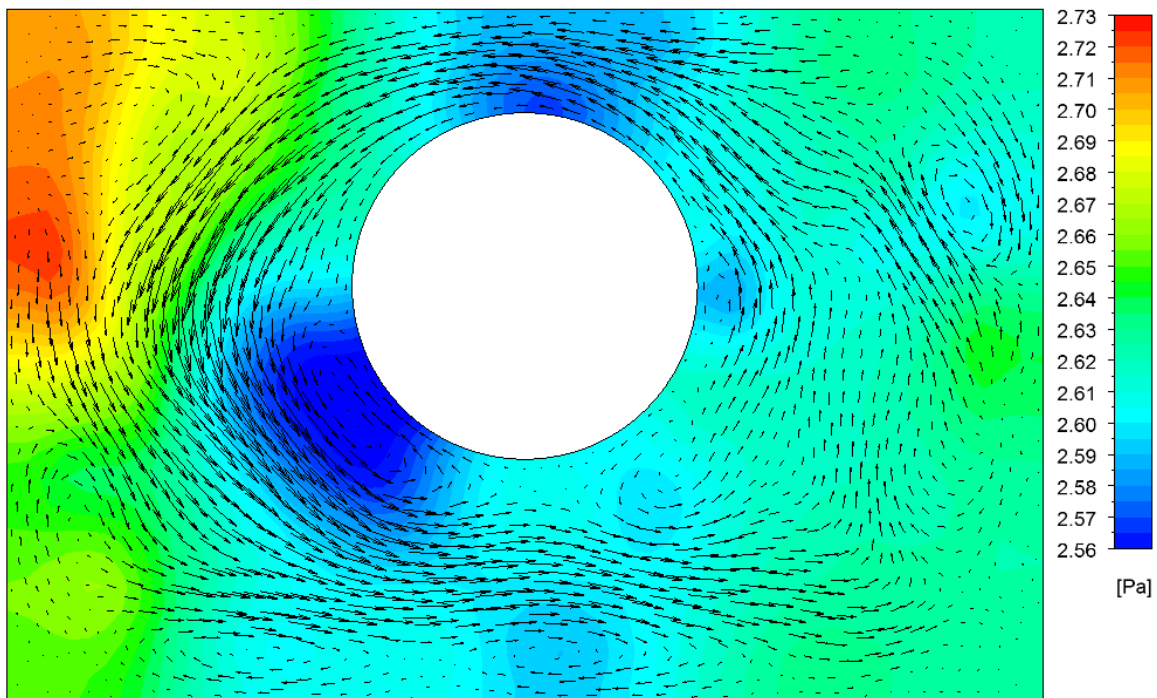


Figure 4.41: Vector plot of crossplane velocity (u and v) with shaded contours of pressure behind for $Re = 900$. Flow direction is into the page. Location and time are the same as in figure 4.39

The rotational direction of the flow in figures 4.39 to 4.41 is counter clockwise. As seen for $Re = 718$, there are circulation zones near the rod and walls. The number of circulation zones appear to have increased from $Re = 718$. Strongest crossplane flow is out of the gap and around the rod, in the bottom of the middle subchannel. The axial velocity is strong in the bottom of the left subchannel, with fairly strong flow seen in the right subchannel. It again is weakest exiting the gap region.

In figure 4.40, the change in gradient is approximately 4 s^{-1} . The largest negative values are much greater than the positive values, as was seen in figure 4.25. On the right hand side of the domain, there is a region of high gradient just above a region of low gradient. Crossplane flow seems to be coming from the region of low gradient, which concurs with momentum conservation. The flow somewhat weakens around the area of high gradient, but since the overall magnitude is still negative, there is net flow from this region. Other regions within the domain with negative axial velocity gradients producing crossplane flow can be found in the top right, the bottom right of the rod, the bottom left corner of the domain and the left side of the domain.

Pressure change seen across figure 4.41 is 0.17 Pa. Two areas of negative pressure can be found, one in the centre of the gap and one on the bottom left part of the rod. The area on the bottom left of the rod also has a circulation zone centred on it. The highest pressure seen on the left wall, extending from the middle of the rod to the top of the domain. This high pressure area pushes flow away from the wall and around the rod.

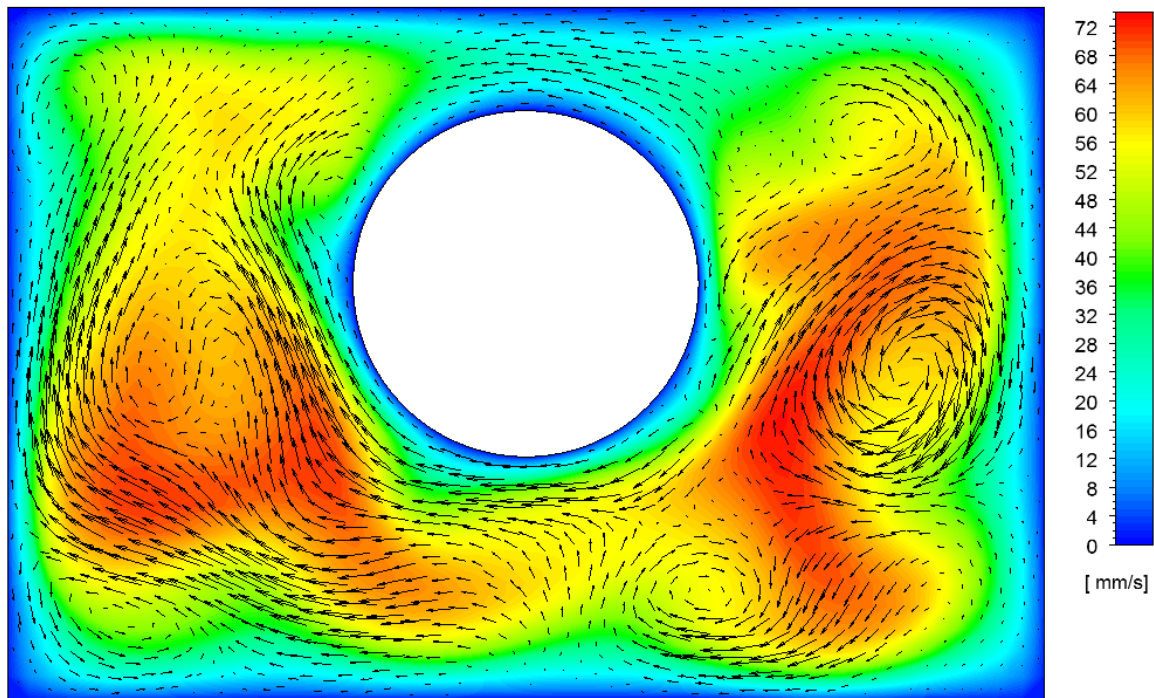


Figure 4.42: Vector plot of crossplane velocity (u and v) with shaded contours of axial velocity behind for $Re = 900$. Flow direction is into the page. Location is approximately 40 mm downstream from figure 4.39, taken after 75 seconds of true transient time has elapsed.

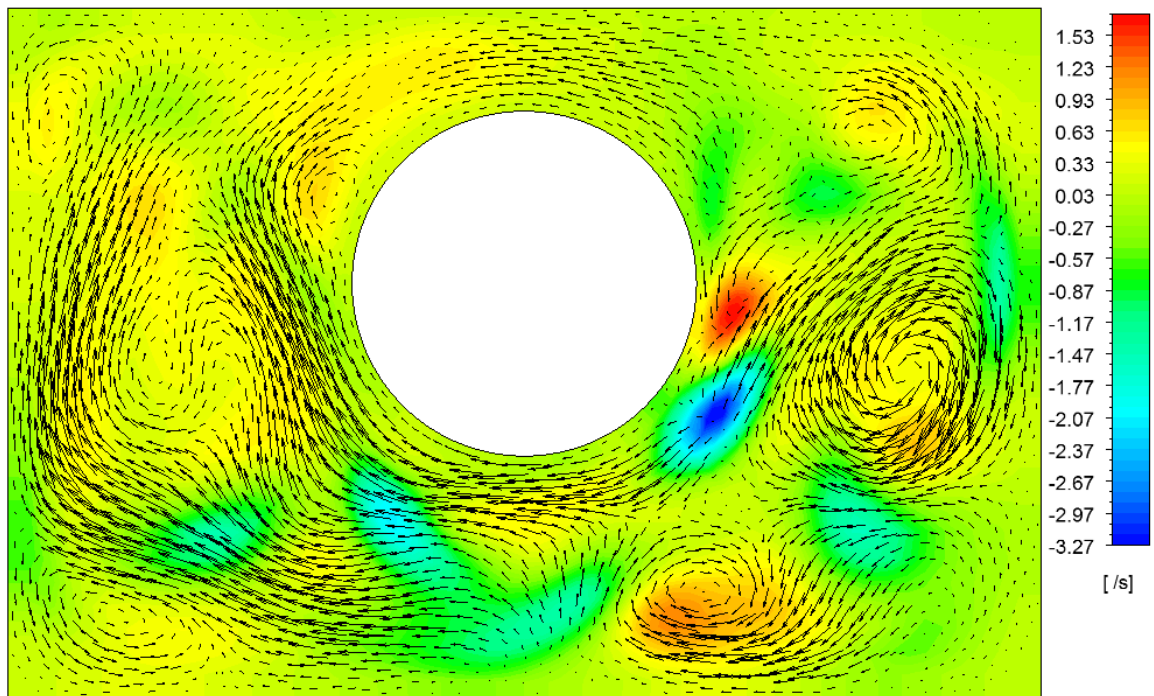


Figure 4.43: Vector plot of crossplane velocity (u and v) with shaded contours of axial velocity gradient behind for $Re = 900$. Flow direction is into the page. Location and time are the same as in figure 4.42.

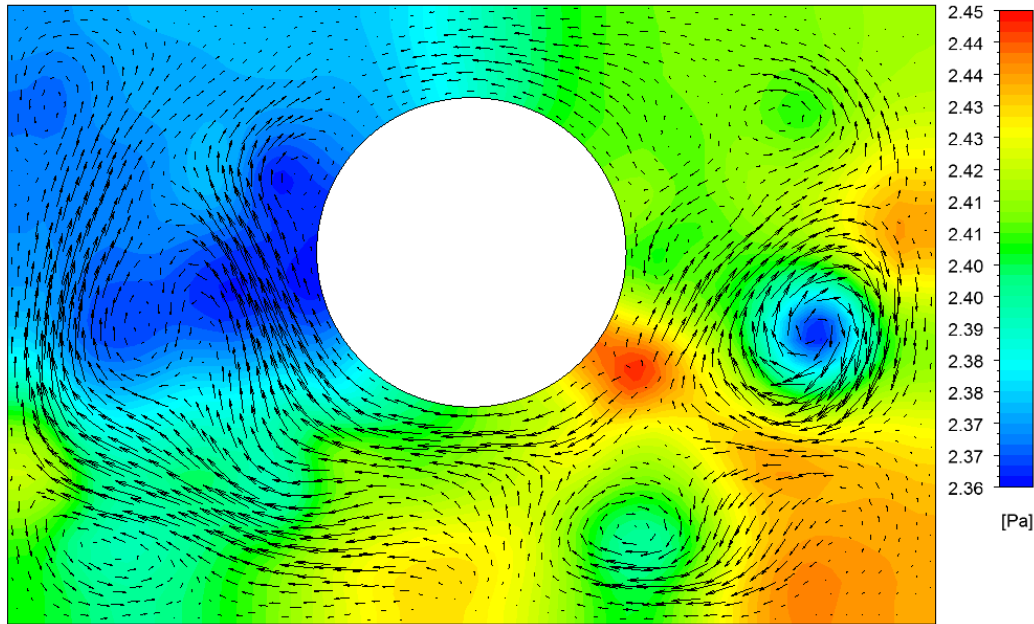


Figure 4.44: Vector plot of crossplane velocity (u and v) with shaded contours of pressure behind for $Re = 900$. Flow direction is into the page. Location and time are the same as in figure 4.42

Figures 4.42 to 4.44 show similar results to what was seen previously for $Re = 718$ (4.32 to 4.34), as the location of transition between pulsations does not have a single rotational direction. The subchannels are where the strongest flow can be found, with the middle of the right subchannel housing a very strong circulation zone. The left subchannel has a weaker flow circulation zone with quite strong crossplane flow either side of it. The bottom right part of the rod has a source of momentum on the crossplane, and there is a weaker momentum source in the bottom of the domain. The axial velocity is strongest in the bottom of the subchannels, with very weak flow in the gap itself.

The axial velocity gradient in figure 4.43 has a total difference of about 5 s^{-1} , with the strongest negative gradient over twice as large as the strongest positive gradient. On the whole, the domain experiences an overall positive gradient, around 0.50 s^{-1} . Near the bottom right of the

rod, there is an area with a strong negative gradient with the corresponding high pressure directing the flow away in the crossplane.

Overall change in pressure in figure 4.44 is 0.09 Pa. In the upper left quadrant, there is a large area of low pressure, whereas the high pressure is mainly in the lower right corner of the domain. Most of the domain is at the average pressure, about 2.40 Pa, which is light green. The momentum source on the crossplane corresponds to a region of high pressure, since the axial velocity is slowing down here. The area of low pressure in the right subchannel is at the centre of a circulation zone, and this zone has regions of high pressure around its edges.

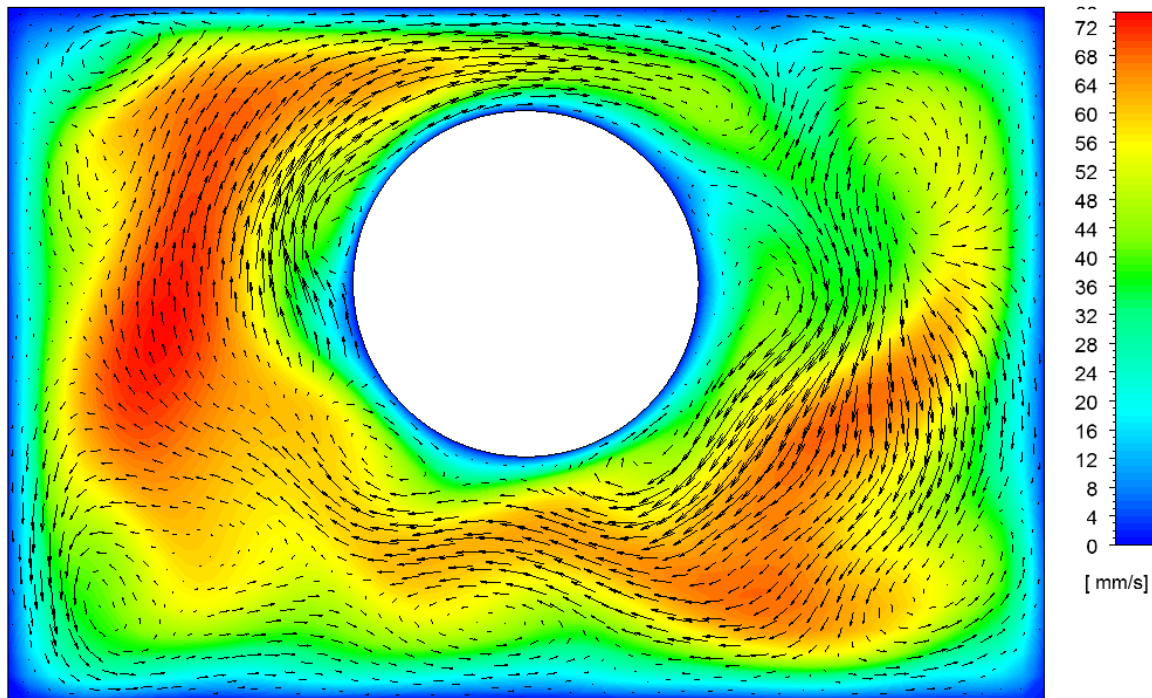


Figure 4.45: Vector plot of crossplane velocity (u and v) with shaded contours of axial velocity behind for $Re = 900$. Flow direction is into the page. Location is approximately 40 mm downstream from figure 4.42, taken after 75 seconds of true transient time has elapsed.

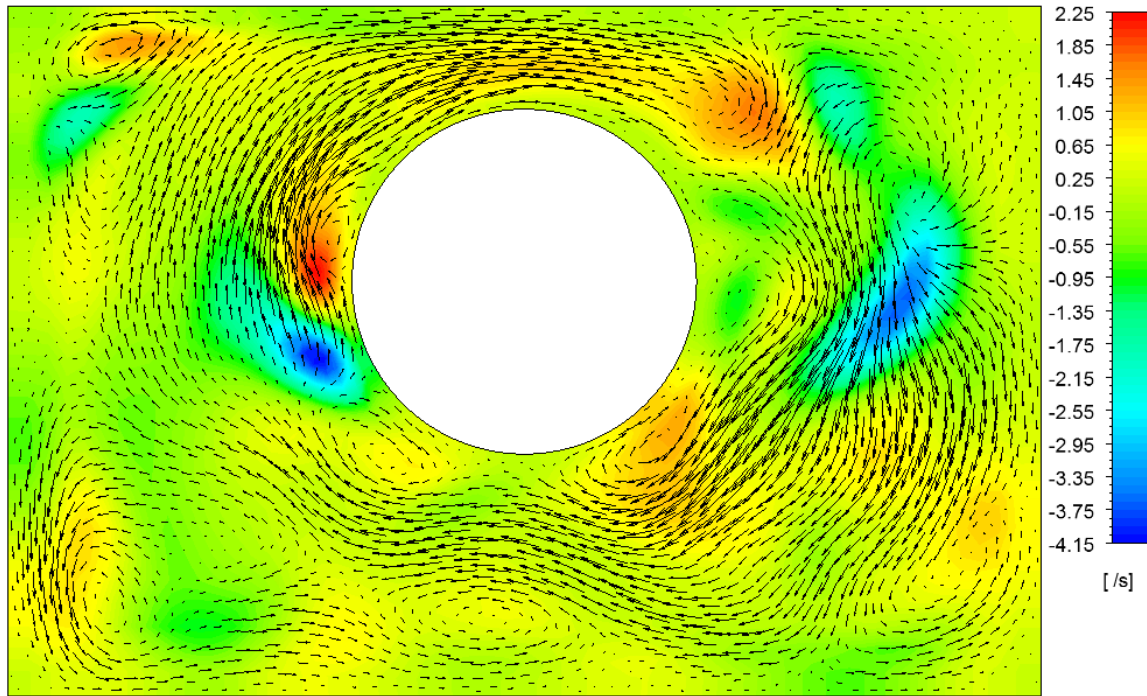


Figure 4.46: Vector plot of crossplane velocity (u and v) with shaded contours of axial velocity gradient behind for $Re = 900$. Flow direction is into the page. Location and time are the same as in figure 4.45.

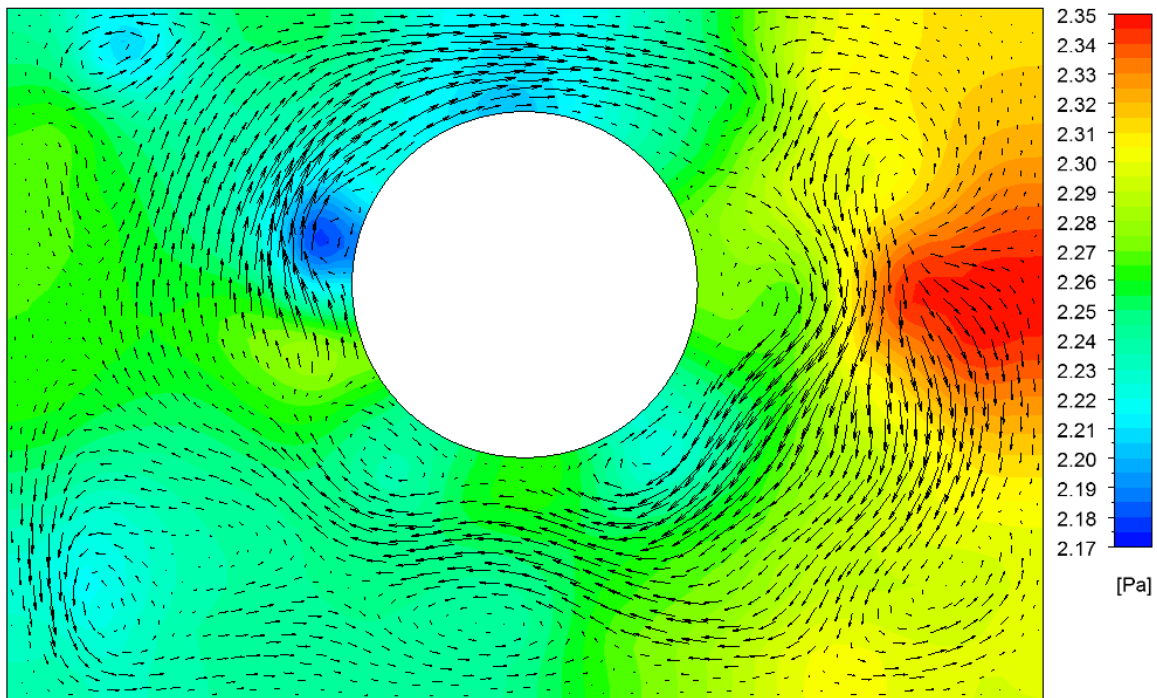


Figure 4.47: Vector plot of crossplane velocity (u and v) with shaded contours of pressure behind for $Re = 900$. Flow direction is into the page. Location and time are the same as in figure 4.45.

The flow in figures 4.45 to 4.47 rotates in an overall clockwise direction. The strongest flow is through the gap region and turning from the right subchannel into the secondary gap. Throughout the domain, there are quite a few circulation zones, found near the walls and the rod. Flow is only attached to the rod through the gap region. A crossplane momentum source can be seen near the bottom left of the rod, as well as on the right wall. The axial velocity is strongest in the upper part of the left subchannel, near the entrance to the gap. As has been seen previously, the weakest axial velocity is seen at the gap exit, coinciding with the slight circulation zone seen in the crossplane flow.

About two thirds of the distribution of the axial velocity gradient in figure 4.46 is negative, with a total different of about 6.40 s^{-1} . However, most of the domain has a fairly weak gradient, ranging between -0.55 and 0.65 s^{-1} . There are three areas of strong negative gradient; near the right wall, upper left wall and bottom left of the rod. All can be seen as acting as momentum sources in the crossplane. The areas of stronger positive gradient are acting to decrease the flow in the crossplane - the strongest is located middle left of the rod, one near the gap exit, another in the top left corner and one at the bottom right of the rod.

The pressure difference in figure 4.47 is 0.18 Pa , with most of the domain being near the average pressure of 2.26 Pa . The highest pressure is seen on the right side of the domain, near the wall. As has been observed in other crossplanes, the negative pressure regions tend to correspond to positive axial velocity gradients, as well as positive pressure being spatially linked to negative axial velocity gradients.

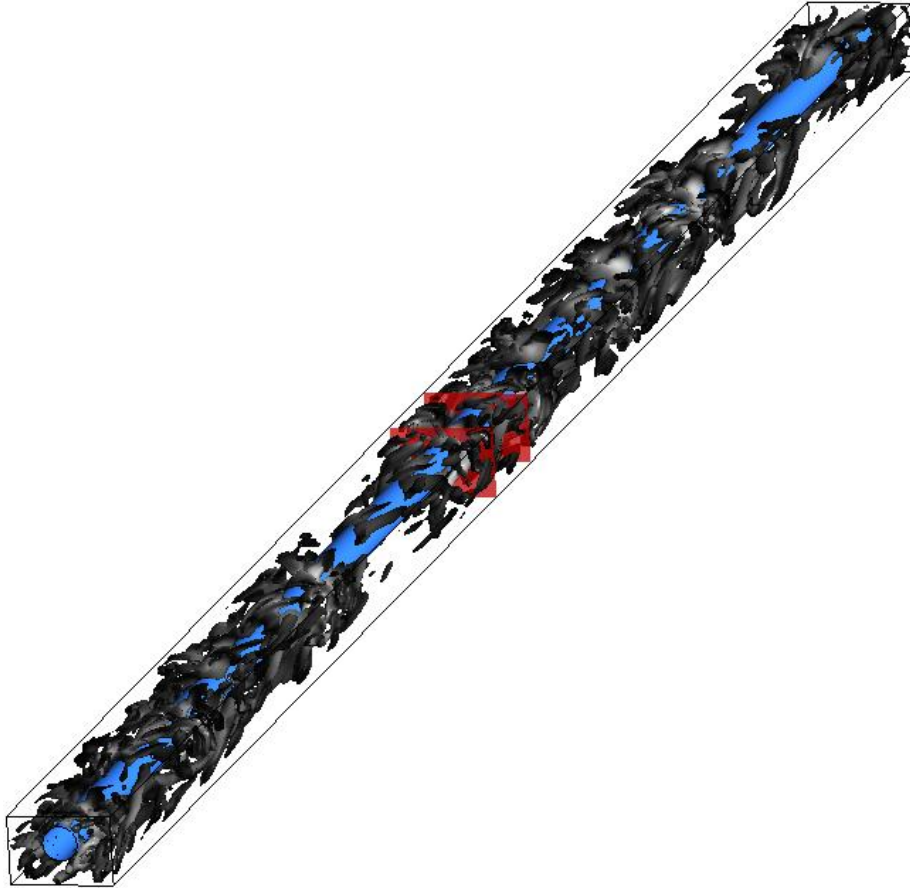


Figure 4.48: Isosurface plot of Q-criterion for $Re = 955$, 75 seconds into the true transient. $Q = 0.75 \text{ s}^{-2}$. Bulk flow is from bottom left to top right. The red planes show where the visualizations of figures 4.49 to 4.51 and 4.55 to 4.57 are taken. Figures 4.52 - 4.54 are taken in between the planes.

In the three-dimensional flow visualization shown above in figure 4.48, there are many more structures seen compared to figure 4.38. The structures still wrap around the rod, as in figure 4.28 and 4.38. Just before the visualization plans, and before the end of the domain, there are regions with a vastly reduced structure density. These regions correspond to areas in figure 4.2c which have regions where the total velocity is faster on one side, but does not have the same directionality into the gap. Also, from figure 4.3c, it can be seen that the spanwise velocity is much reduced in these regions. This behaviour is the same as was seen in figure 4.38, corresponding to figures 4.2b and 4.3b.

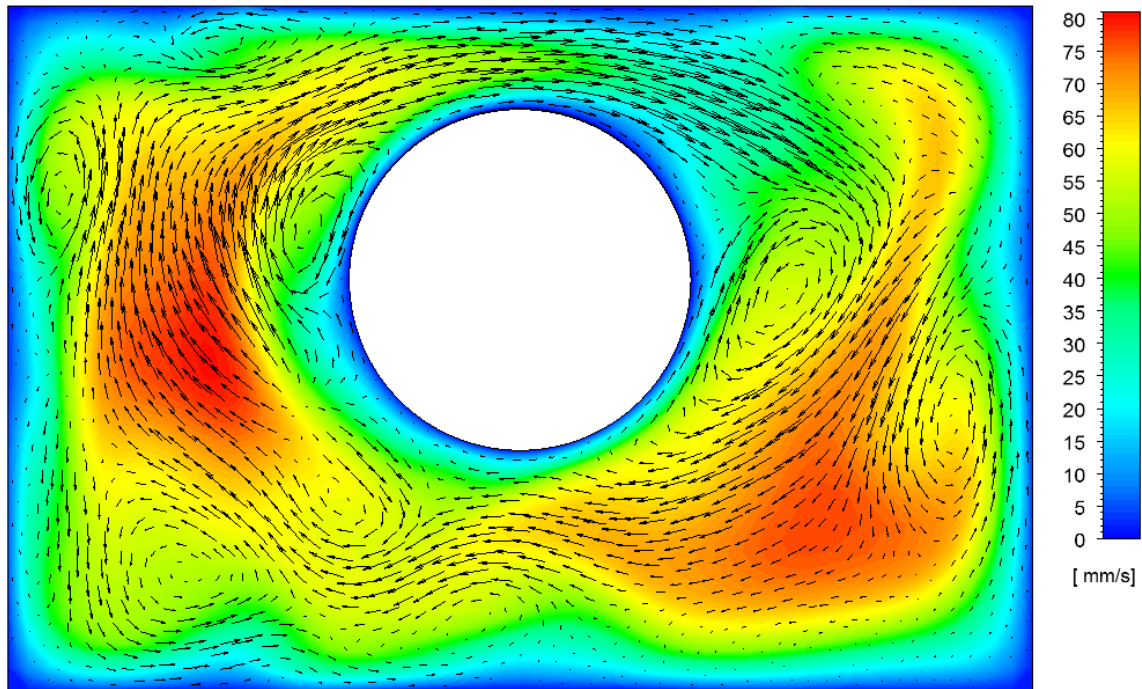


Figure 4.49: Vector plot of crossplane velocity (u and v) with shaded contours of axial velocity behind for $Re = 955$. Flow direction is into the page. Location is approximately 560 mm downstream from the inlet, taken after 75 seconds of true transient time has elapsed.

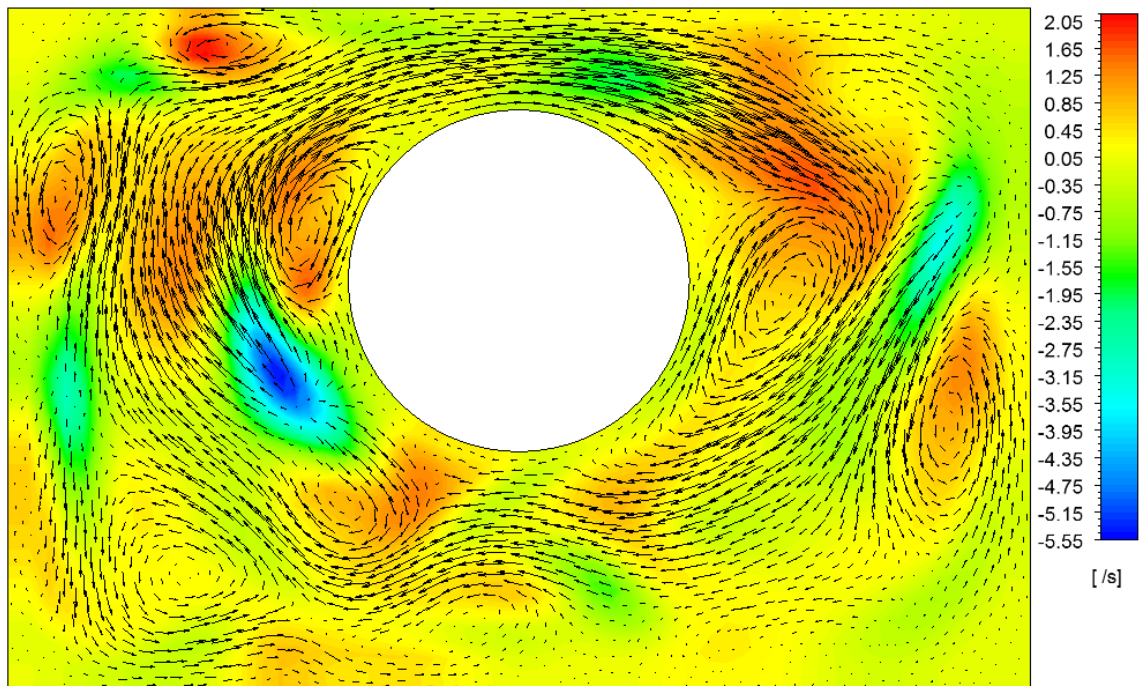


Figure 4.50: Vector plot of crossplane velocity (u and v) with shaded contours of axial velocity gradient behind for $Re = 955$. Flow direction is into the page. Location and time are the same as in figure 4.49.

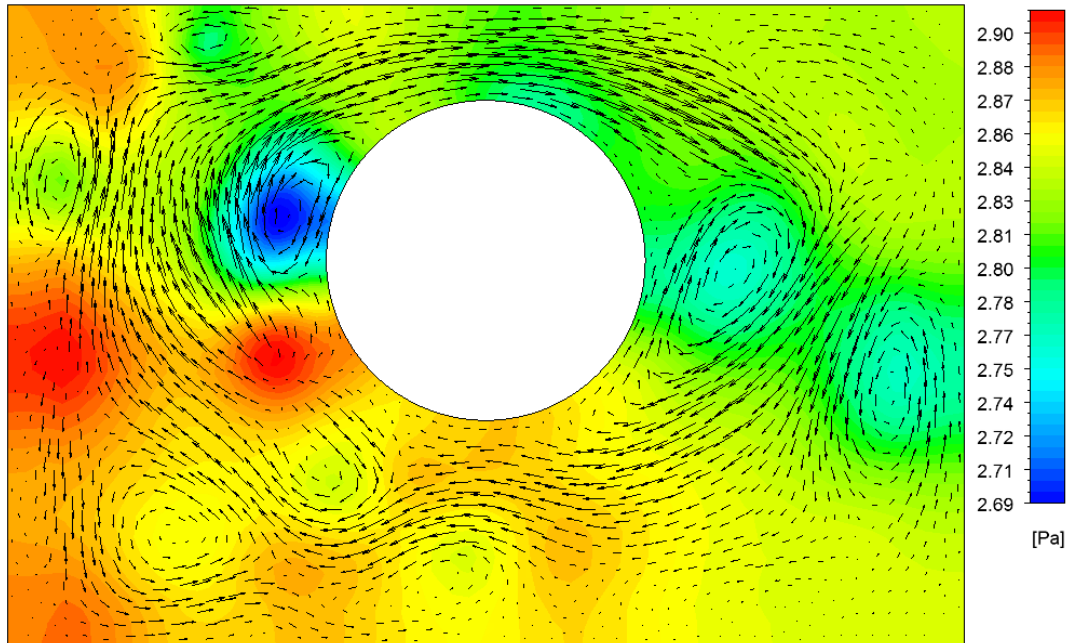


Figure 4.51: Vector plot of crossplane velocity (u and v) with shaded contours of pressure behind for $Re = 955$. Flow direction is into the page. Location and time are the same as in figure 4.49.

The flow in figures 4.49 to 4.51 rotates in a clockwise direction around the rod. This rotation follows the trend of pulsations being more than just flow through the gap, but involving the entire domain as well. There are circulation zones near the rod and walls which are stronger than those observed for flow rotating through the gap at lower Reynolds numbers. The strongest flow is seen exiting the gap and between two circulation zones in the left subchannel prior to entering the gap region. The axial velocity is strong in the regions where flow is entering the gap and around the bottom of the rod. The weakest axial velocity is seen in the gap exit region.

The difference in axial velocity gradient in figure 4.50 is 7.60 s^{-1} . The gradient scale is again heavily weighted towards negative values. Most of the domain has gradients ranging between -0.75 and 0.25 s^{-1} . The large negative gradients are where axial velocity is transferred to crossplane velocities. Most of the areas of positive axial velocity gradient are found near the

centres of circulation zones. There is also a large region of positive gradient as the flow exits the gap.

Total pressure change in figure 4.51 is 0.21 Pa. Higher pressure is mostly found in the bottom half of the domain, with one area of high pressure found in the top left corner. As would be expected, these areas are pushing flow away. The regions of lower pressure can be found in the centres of circulation zones. The high pressure regions correspond to negative axial velocity gradient, and act to influence the crossplane momentum.

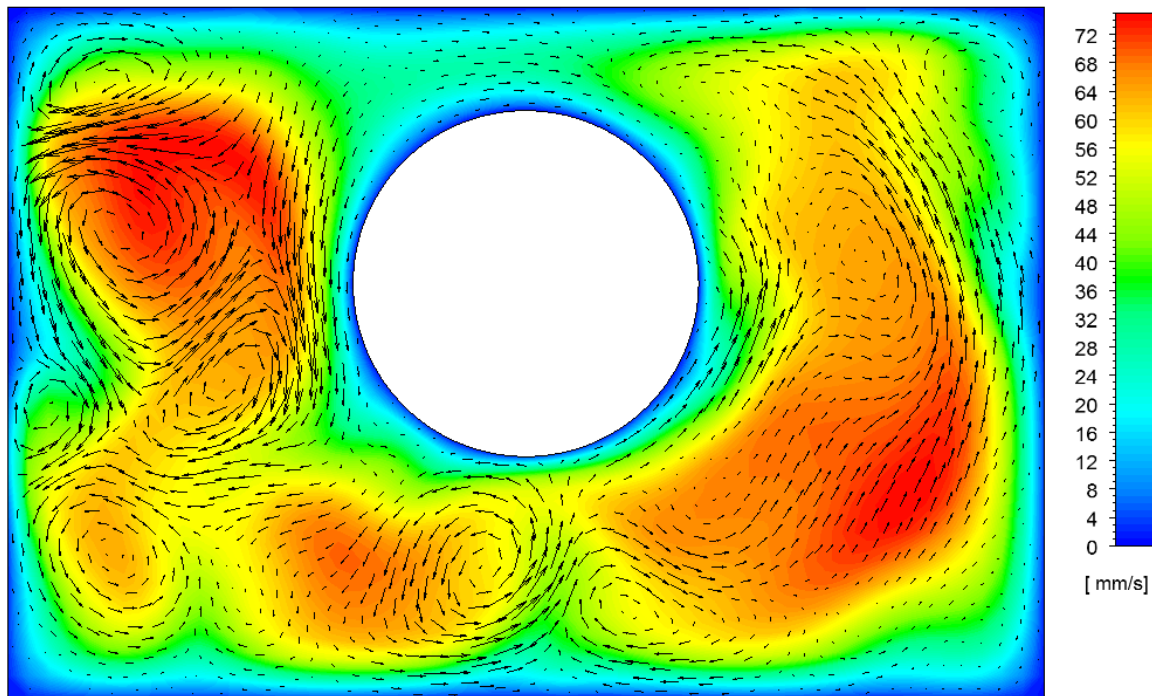


Figure 4.52: Vector plot of crossplane velocity (u and v) with shaded contours of axial velocity behind for $Re = 955$. Flow direction is into the page. Location is approximately 25 mm downstream from figure 4.49, taken after 75 seconds of true transient time has elapsed.

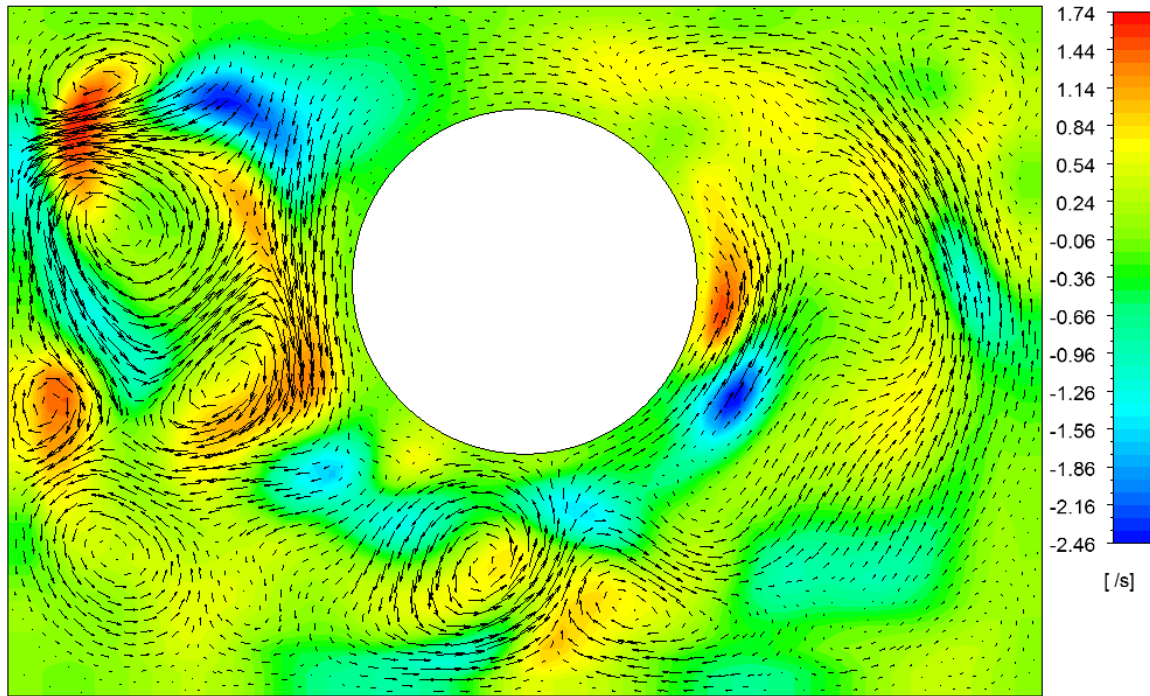


Figure 4.53: Vector plot of crossplane velocity (u and v) with shaded contours of axial velocity gradient behind for $Re = 955$. Flow direction is into the page. Location and time are the same as in figure 4.52.

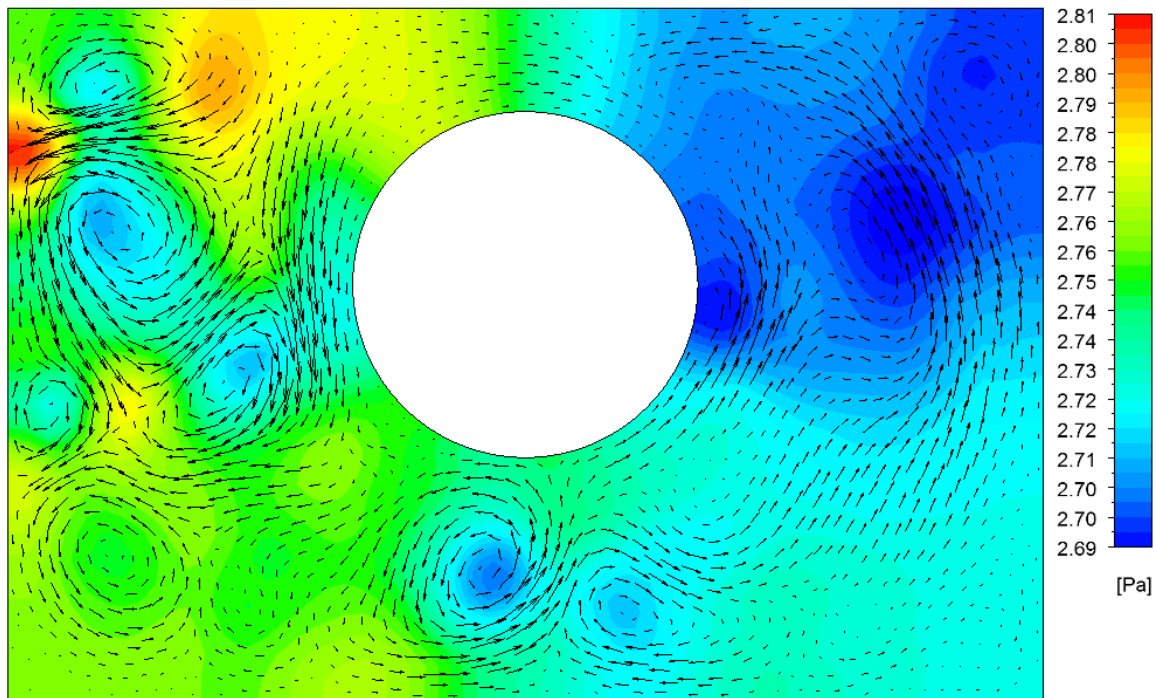


Figure 4.54: Vector plot of crossplane velocity (u and v) with shaded contours of pressure behind for $Re = 955$. Flow direction is into the page. Location and time are the same as in figure 4.52.

The state of transition flow in figures 4.52 to 4.54 is more complicated than has been seen previously. It has no rotational direction at all, with flow being strongest in a series of circulation zones in the left subchannel, near the wall. There is also a region of strong flow in the upper part of the right subchannel, where the flow shears off into some circulation zones. Throughout the domain, there are a number of pairs of counter-rotating circulation zones. The axial velocity is again weakest in the gap region. The strongest regions of axial velocity are in the upper left and the lower right subchannel.

The greatest negative axial velocity gradient in figure 4.53 is only about 0.70 s^{-1} greater in magnitude than the largest positive gradient, with a total change of about 4.2 s^{-1} . Despite these extrema, most of the domain is between -0.36 and 0.54 s^{-1} . A strong negative gradient in the upper left subchannel can be seen in conjunction with a momentum source on the crossplane. Another strong negative gradient is seen on the bottom right part of the rod, which again is a strong momentum source on the crossplane. One region of positive gradient exists near the left wall, as flow comes through the circulation zones and has to turn before the wall. There is another area of positive gradient on the right side of the rod, just above an area of negative gradient.

Total range of pressure seen in figure 4.54 is 0.12 Pa . The domain is roughly split down the middle, with the lower pressures mainly existing on the right side. The circulation zones have, for the most part, regions of lower pressure at their centres. A region of high pressure can be seen at the left wall, where the flow is being turned away from the wall as it exits the counter-rotating vortices.

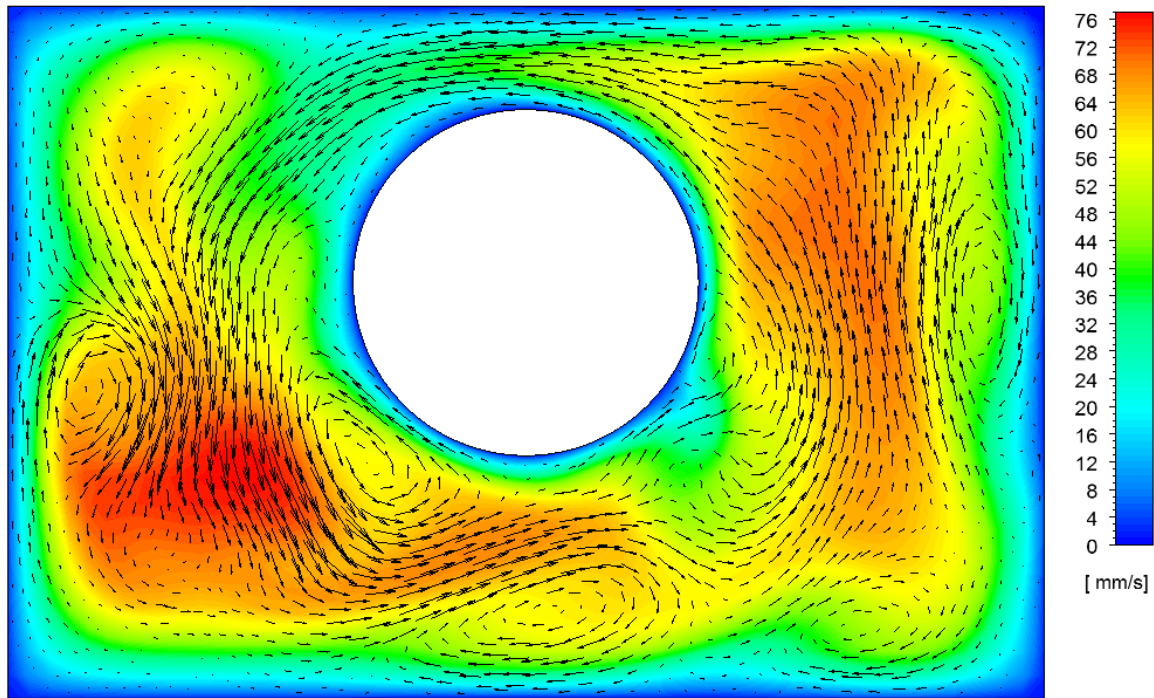


Figure 4.55: Vector plot of crossplane velocity (u and v) with shaded contours of axial velocity behind for $Re = 955$. Flow direction is into the page. Location is approximately 25 mm downstream from figure 4.52, taken after 75 seconds of true transient time has elapsed.

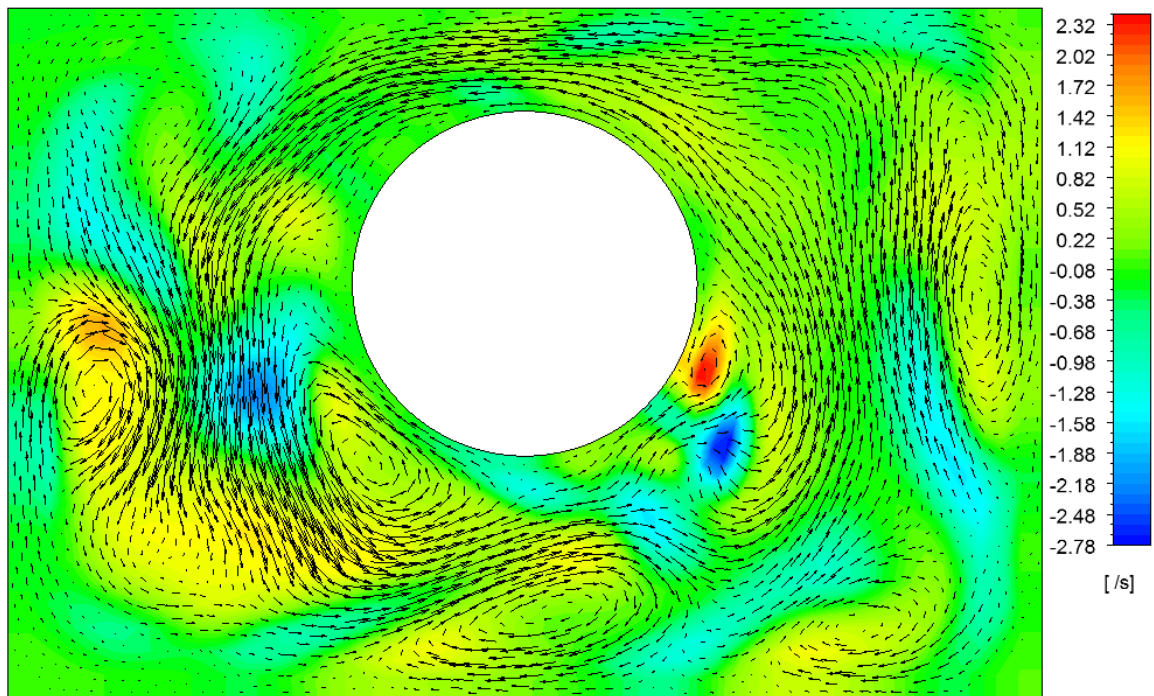


Figure 4.56: Vector plot of crossplane velocity (u and v) with shaded contours of axial velocity gradient behind for $Re = 955$. Flow direction is into the page. Location and time are the same as in figure 4.55.

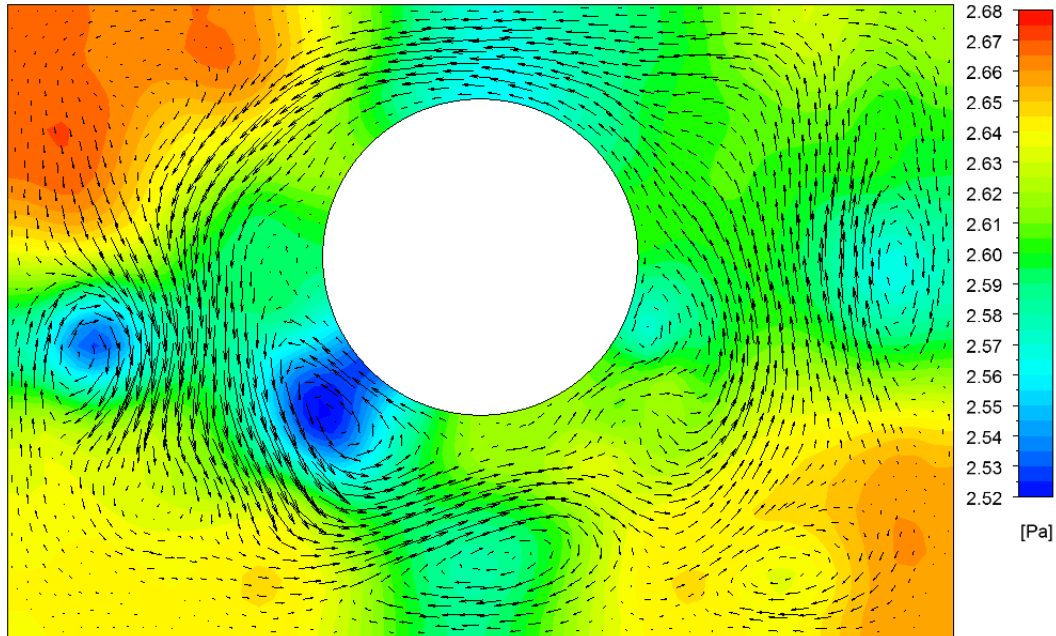


Figure 4.57: Vector plot of crossplane velocity (u and v) with shaded contours of pressure behind for $Re = 955$. Flow direction is into the page. Location and time are the same as in figure 4.55.

The direction of rotation of the flow in figures 4.55 to 4.57 is counter-clockwise. As seen before, there are a number of circulation zones which are near the rod and walls. The flow is strongest as it exits the gap, and increasing in velocity between a pair of counter-rotating circulation zones in the bottom of the left subchannel. The axial velocity is also strongest between these two counter-rotating circulation zones. Most of the right subchannel contains strong axial flow as well. As crossplane flow exits the gap, the axial velocity is correspondingly weak.

The distribution of the axial velocity gradient in figure 4.56 is much more uniform than has been seen previously, with a total spread of about 5.1 s^{-1} . Most of the domain has very little gradient; -0.3 to 0.3 s^{-1} . The regions of large negative velocity gradient correspond to places where the crossplane flow increases. One is seen as the flow passes between the counter-rotating vortices in the left subchannel, another is seen on the bottom right of the rod. The highest region of positive velocity gradient is seen at the centre of a small circulation zone next to the right side of the rod.

Total pressure difference in figure 4.57 is 0.16 Pa. All corners, apart from the upper right, have higher pressure regions. The domain mostly is at the average pressure, 2.60 Pa. Areas of low pressure can be found at the centre of circulation zones, as well as a weaker area in the gap region. Strongest pressure is seen in the top left corner of the domain, which helps to push the crossplane flow between the counter-rotating vortices.

The visualizations have shown that the flow on the crossplane is much more complicated than movement in and out of the gap region. When there is a strong pulse in a given direction, the flow rotates around the rod, carrying high momentum flow into the gap region from the subchannels. When the flow is exiting the gap, the axial velocity is correspondingly quite weak. In addition to the main rotating flow, there also exist many circulation zones throughout the domain. These increase in number and strength as the Reynolds number increases. For the most part, the domain has a relatively low axial velocity gradient, with small areas of extremes being found. The axial velocity gradient with its associated localized high or low pressure regions is a key part of momentum exchange from the axial flow to the flow on the crossplane. The gradient of axial velocity is also strongly correlated to the pressure field, with areas of low pressure where there is positive gradient, as well as high pressure where there is negative gradient.

4.7 Evolution of Pulsing Flow

One of the objectives of research into subchannel mixing is to understand the mechanism behind the pulsations. A step in understanding this mechanism is to investigate what happens as the flow develops from a purely axial duct flow. In order to investigate this, the case of $Re = 718$ was run with initial conditions of zero velocity everywhere. As has been discussed in section 3.3.3, this results in the same transient results as the initial conditions used for the simulations, but is much more computationally expensive. Some of the key parameters which are strongly

correlated with the pulsating rotational flow have been discussed in the previous section. These parameters - axial velocity gradient, pressure and axial velocity will be plotted on crossplane visualizations to compare the evolving flow to the fully evolved flow.

The transient run with purely axial flow is shown below in figure 4.58. The flow shown is straight, without any visible disturbances which would be associated with spanwise velocities significant enough to affect the main axial flow.

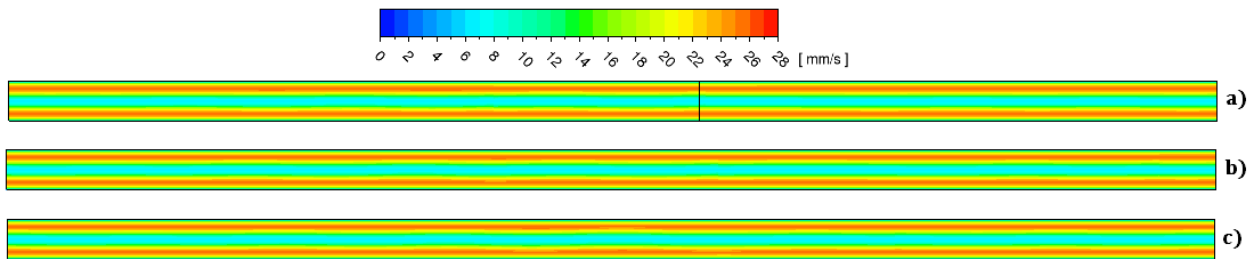


Figure 4.58: Total velocity contours for $Re = 718$, after starting the transient from an initial guess of zero velocity everywhere. Flow is from left to right. Taken on the visualization plane shown in figure 4.1 a) 60.5 seconds after starting, black line indicating the location of the crossplane in figure 4.59. b) 62.5 seconds after starting c) 63.5 seconds after starting.

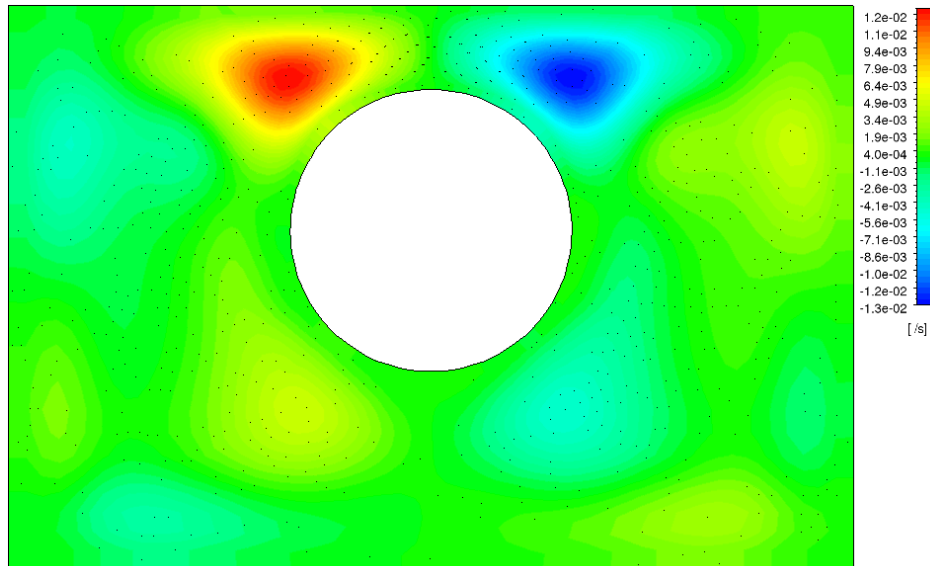


Figure 4.59: Axial velocity gradient contour with crossplane velocity vectors in front. $Re = 718$. Axial flow is into the page. Taken 60.5 seconds after starting the transient from zero velocity. This image is typical of the flow in 4.58a, but was taken from a location 670 mm downstream of the inlet, indicated by a black line on figure 4.58a.

The axial velocity gradient in figure 4.59 is extremely small, about two orders of magnitude lower than what is seen in the fully evolved pulsating flow. It appears to be symmetrical around a vertical plane running through the middle of the domain. The extrema are located across the gap, which would start to drive some flow through the gap region. Their location is close to the location of inflection points in the axial velocity profile in the spanwise direction. The very small crossplane flows seen in this case are roughly two orders of magnitude lower than the observed flow in fully developed pulsations. Consequently, the flow in the duct remains essentially axial flow. For figure 4.59 and all following figures, the crossplane velocity vectors are the same scale as those seen in the fully evolved flow (eg: figure 4.30).

Figure 4.60 below shows three snapshots, taken five seconds after the ones in figure 4.58a,b,c respectively. In those intervening five seconds, the flow has begun to show asymmetry, with alternating areas of higher velocity appearing in the subchannel regions. This asymmetry will mean there is an imbalance in the relative magnitude of the axial velocity gradient in the spanwise direction. This imbalance will start to turn flow into the gap region.

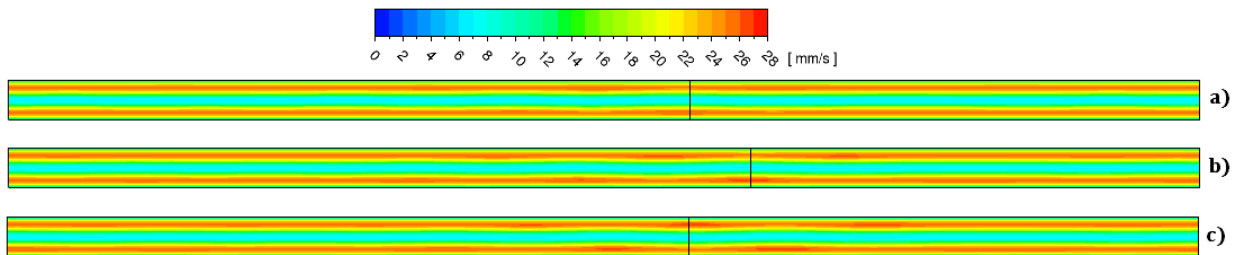


Figure 4.60: Total velocity contours for $Re = 718$, after starting the transient from an initial guess of zero velocity everywhere. Flow is from left to right. Taken on the visualization plane shown in figure 4.1. Black lines indicate planes where visualizations were taken. a) 65.5 seconds after starting. b) 67.5 seconds after starting c) 68.5 seconds after starting

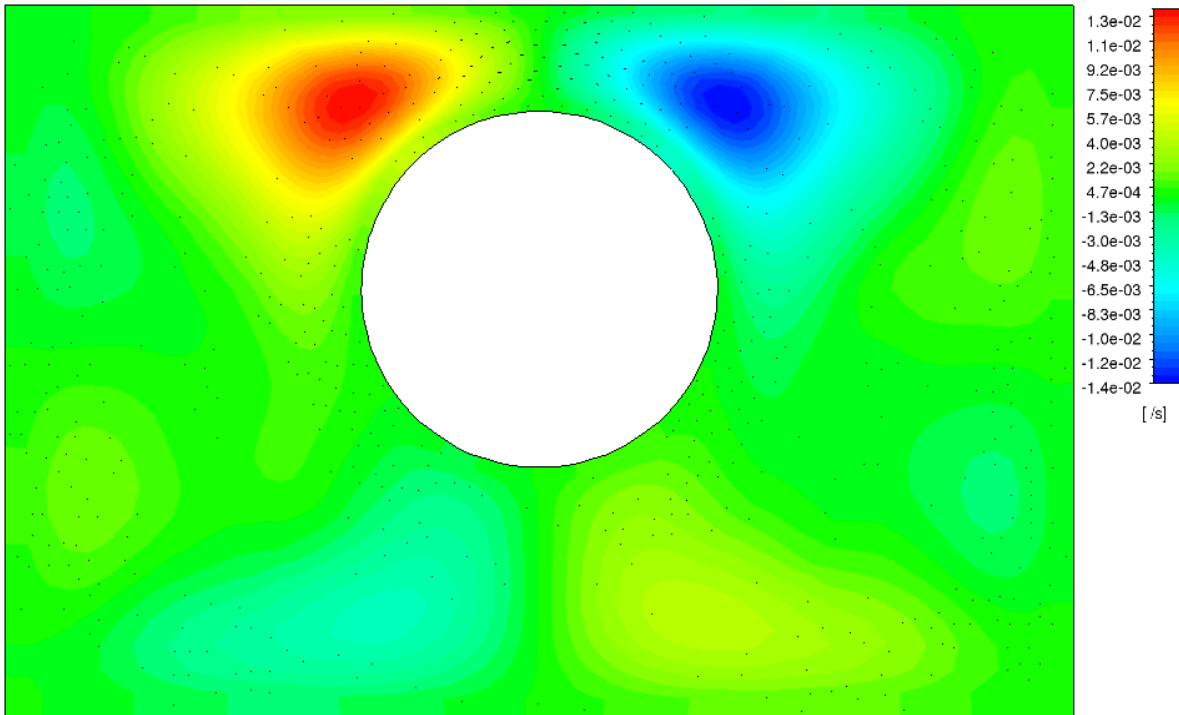


Figure 4.61: Axial velocity gradient contour with crossplane velocity vectors in front. $Re = 718$. Axial flow is into the page. Taken 65.5 seconds after starting the transient from zero velocity. Location is approximately 670 mm downstream of inlet.

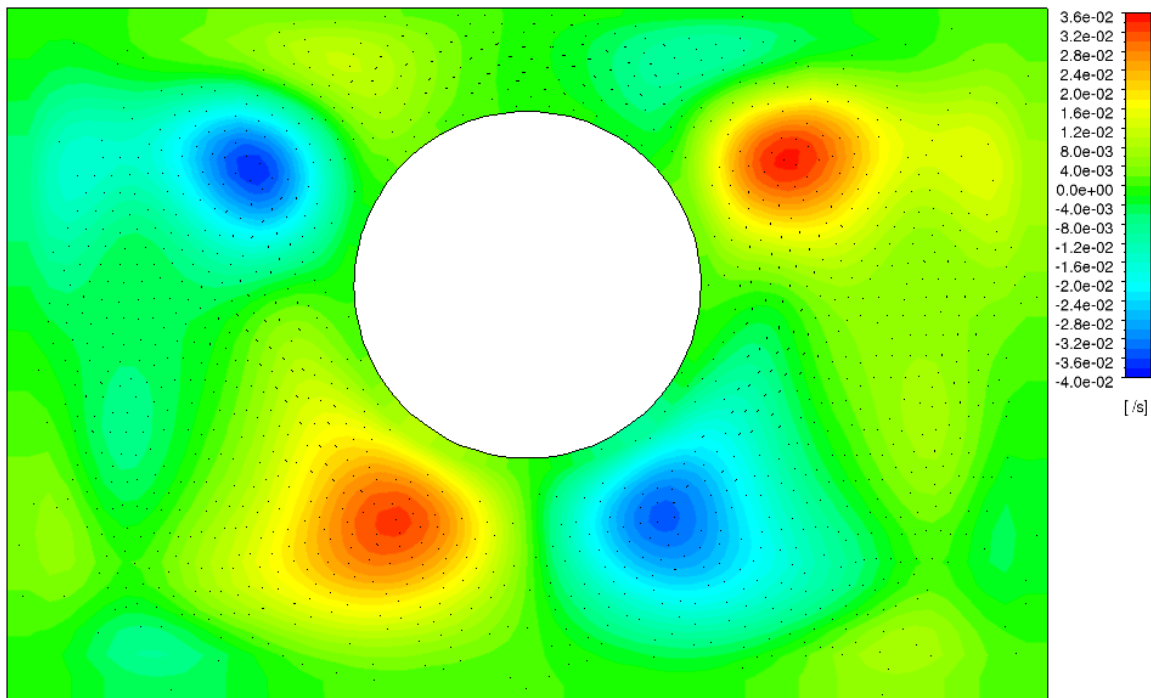


Figure 4.62: Axial velocity gradient contour with crossplane velocity vectors in front. $Re = 718$. Axial flow is into the page. Taken 67.5 seconds after starting the transient from zero velocity. Location is approximately 730 mm downstream of inlet.

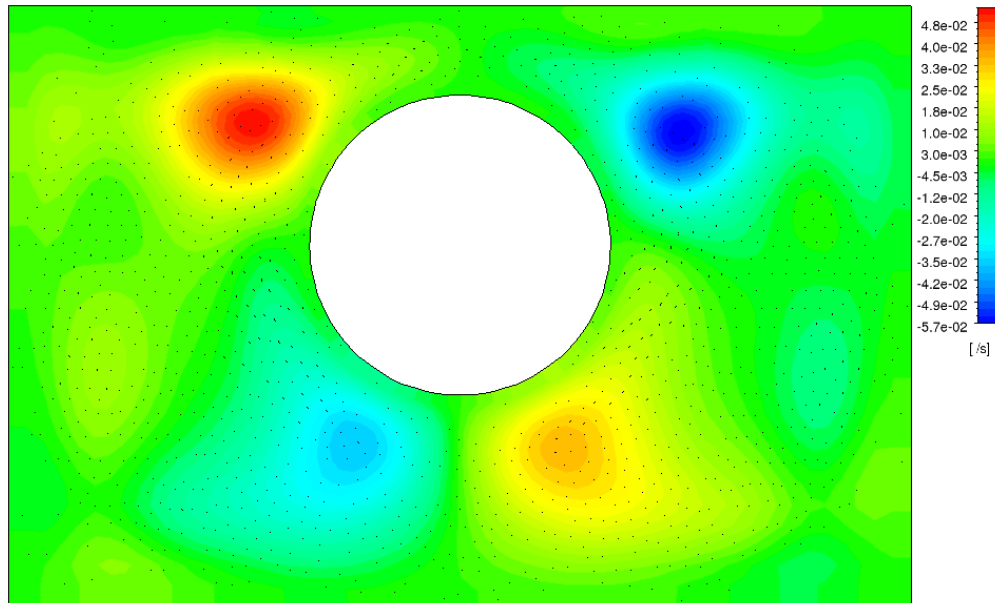


Figure 4.63: Axial velocity gradient contour with crossplane velocity vectors in front. $Re = 718$. Axial flow is into the page. Taken 68.5 seconds after starting the transient from zero velocity. Location is approximately 670 mm downstream of inlet.

Figures 4.61 to 4.63 show a variation in the crossflow rotation direction. Figure 4.61 shows flow transitioning between rotation directions. Figure 4.62 is both two seconds later and 60 mm downstream of the crossplane in figure 4.61, effectively moving a quarter of a full period (about 120 mm) downstream. Figure 4.63 (one second later but 60 mm upstream of figure 4.62) is approximately half a period upstream of figure 4.62. Essentially, figure 4.62 and 4.63 show opposite pulsation directions. In figures 4.62 and 4.63, the gradient change is about forty times smaller than fully pulsing flow. Looking at figures 4.60b and 4.60c, the region of stronger flow in the visualization plane changes side and in figures 4.62 and 4.63, the region of negative gradient switches sides accordingly. The crossplane velocities in figure 4.63 have a maximum of 0.4 mm/s, also approximately forty times smaller than the maximum seen in fully pulsing flow. Progressing in time from figure 4.61 to 4.63, the regions of axial velocity gradient have moved out from the gap edges, and there are regions which develop in the secondary gap which are anti-phase to those seen in the smaller gap.

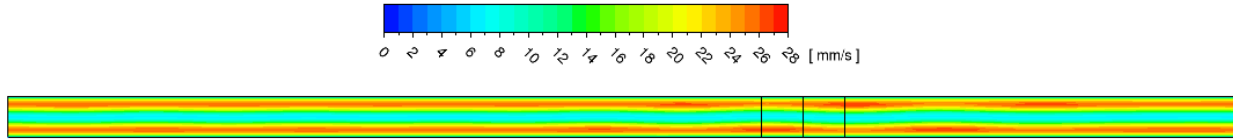


Figure 4.64: Total velocity contours for $Re = 718$, after starting the transient from an initial guess of zero velocity everywhere. Flow is from left to right. Time elapsed is 72.5 seconds Taken on the visualization plane shown in figure 4.1. The black lines indicate planes where figures 4.65 to 4.67 were taken, and are 720 mm, 760 mm and 800 mm from the inlet.

The total velocity contour shown in figure 4.64, four seconds on from 4.60c, despite the regions of higher flow, is still quite straight overall. These higher flow regions have increased in width and length slightly from figure 4.60c. The growing imbalance between the flow on either side of the rod is starting to affect the direction of the flow. The characteristic movement seen in figure 4.2 is just starting to grow and develop here. Figures 4.65 to 4.67 show the crossflow planes spatial spanning roughly half of a period, all at a single time of 72.5 seconds.

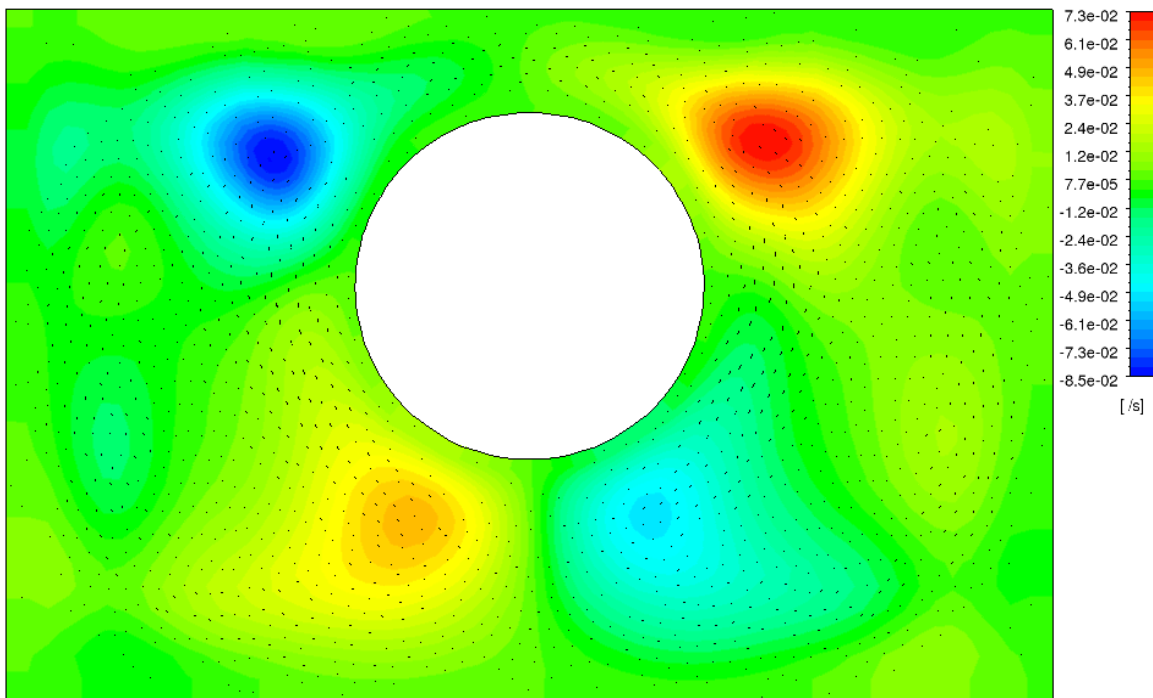


Figure 4.65: Axial velocity gradient contour with crossplane velocity vectors in front. $Re = 718$. Axial flow is into the page. Taken 72.5 seconds after starting the transient from zero velocity. Location is approximately 720 mm downstream of inlet.

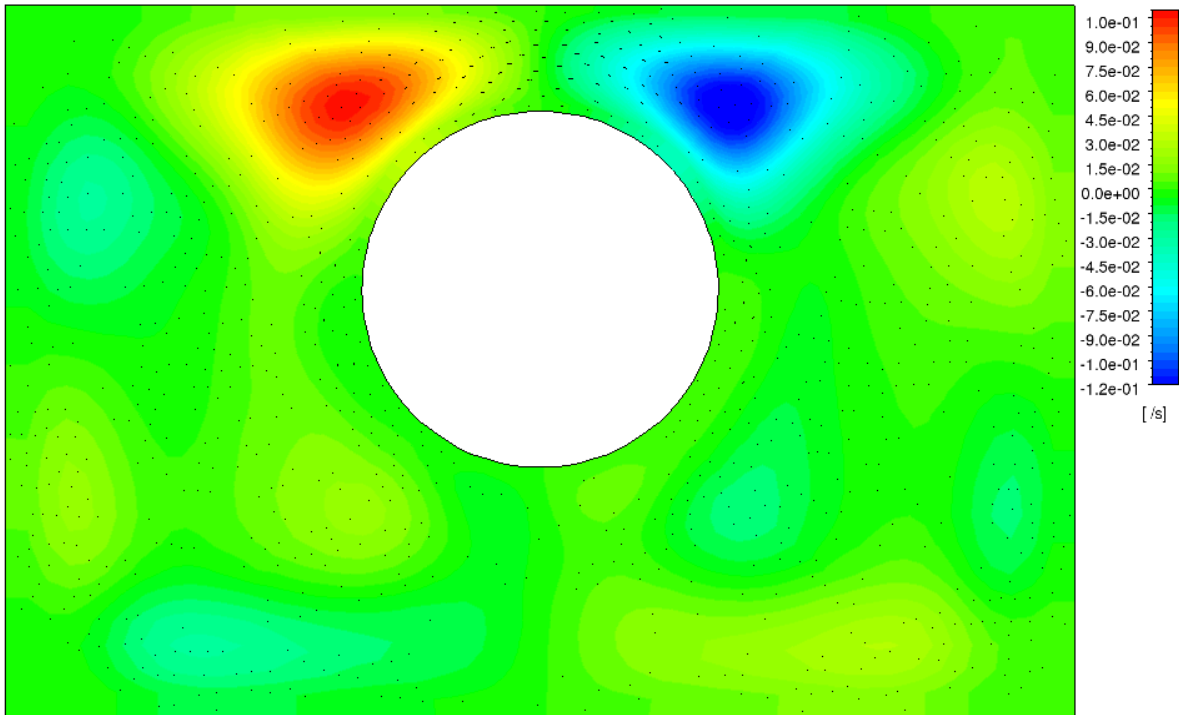


Figure 4.66: Axial velocity gradient contour with crossplane velocity vectors in front. $Re = 718$. Axial flow is into the page. Taken 72.5 seconds after starting the transient from zero velocity. Location is 40 mm downstream of the location in figure 4.65.

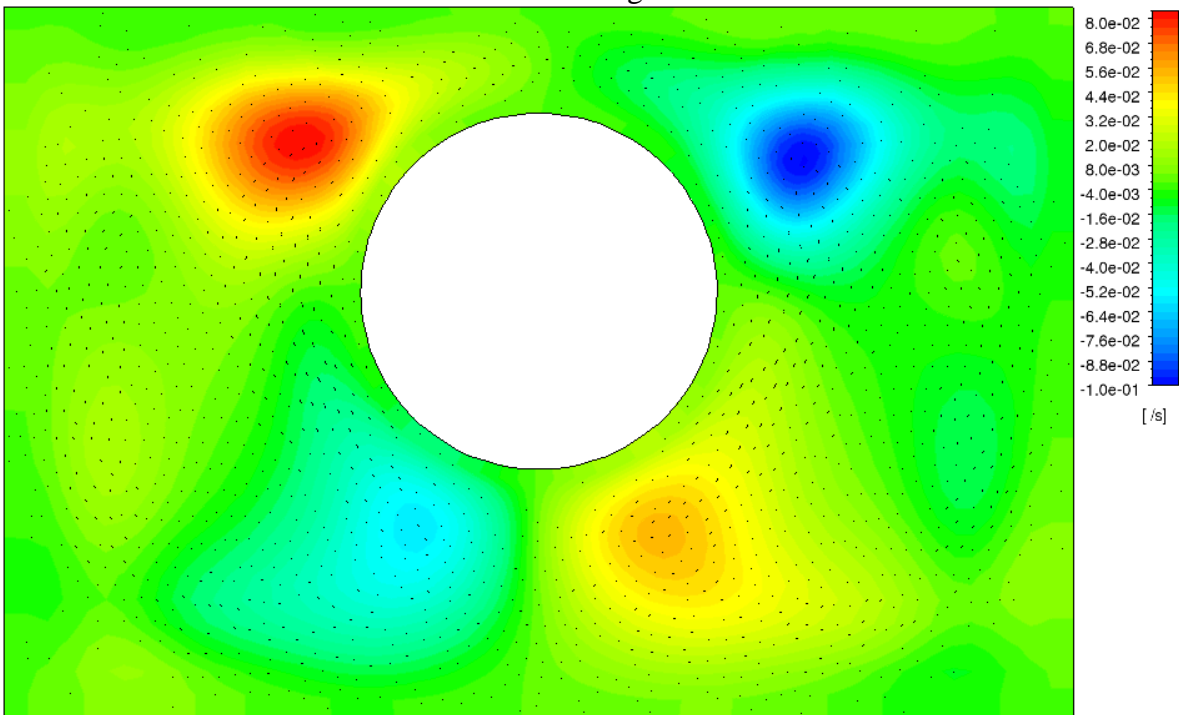


Figure 4.67: Axial velocity gradient contour with crossplane velocity vectors in front. $Re = 718$. Axial flow is into the page. Taken 72.5 seconds after starting the transient from zero velocity. Location is 40 mm downstream of the location in figure 4.66.

The highest change in velocity gradient, 0.2 s^{-1} , is seen in figure 4.66, which is where the flow appears to have roughly equal total velocity, but is transitioning between pulsation directions. This value is approximately fifteen times smaller than the change seen in an equivalent plane in fully evolved pulsing flow. Symmetry which was present in the domain has continued to decrease as time progresses. Figures 4.65 and 4.67 show similar locations of gradient extrema compared to figure 4.66. This is because 4.66 is transitioning between pulsation directions, whereas 4.65 and 4.67 are in the middle of a pulsation. The maximum of the crossplane flow is about 0.55 mm/s , which is approximately twenty times smaller than the maximum seen in the fully evolved case.

Figures 4.65 and 4.67 show a further movement away from the gap edges of the locations of extreme axial velocity gradient. The flow in these two figures is correlated with an axial velocity imbalance across the gap, seen in figure 4.64. They display the same developing regions of axial velocity gradient in the secondary gap that were seen in figures 4.62 and 4.63, although the regions in figures 4.65 and 4.67 are lower in relative magnitude. Figure 4.66 shows regions which are much closer to the gap edges, and larger than those seen in figures 4.65 and 4.67. Unlike figures 4.65 and 4.67, figure 4.66 does not display the same regions of extreme axial velocity gradient in the secondary gap.

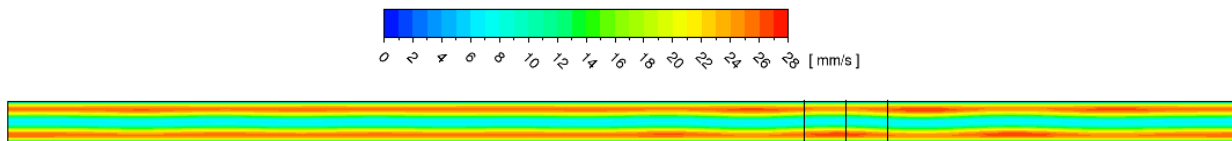


Figure 4.68: Total velocity contours for $Re = 718$, after starting the transient from an initial guess of zero velocity everywhere. Flow is from left to right. Time elapsed is 74.5 seconds Taken on the visualization plane shown in figure 4.1. The black lines indicate planes where visualizations were taken, and are 760 mm, 800 mm and 840 mm from the inlet.

The effect of the regions of higher velocity is becoming more pronounced on the slower flow in the gap. The gap flow is continuing to be pushed away from these higher velocity regions, more strongly than seen in figure 4.64. These regions of higher velocity are continuing to increase in size. The relative difference between the high and low velocities at the edges of the gap are also increasing from figure 4.64.

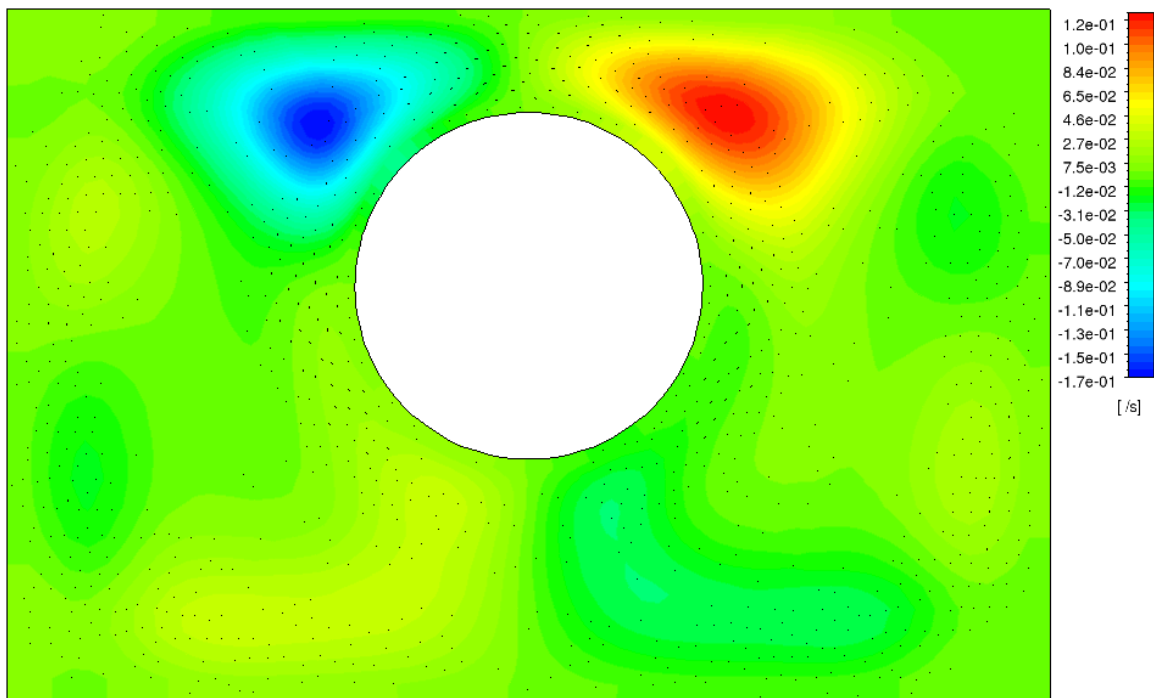


Figure 4.69: Axial velocity gradient contour with crossplane velocity vectors in front. $Re = 718$. Axial flow is into the page. Taken 74.5 seconds after starting the transient from zero velocity. Location is approximately 760 mm downstream of inlet.

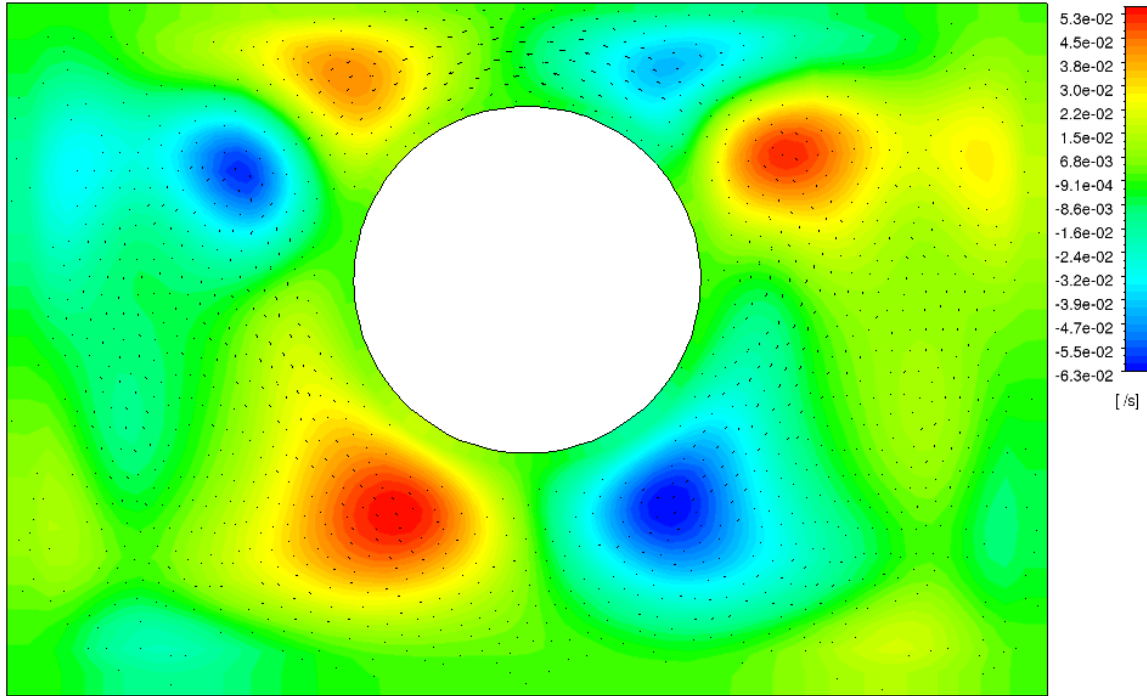


Figure 4.70: Axial velocity gradient contour with crossplane velocity vectors in front. $Re = 718$. Axial flow is into the page. Taken 74.5 seconds after starting the transient from zero velocity. Location is 40 mm downstream of the location in figure 4.69.

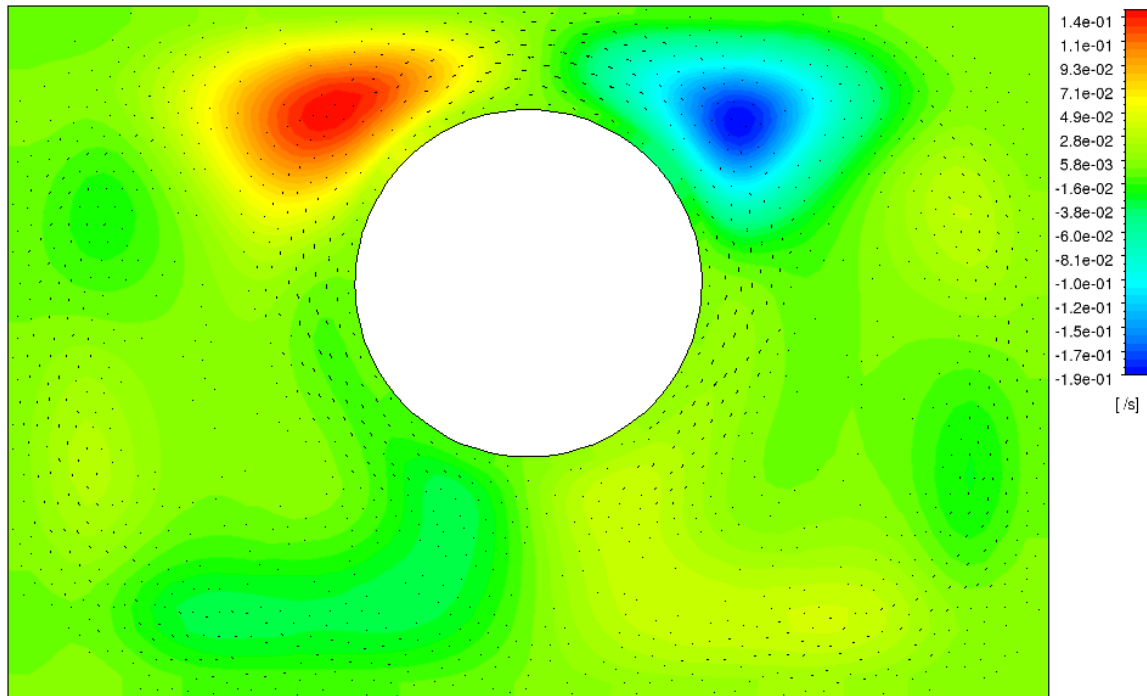


Figure 4.71: Axial velocity gradient contour with crossplane velocity vectors in front. $Re = 718$. Axial flow is into the page. Taken 74.5 seconds after starting the transient from zero velocity. Location is 40 mm downstream of the location in figure 4.72.

Figures 4.69 and 4.71 show a total difference in velocity gradient of about 0.3 s^{-1} , which is one order of magnitude below the differences seen in fully evolved flow. Figure 4.70, which is in the middle of an evolving pulsation, has more regions of extreme velocity gradient than were seen in figures 4.65 and 4.67. The extra regions in figure 4.70 appear to have split from the regions near the edges of the main gap. These weaker regions are in a similar position to the extrema seen in figure 4.59, although they are about three times greater in magnitude. These six regions of extreme velocity gradient in figure 4.70 are acting to rotate the flow around the rod, due to momentum exchange occurring between paired regions of negative and positive axial velocity gradient. The strongest crossplane flow is about 0.96 mm/s , about an order of magnitude below what is observed in evolved flow.

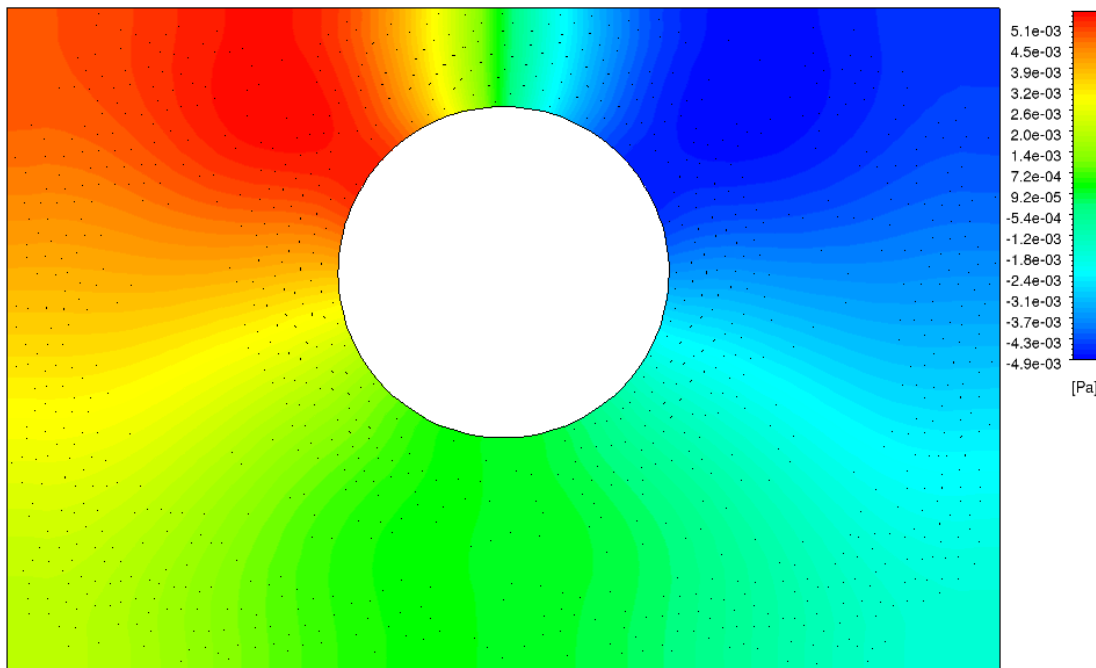


Figure 4.72: Contour of pressure fluctuations with crossplane velocity vectors in front. $Re = 718$. Axial flow is into the page. Taken 74.5 seconds after starting the transient from zero velocity. Location is 760 mm downstream of the inlet.

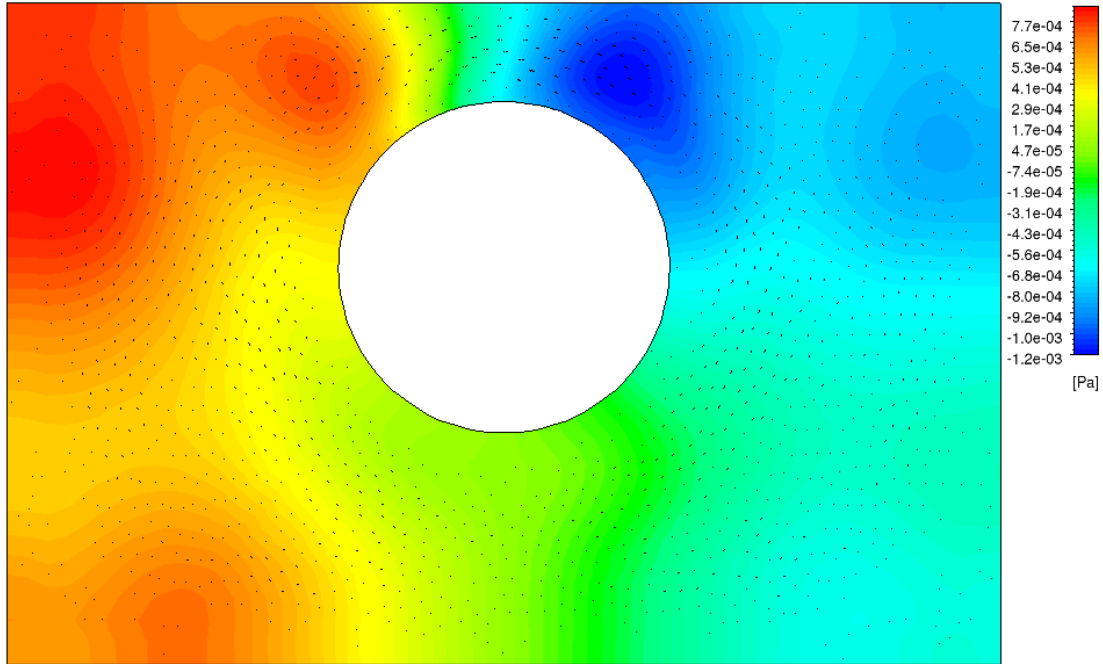


Figure 4.73: Contour of pressure fluctuations with crossplane velocity vectors in front. $Re = 718$. Axial flow is into the page. Taken 74.5 seconds after starting the transient from zero velocity. Location is 40 mm downstream of the location in figure 4.74.

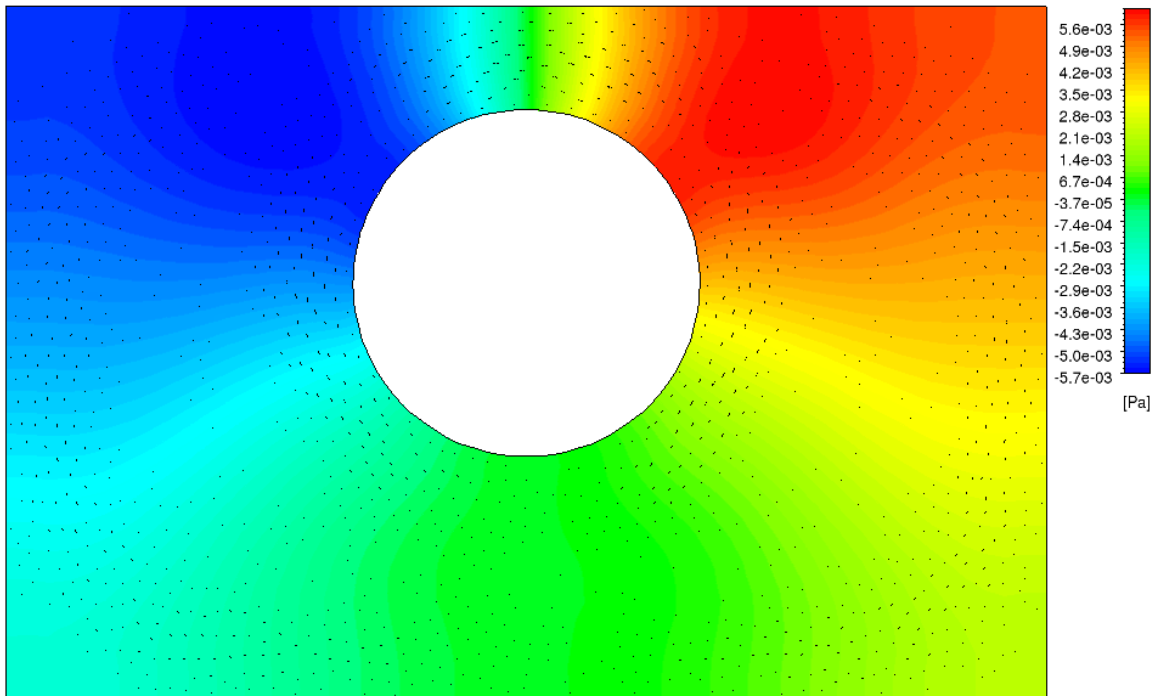


Figure 4.74: Contour of pressure fluctuations with crossplane velocity vectors in front. $Re = 718$. Axial flow is into the page. Taken 74.5 seconds after starting the transient from zero velocity. Location is 40 mm downstream of the location in figure 4.75.

Figures 4.72 and 4.74 show extremes of pressure fluctuations in the upper parts of the right and left subchannels. Below the rod, the pressure fluctuations are essentially zero. Between these regions, there is a fairly steady transition. The change in pressure within the domain is about 0.01 Pa, ten times smaller than what is seen in fully evolved flow. Figure 4.73 is almost split down the middle between high and low pressure. The pressure extremes are not as symmetrical as in 4.72 and 4.74. Low pressure is on the side with the higher velocity, seen in figure 4.69.

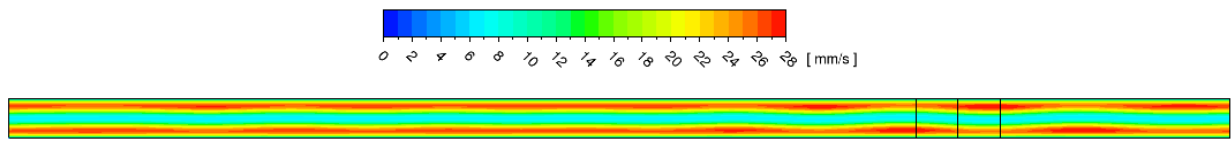


Figure 4.75: Total velocity contours for $Re = 718$, after starting the transient from an initial guess of zero velocity everywhere. Flow is from left to right. Time elapsed is 76.5 seconds Taken on the visualization plane shown in figure 4.1. Flow is from left to right. The black lines indicate planes where visualizations were taken, and are 870 mm, 910 mm and 950 mm from the inlet.

In figure 4.75, the regions of higher velocity in the subchannels have become much more pronounced. The lower velocity flow in the gap can be seen to move up and down, away from the regions of higher velocity. This matches up with what would be expected when there is a velocity imbalance on either side of an infinitesimal volume of fluid. The higher velocity on the outside will turn the fluid into the gap.

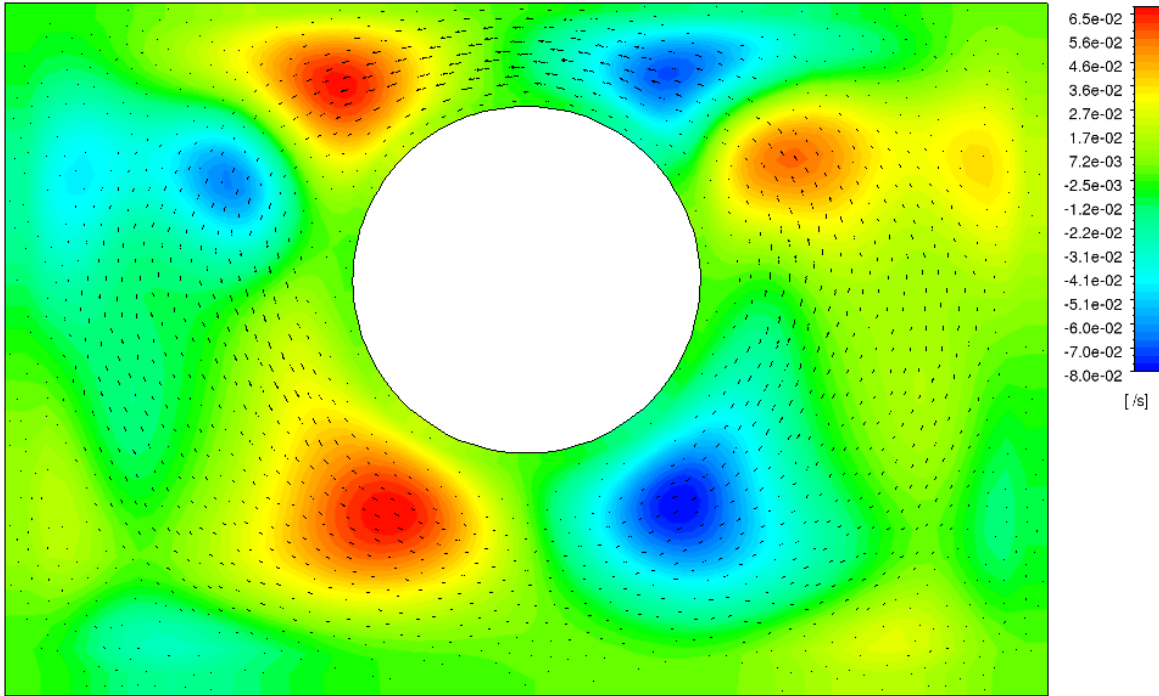


Figure 4.76: Axial velocity gradient contour with crossplane velocity vectors in front. $Re = 718$. Axial flow is into the page. Taken 76.5 seconds after starting the transient from zero velocity. Location is approximately 870 mm downstream of inlet.

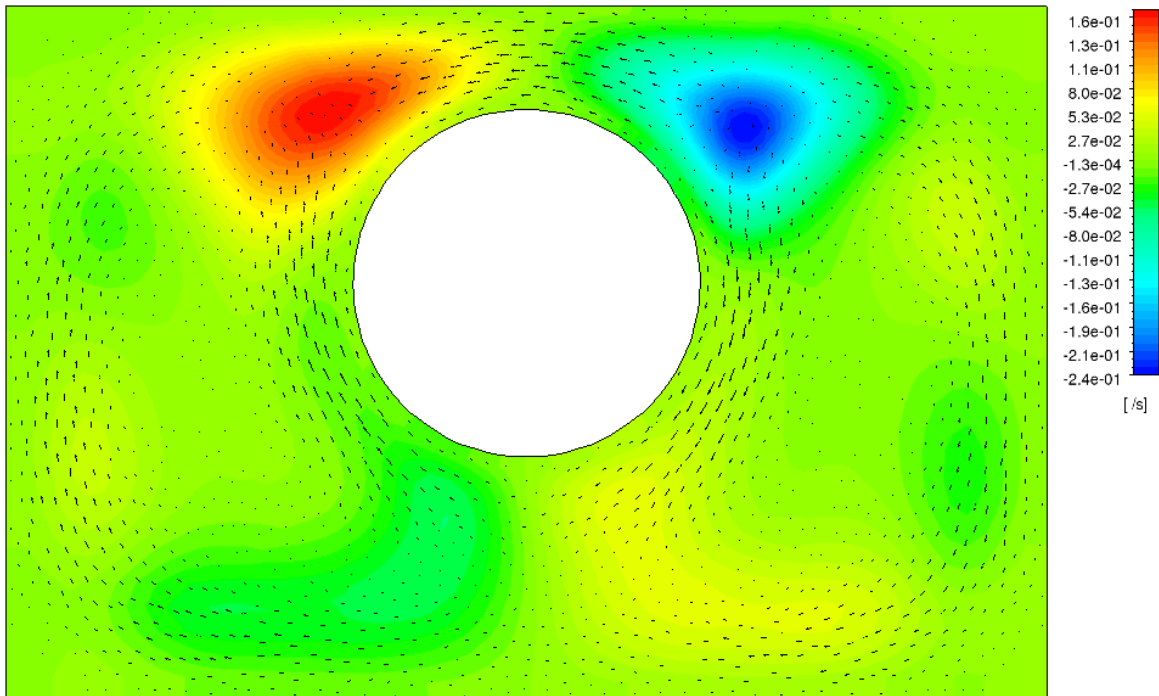


Figure 4.77: Axial velocity gradient contour with crossplane velocity vectors in front. $Re = 718$. Axial flow is into the page. Taken 76.5 seconds after starting the transient from zero velocity. Location is approximately 40 mm downstream from figure 4.76.

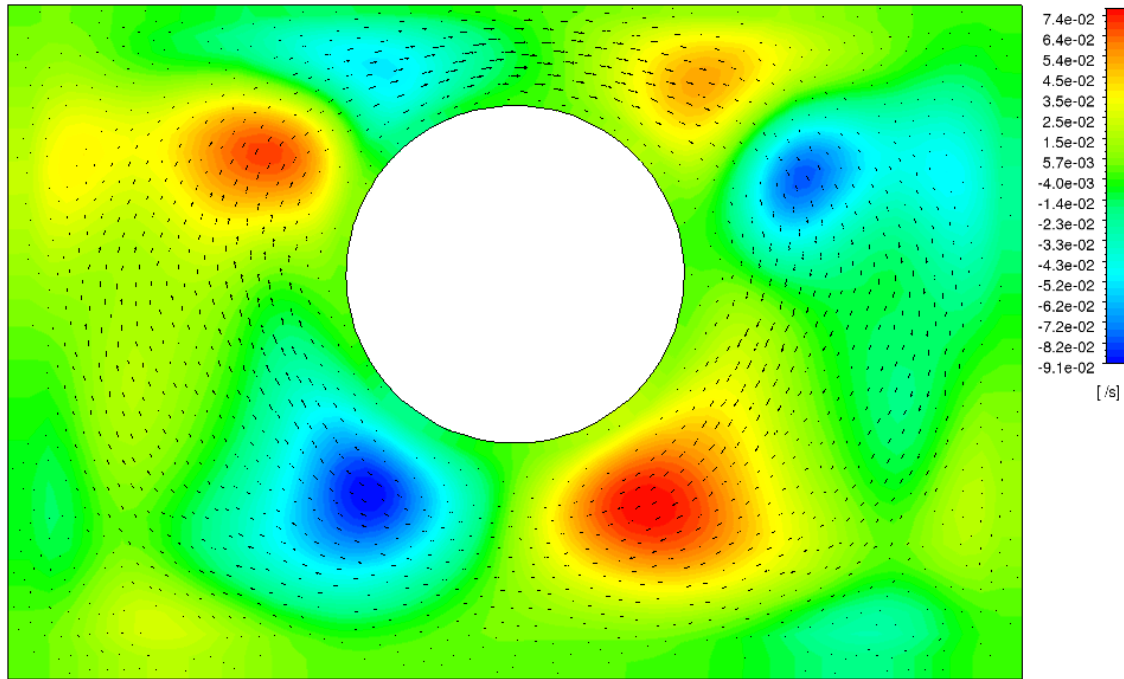


Figure 4.78: Axial velocity gradient contour with crossplane velocity vectors in front. $Re = 718$. Axial flow is into the page. Taken 76.5 seconds after starting the transient from zero velocity. Location is approximately 40 mm downstream from figure 4.77.

Flow can be seen circulating around the rod in figures 4.76 and 4.78. Figure 4.76 shows flow rotating counter clockwise, figure 4.78 shows clockwise rotation. Figure 4.77 shows flow in between rotation states, and does not have a singular direction of flow. The flow in the left subchannel is moving towards the area of positive velocity gradient, whereas the flow in the right subchannel is moving away from the area of negative velocity gradient. These areas act to exchange momentum to and from the crossplane, as shown by the flow movements around them. The change in velocity gradient for figure 4.77 is 0.4 s^{-1} , about one tenth of what is seen in the fully evolved case. Figure 4.77 shows flow transitioning between proto-pulsation states. Figures 4.76 and 4.78, which show those states of proto-pulsation, have a lower change in velocity gradient, about 0.15 s^{-1} . There is a further development and growth of the six regions of axial velocity gradient extremes which were initially seen in figure 4.70. Although the flow is not yet

very strong on the crossplane, it is these regions which are causing it to rotate around the rod, transferring momentum from the axial velocity to the crossplane velocities. The maximum value of the crossplane velocity is about 1.3 mm/s, about a tenth of what the maximum will be in the fully evolved case.

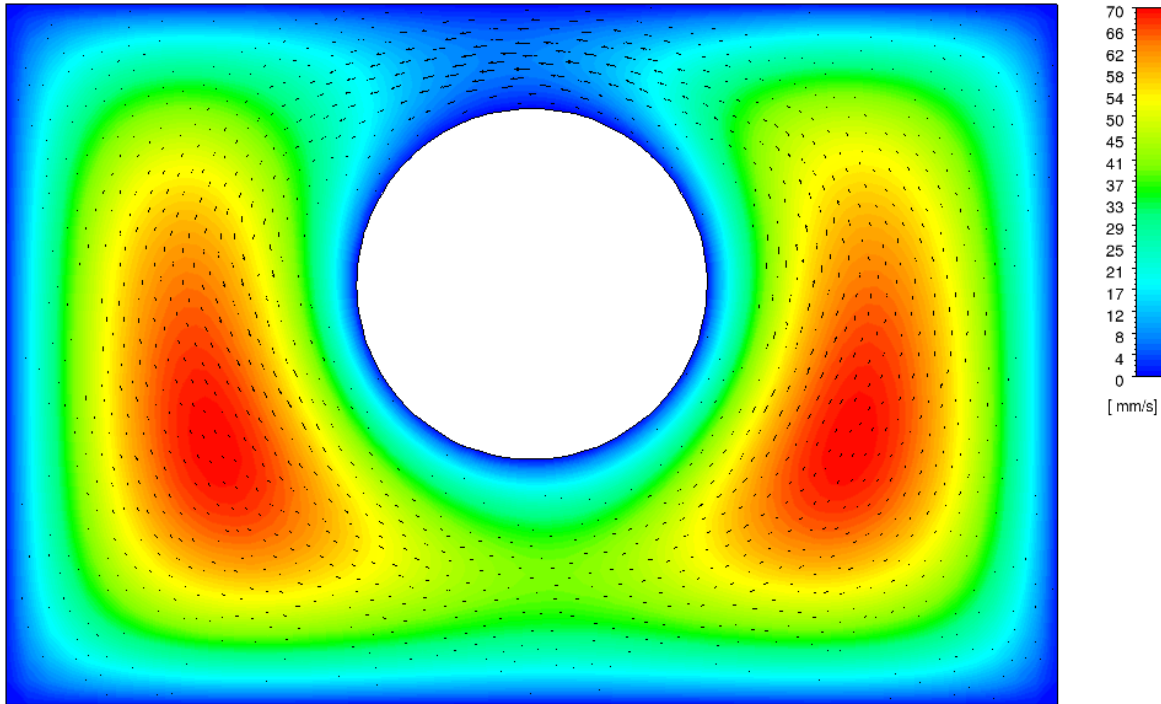


Figure 4.79: Axial velocity contour with crossplane velocity vectors in front. $Re = 718$. Axial flow is into the page. Taken 76.5 seconds after starting the transient from zero velocity. Location is the same as in figure 4.76.

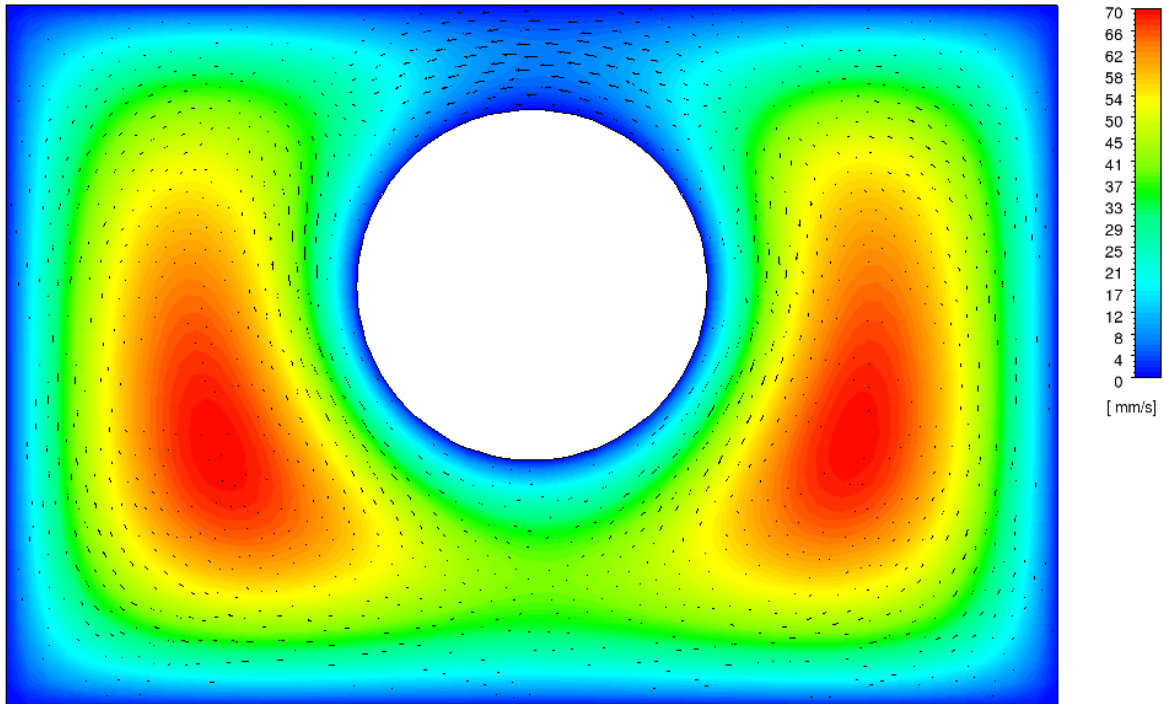


Figure 4.80: Axial velocity contour with crossplane velocity vectors in front. $Re = 718$. Axial flow is into the page. Taken 76.5 seconds after starting the transient from zero velocity. Location is the same as in figure 4.77.

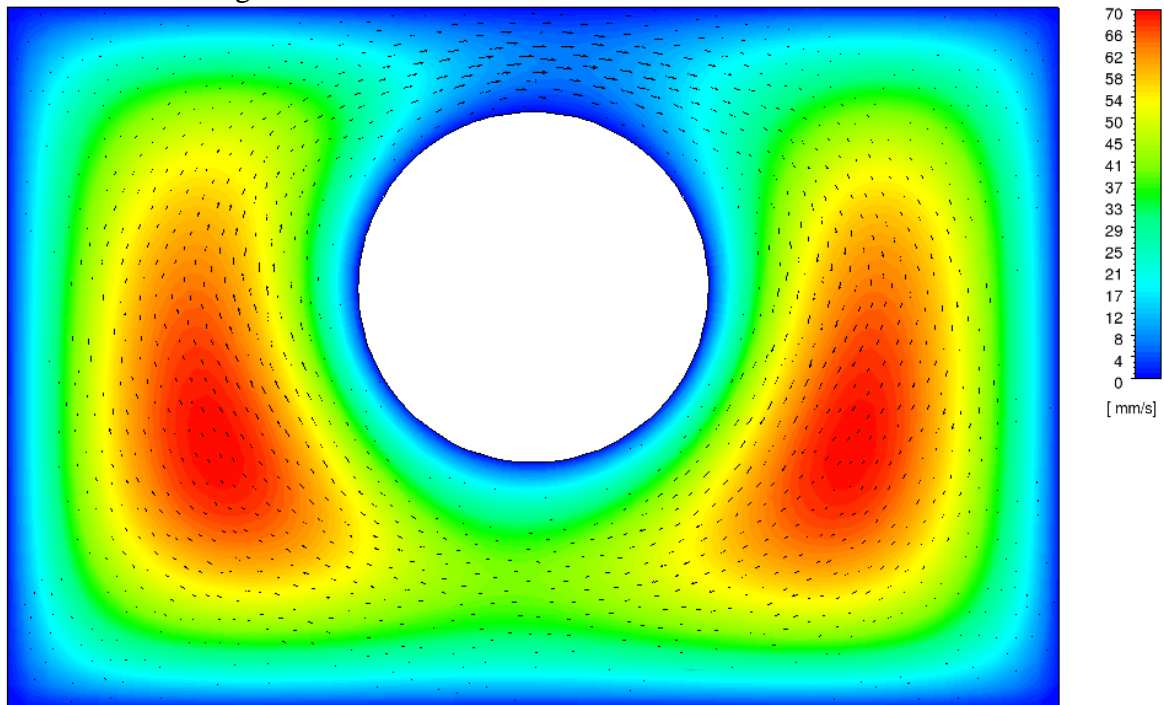


Figure 4.81: Axial velocity contour with crossplane velocity vectors in front. $Re = 718$. Axial flow is into the page. Taken 76.5 seconds after starting the transient from zero velocity. Location is the same as in figure 4.78.

In the snapshots where there is flow rotation, figures 4.79 and 4.81, the axial velocity is pulled slightly higher, with the crossplane flow entering the gap region. In the snapshot where the rotation direction is changing, the axial velocity is much more symmetric. Velocity is highest in near the bottom of each subchannel. Figure 4.80 has the crossplane velocity being very close to zero in the areas where the axial velocity is highest.

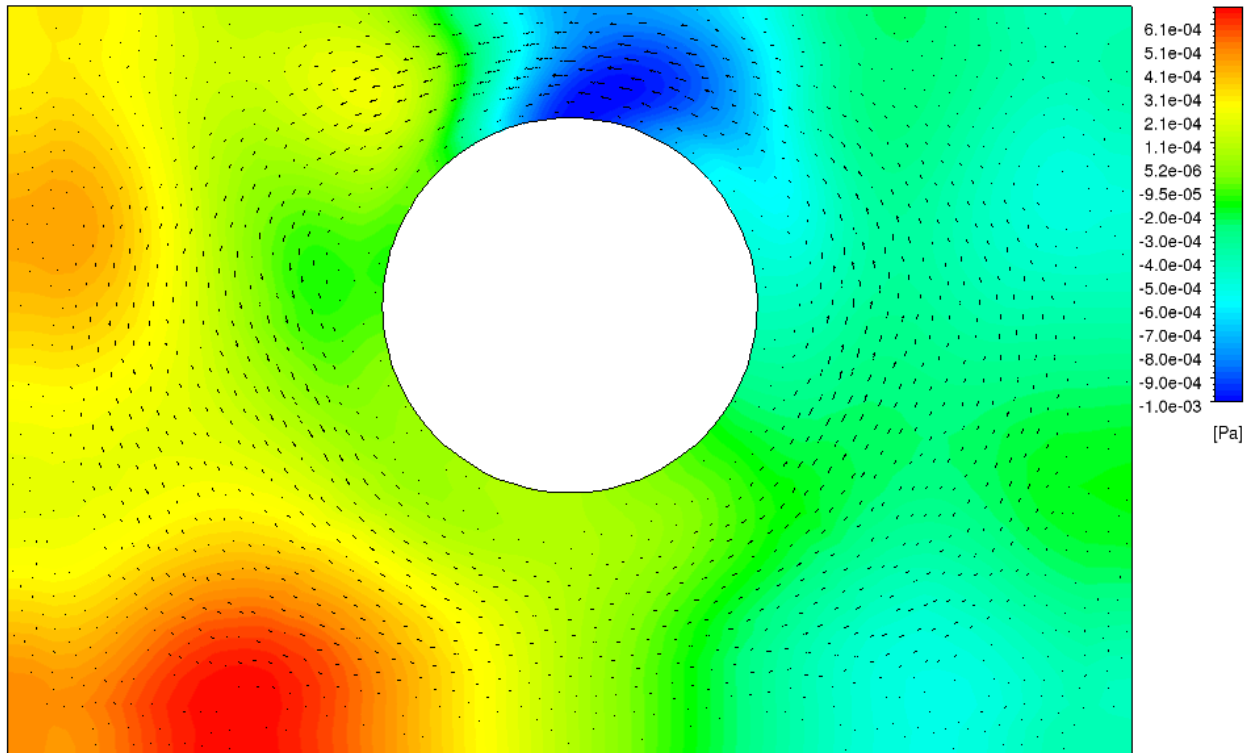


Figure 4.82: Contour of pressure fluctuations with crossplane velocity vectors in front. $Re = 718$. Axial flow is into the page. Taken 76.5 seconds after starting the transient from zero velocity. Location is the same as in figure 4.76.

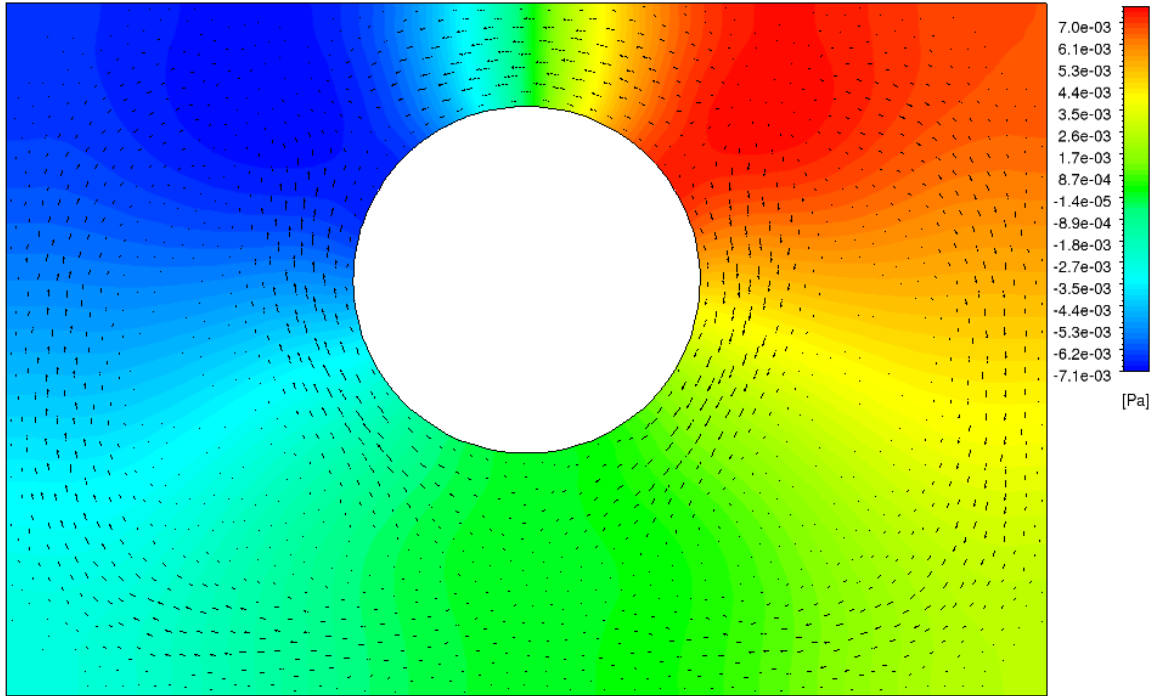


Figure 4.83: Contour of pressure fluctuations with crossplane velocity vectors in front. $Re = 718$. Axial flow is into the page. Taken 76.5 seconds after starting the transient from zero velocity. Location is the same as in figure 4.77.

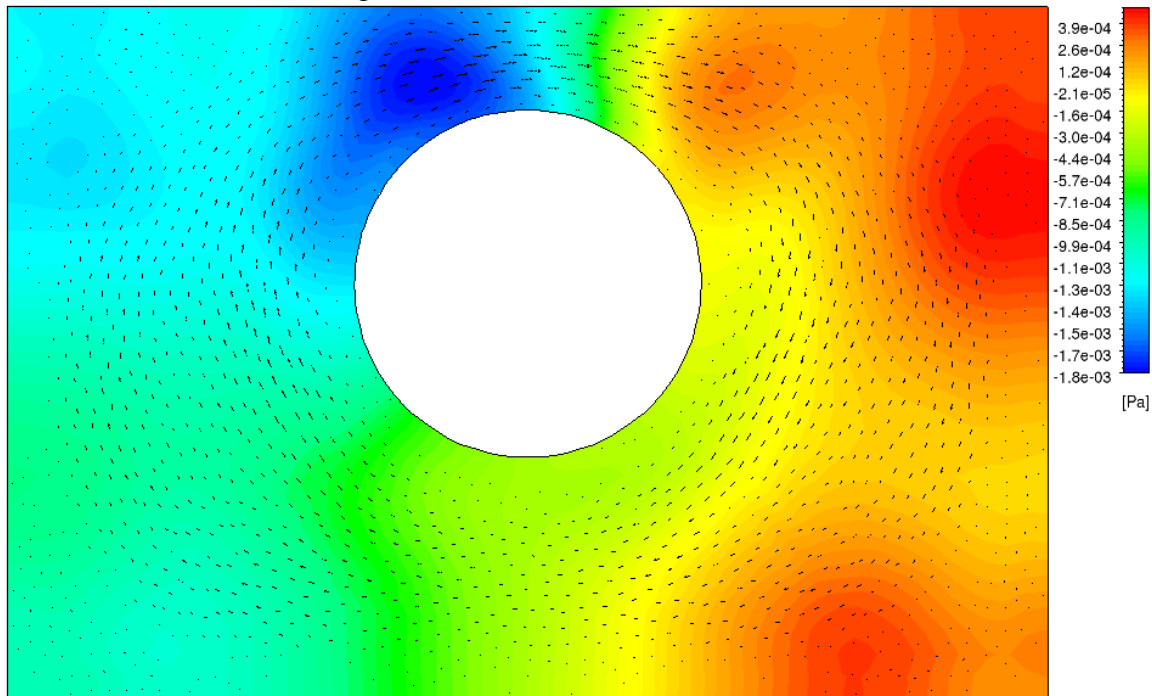


Figure 4.84: Contour of pressure fluctuations with crossplane velocity vectors in front. $Re = 718$. Axial flow is into the page. Taken 76.5 seconds after starting the transient from zero velocity. Location is the same as in figure 4.78.

the pressure distribution is almost split down the middle between high and low values. Total change in pressure is about 0.0017 Pa, about two orders of magnitude less than seen in full evolved flow. There is an area of negative pressure in the gap region, shifted to the side where the crossplane flow is entering. There are areas of high pressure on the wall nearest the flow exiting the gap region, and on the bottom of the domain, within the same subchannel. These regions push the flow down the subchannel and through the secondary gap. In figure 4.85, the pressure extremes are located in the upper part of the right and left subchannels. Below the rod, the pressure fluctuations are essentially zero. Between these regions, there is a fairly steady transition. The distribution of pressures is much more symmetric. The difference in pressure is about 0.014 Pa, about a tenth of what is seen in fully evolved flow.

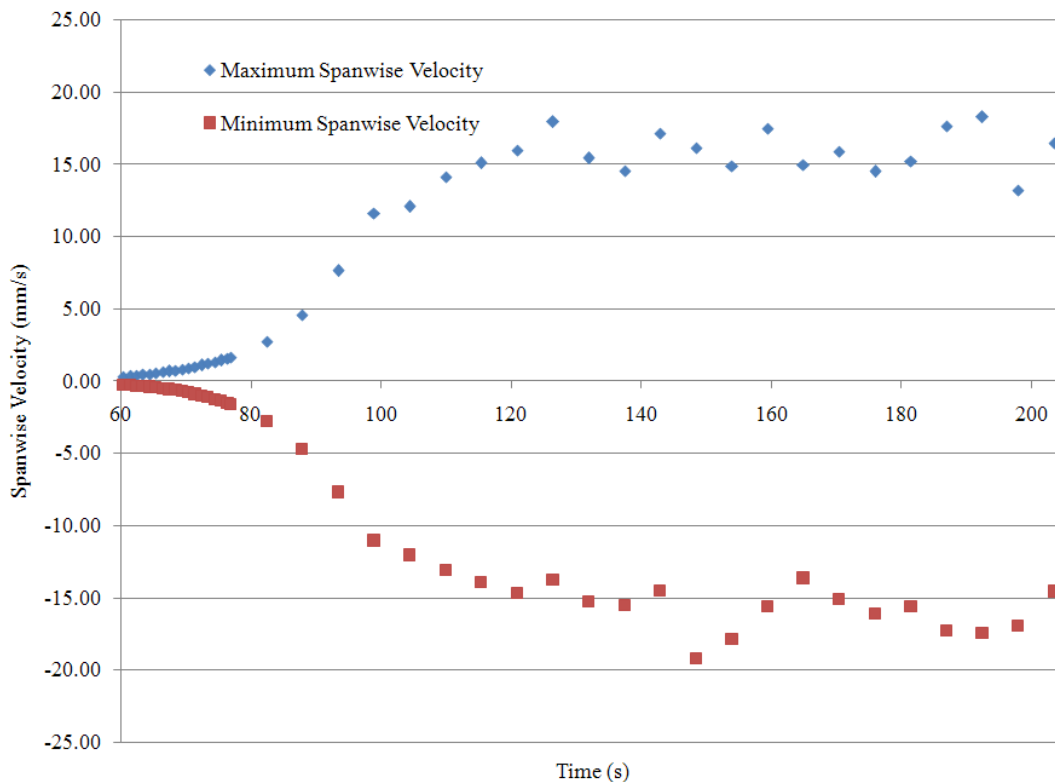


Figure 4.85: Maximum and minimum spanwise velocities seen in the entire domain. Time is taken from when the simulation started with an initial guess of 0 velocity. $Re = 718$

Figure 4.85 shows a measure of the growth of the pulsating flow. Although using the extrema of the spanwise velocity will not show saturation at a constant value, it will demonstrate the increase in the small instability over time. The flow which has purely axial flow up to about 60 seconds after the transient solution started grows to show pulsating flow by about 120 seconds. This pulsating flow saturates and then has extrema which fluctuate around a constant value. From figure 4.59, (60.5 seconds after starting the flow from the initial guess of zero velocity) to figure 4.84 (76.5 seconds after the flow was started), only sixteen seconds were required to bring the flow from insignificant spanwise velocities to one which has disturbances that are large enough not to die out.

The factors which have been important in the development of the pulsating flow are the same as those which were important in the fully evolved case - axial velocity gradient and pressure. The axial velocity gradient with the associated pressure changes results in pressure forces acting in the crossplane resulting in crossflow velocities. This in turn creates further flow disturbance which gives rise to a stronger velocity gradient and the instabilities grow. When compared to the fully evolved case, the magnitudes of the axial velocity gradient and crossplane flow, show a similar reduction factor. This implies that the axial velocity gradient is strongly correlated to the creation and sustaining of the pulsating flow within the domain. There is also a strong linkage between the pressure field and the axial velocity gradient, which was shown very clearly in the full evolved case, and to a lesser extent in figures 4.76 to 4.78, 4.82 to 4.84. As was seen in figures 4.2, 4.3 and 4.4, the pressure field affects the axial velocity, but the change in pressure does not correspond to the spanwise velocity reversing direction at the same location.

The effect of the pulsations on the flow are quite pronounced. As was shown by the particle tracks in figures 4.24, 4.25 and 4.27, flow in the centre of the gap is able to be directed to

the walls of the domain. This means that high speed flow will be pulled into the gap, and lower speed flow from the gap will be mixed with flow in the subchannels. This effect can be seen well in the following two figures (4.86 and 4.87), which show the axial velocity contours for the purely axial flow case as well as averaged for the pulsating flow case.

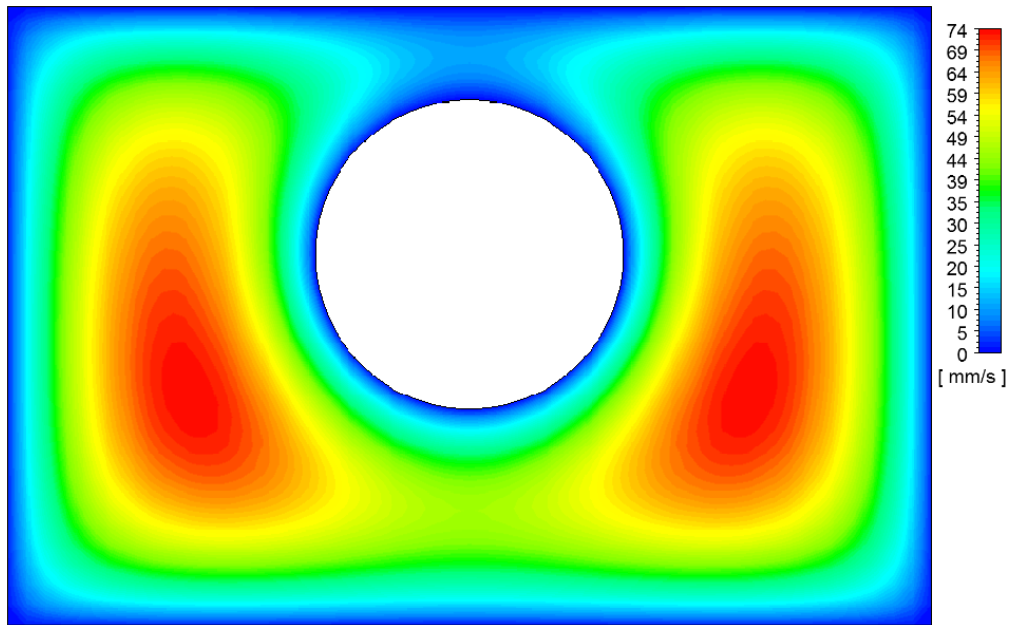


Figure 4.86: Axial velocity contours for purely axial flow. Flow is into the page.

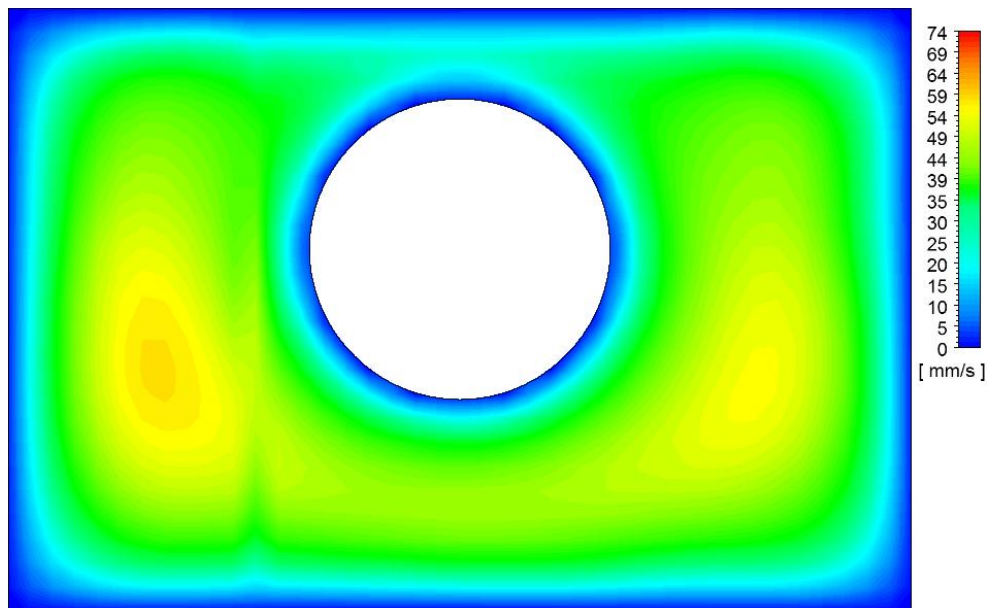


Figure 4.87: Averaged axial velocity contours for pulsating flow. Time is 250 seconds into the true transient. Flow is into the page.

Comparing figures 4.86 and 4.87, it can be seen that the flow in the gap region is much higher for the pulsating flow. In the upper parts of the subchannel, it is clear that the rotations around the rod have pulled in the higher velocity flow in the middle of the subchannels. This in turn has reduced the velocity in the core of the subchannels. In the secondary gap, below the rod, the velocity is much more uniform for the averaged pulsating case than for the purely axial case. This again is a demonstration of the enhanced mixing seen within the domain.

Chapter 5

Closure

5.1 Summary and Conclusions

Numerical simulations of the flow pulsation phenomenon pertaining to subchannel mixing in nuclear fuel channel assemblies were carried out. The geometry considered was a rectangular duct containing a cylindrical rod. The rod was positioned non-symmetrically within the duct to create a gap region between the rod and the duct wall. The presence of the gap is critical for establishing flow pulsations. Validation was achieved using the experimental work of Gosset and Tavoularis [52]. Three different Reynolds numbers (718, 900, 955) within the laminar flow regime were used using the same dimensionless gap size, $\delta/D = 0.3$. These simulations have been demonstrated to be independent of grid size, timestep, and length of domain. The numerical results were analyzed using Q-criterion visualizations along with crossplane vectors and contours of axial velocity gradient, pressure and axial velocity. This analysis yielded results which gave insight into the behaviour of the pulsations as well as some of the important parameters correlated with them. These parameters were then utilized in a study of the evolution of the pulsations to see how the parameters changed from a flow which was purely axial into a flow which had instabilities large enough to grow into the fully evolved pulsating state. The following conclusions may be made about the work presented in this thesis.

1. This work represents the first time, to the author's knowledge, that any successful numerical simulation of laminar flow in subchannel geometries has been carried out. The fact that the pulsations can be obtained in a laminar simulation conclusively demonstrates that the cause of the pulsations cannot be due to turbulence, as some researchers have stated. These simulations have demonstrated the practicality of utilizing a laminar approach to begin to understand subchannel mixing.

2. Validation of the results with experimental data was achieved by comparing a calculated frequency to an experimentally estimated frequency. The numerically obtained frequency came from a discrete point which monitored all three velocities (u,v,w) and pressure for each timestep. The timetrace of spanwise (u) velocity was fast Fourier transformed to obtain the frequency spectrum. The experimental frequency came from visual inspection of dye streaks in the gap region over time. The numerically obtained frequency over predicted the experimental frequency by between 15% and 25%, however the experimental frequency was known to have a standard deviation of 20%. It was also demonstrated that using pathline particle tracking to determine the frequency would not necessarily be expected to give the same frequency as using a Fourier transform on a velocity time trace.

3. In a greatly simplified geometry, using laminar flow, these pulsations have demonstrated the effectiveness of the mixing which is observed. The pulsations are not merely a simple motion in and out of the gap, but are rotating through around the rod, which will result in enhanced mixing. The axial velocity gradient is strongly correlated with the direction and growth of the rotating pulsations. In turn, the pressure field is strongly correlated with the axial velocity gradient.

4. The pulsations evolve from a flow field which is initially purely axial. Small disturbances, near inflection points in the axial velocity profile grow. The resulting axial velocity gradients in turn transfer mass between the axial velocity and the crossplane velocities. Over time, the disturbances reach a sustained stationary state, with complex cross stream flow through both the gaps and channels.

5.2 Recommendations for Future Work

1. Further research into the effect of multiple gaps should be performed. Multiple studies have been conducted using geometries with only one gap [45,49,53], as well as a single rod inside a larger domain [14-16,52], which gives two gaps. However, it is not known how an odd number of gaps would interact with each other. In the case of three gaps, if one gap has flow pulsing in, it is unclear how the flow would behave in the other two gaps. The geometry investigated by Silin and Juanicó [38,40] is one that if instrumented more rigorously, would yield very interesting results.

2. Conducting more laminar studies which use more instrumentation (eg. PIV) that allowed for a transient velocity signal to be recorded would be beneficial. This would allow work to be done that could investigate the Reynolds number dependence on frequency and gap size in the laminar regime, using more reliable methods for obtaining the frequency.

3. It would also be interesting numerically to study the change in frequency as gap size and Reynolds number are varied, extending the work of Gosset and Tavoularis [53]. It is postulated that, as the gap size is increased from zero, gap cross-flow resistance initially decreases, until the

frequency becomes a maximum. After this point, increasing the gap size will most likely decrease the strength of the driving mechanism behind the pulsations. Further work would give valuable insight into the relationship between gap size, frequency and Reynolds number.

The experimental work mentioned above would allow the laminar numerical investigation into subchannel mixing to continue. Future numerical laminar analysis should be done using more complex geometries than the domain simulated in this work. Further utilization of increasingly geometrically complex laminar simulations will allow a fundamental understanding of subchannel mixing to be attained. From this understanding, a consideration of the turbulent regime, with the knowledge gained from the laminar simulations and experiments can be made. This would be an effective way to gain real insight into the complex phenomenon that is subchannel mixing.

Bibliography

- [1] T. Van Der Ros and M. Bogaardt. Mass and heat exchange between adjacent channels in liquid-cooled rod bundles. *Nuclear Engineering and Design*, Vol 12. pp 259 - 268, 1970.
- [2] M.S. Guellouz and S. Tavoularis. Heat transfer in rod bundle subchannels with varying rod-wall proximity. *Nuclear Engineering and Design*, Vol.132, pp 351-366, 1992.
- [3] L. Meyer. From discovery to recognition of periodic large scale vortices in rod bundles as source of natural mixing between subchannels -- A review. *Nuclear Engineering and Design*, Vol. 240, pp 1575 - 1588, 2010
- [4] H-Y. Jeong, K-S. Ha, Y-M. Kwon, Y-B. Lee, D. Hahn. A dominant geometrical parameter affecting the turbulent mixing rate in fuel rod bundles. *International Journal of Heat and Mass Transfer*. Vol. 50, pp 908 - 918, 2007.
- [5] O.S. Eiff, and M.F. Lightstone. On the modeling of single-phase turbulent energy transport in subchannels. *Proceedings of the Annual Conference - Canadian Nuclear Society*, 1997.
- [6] G. Arvanitis. Simulation of flow pulsations in gap geometries using unsteady Reynolds averaged Navier-Stokes modelling. *M.A.Sc. Thesis*, McMaster Univ., Hamilton, Ontario, Canada, 2008.

- [7] W. Eifler and R. Nijising. Experimental investigation of velocity distribution and flow resistance in a triangular array of parallel rods. *Nuclear Engineering and Design*, Vol. 5, pp 22-42, 1967.
- [8] D.S. Rowe, B.M. Johnson and J.G. Knudsen. Implications concerning rod bundle crossflow mixing based on measurements of turbulent flow structure. *International Journal of Heat and Mass Transfer*, Vol 17, pp . 1974
- [9] K. Rehme. The structure of turbulent flow through a wall subchannel of a rod bundle. *Nuclear Engineering and Design*, Vol 45, pp 311-323, 1978.
- [10] J.D. Hooper and K. Rehme. Large-scale structural effects in developed turbulent flow through closed spaced rod arrays. *Journal of Fluid Mechanics*, Vol.145, pp 305-337. 1984
- [11] M. Renksizbulut and G.I. Hadaller. An experimental study of turbulent flow through a square array rod bundle. *Nuclear Engineering and Design*, Vol. 91, pp 41-55, 1986.
- [12] S.V. Moller. On phenomenon of turbulent flow through rod bundles. *Experimental Thermal and Fluid Science*. Vol 4, pp 25-35, 1991.
- [13] T. Krauss and L. Meyer. Characteristics of turbulent velocity and temperature in a wall channel of a heated rod bundle. *Experimental Thermal and Fluid Science*, Vol 12, pp 75-86, 1996.
- [14] M.S. Guellouz, and S. Tavoularis. The structure of turbulent flow in a rectangular channel containing a cylindrical rod - Part 1: Reynolds-averaged measurements. *Experimental Thermal and Fluid Science*, Vol 23, pp 59-73. 2000a

- [15]M.S. Guellouz, and S. Tavoularis. The structure of turbulent flow in a rectangular channel containing a cylindrical rod - Part 2: phase-averaged measurements. *Experimental Thermal and Fluid Science*, Vol 23, 75-91. 2000b
- [16]E. Piot and S. Tavoularis. Gap instability of laminar flows in eccentric annular channels. *Nuclear Engineering and Design*, 2011.
- [17]P. Carajilescov and N.E. Todreas. Experimental and analytical study of axial turbulent flows in an interior subchannel of a bare rod bundle. *Journal of Heat Transfer*, Vol. 98, No. 2, 1976
- [18] W. Seale. Turbulent diffusion of heat between connected flow passage; Part 2: Prediction using k- ϵ turbulence model. *Nuclear Engineering and Design*, Vol. 54, pp 197-209, 1979b.
- [19]C.W. Rapley and A.D. Gosman. The prediction of fully developed axial turbulent flow in rod bundles. *Nuclear Engineering and Design*, Vol. 97, pp 313 - 325, 1986.
- [20]X.Wu. Numerical study on the turbulence structures in closely spaced rod bundle subchannels. *Numerical Heat Transfer Part A - Applications*. Vol. 25, pp 649 - 670, 1994.
- [21]Y.K. Suh and M.F. Lightstone. Numerical simulation of turbulent flow and mixing in a rod bundle geometry. *Nuclear Energy*, Vol. 43, pp. 1-11, 2004.
- [22]D. Chang and S. Tavoularis. Unsteady numerical simulations of turbulence and coherent structures in axial flow near a narrow gap. *Journal of Fluids Engineering*, Vol. 127, pp 458 - 466, 2005.

- [23]F. Abbasian S.D. Yu and J. Cao. Experimental and numerical investigations of three-dimensional turbulent flow of water surrounding a CANDU simulation fuel bundle structure inside a channel. *Nuclear Engineering and Design*, Vol. 239, pp 2224 - 2235, 2009.
- [24]D. Home, G. Arvanitis, M. Lightstone, M. Hamed. Simulation of flow pulsations in a twin rectangular subchannel geometry using unsteady Reynolds averaged Navier-Stokes modelling. *Nuclear Engineering and Design*, Vol. 239, pp 2964 - 2980, 2009.
- [25] Y.D. Levchenko, V.I. Subbotin and P.A. Ushakov. Experimental investigation of averaged characteristics of turbulent flow in cells of rod packs. *Atomic Energy*, Vol. 33, pp 1035 - 1042, 1972.
- [26] B.H. Ouma and S. Tavoularis. Flow measurements in rod bundle subchannels with varying rod-wall proximity. *Nuclear Engineering and Design*, Vol. 131, pp 193 - 208, 1991.
- [27] F.B. Gessner and J.B. Jones. On some aspects of fully-developed turbulent flow in rectangular channels. *Journal of Fluid Mechanics*, Vol. 23, pp 689 - 713, 1965.
- [28] V.R. Skinner, A.R. Freeman and H.G. Lyall. Gas mixing in rod clusters. *International Journal of Heat and Mass Transfer*, Vol. 12, pp 265 - 278, 1969.
- [29] F. Tachibana, A. Oyama, M. Akiyama and S. Kondo. Measurement of heat transfer coefficients for axial air flow through eccentric annulus and seven-rod cluster. *Journal of Nuclear Science and Technology*, Vol. 6, pp 207 - 214, 1969.
- [30] A.C Trupp and R.S Azad, "The structure of turbulent flow in triangular array rod bundles", *Nuclear Engineering and Design*, Vol. 32, 1975, pp 47-84

- [31] A. Melling and J.H. Whitelaw. Turbulent flow in a rectangular duct. *Journal of Fluid Mechanics*, Vol. 78, pp 289 - 315, 1976.
- [32] A.M.M. Aly, A.C. Trupp, and A.D. Gerrard. Measurements and predictions of fully developed turbulent flow in an equilateral triangular duct. *Journal of Fluid Mechanics*, Vol. 85, pp 57-83, 1982.
- [33] W.J. Seale. Measurements and predictions of fully developed turbulent flow in a simulated rod bundle. *Journal of Fluid Mechanics*, Vol. 123, pp 399 - 423, 1982.
- [34] V. Vonka. Measurement of secondary flow vortices in a rod bundle. *Nuclear Engineering and Design*, Vol. 106, pp 191 - 207, 1988.
- [35] V. Vonka. Turbulent transports by secondary flow vortices in a rod bundle. *Nuclear Engineering and Design*, Vol. 106, pp 209 - 220, 1988.
- [36] X. Wu and A.C. Trupp. Experimental study on the unusual turbulence intensity distributions in rod-to-wall gap regions. *Experimental Thermal and Fluid Science*, Vol. 6, pp 360 - 370, 1993.
- [37] X. Wu and A.C. Trupp. Spectral measurements and mixing correlation in simulated rod bundle subchannels. *International Journal of Heat and Mass Transfer*, Vol. 37, pp 1277 - 1281, 1994.
- [38] F.S. Castellana, W.T. Adams and J.E. Casterline. Single-phase subchannel mixing in a simulated nuclear fuel assembly. *Nuclear Engineering and Design*, Vol. 26, pp 242 - 249, 1974.

- [39] W.J. Seale. Turbulent diffusion of heat between connected flow passages; Part 1: Outline of problem and experimental investigation. *Nuclear Engineering and Design*, Vol. 54, pp 183 - 195, 1979.
- [40] J.D. Hooper. Developed single phase turbulent flow through a square-pitch rod cluster. *Nuclear Engineering and Design*. Vol. 60, pp 365-379, 1980.
- [41] K. Rehme. On the development of turbulent flow in wall subchannels of a rod bundle. *Nuclear Technology*, Vol. 77, pp 341 - 342, 1987.
- [42] L. Meyer. Measurements of Turbulent Velocity and Temperature in Axial Flow Through a Heated Rod Bundle. *Nuclear Engineering and Design*, Vol. 146, pp. 71-82, 1994.
- [43] K. Rehme. Experimental observations of turbulent flow through subchannels of rod bundles. *Experimental Thermal and Fluid Science*, Vol. 2, pp 341 - 349, 1989.
- [44] S.R. Wu and K. Rehme. An experimental investigation on turbulence flow through symmetric wall subchannels of two rod bundles. *Nuclear Technology*, Vol. 89, pp 103 - 115, 1990.
- [45] S.V. Moller. Single-Phase Turbulent Mixing in Rod Bundles. *Experimental Thermal and Fluid Science*. Vol. 4, pp 26-33, 1991.
- [46] L. Meyer and K. Rehme. Large-scale turbulence phenomena in compound rectangular channels. *Experimental Thermal and Fluid Science*, Vol. 8, pp 286 - 304, 1994.
- [47] X.H. Wu. On the transport mechanisms in simulated heterogeneous rod bundle subchannels. *Nuclear Engineering and Design*, Vol. 158, pp.125-134, 1995.

- [48] T. Krauss and L. Meyer. Characteristics of turbulent velocity and temperature in a wall channel of a heated rod bundle. *Experimental Thermal and Fluid Science*, Vol. 12, pp 75-86. 1996
- [49] N.Silin, L. Juanicó, and D. Delmastro. Thermal mixing between subchannels: measurement method and applications. *Nuclear Engineering and Design*, Vol. 227, pp 51-63, 2004
- [50] A.S. Lexmond, R.F. Muddle, T.H.J.J van der Hagen. Visualisation of the vortex street and characterisation of the cross flow in the gap between two sub-channels. *Proceedings of the 11th International Topical Meeting on Nuclear Reactor Thermal-Hydraulics*, 2005.
- [51] F. Baratto, S.C.C. Bailey, S. Tavoularis. Measurements of frequencies and spatial correlations of coherent structures in rod bundle flows. *Nuclear Engineering and Design*, Vol. 236, pp 1830 - 1837, 2006.
- [52] N.Silin and L. Juanicó. Experimental study on the Reynolds number dependence of turbulent mixing in a rod bundle. *Nuclear Engineering and Design*, Vol. 236, pp. 1860-1866, 2006.
- [53] A.Gosset and S. Tavoularis. Laminar flow instability in a rectangular channel with a cylindrical core. *Physics of Fluids*, Vol. 18, pp 1-8, 2006.
- [54] A. Mahmood, M. Rohde, T.H.J.J. van der Hagen, R.F. Mudde. Contribution of large-scale coherent structures towards the cross flow in two interconnected channels. *Proceedings of the 13th International Topical Meeting on Nuclear Reactor Thermal Hydraulics*, 2009.
- [55] A.C. Trupp and A.M.M. Aly. Predicted secondary flows in triangular array rod bundles. *Journal of Fluids Engineering - Transactions of the ASME*. Vol. 101, pp 354 - 363 , 1979.

- [56] K.B. Lee and H.C. Jang. A numerical prediction on the turbulent flow in closely spaced bare rod arrays by a nonlinear k- ϵ model. *Nuclear Engineering and Design*, Vol. 172, pp 351 - 357, 1997.
- [57] R.C.K. Rock and M.F. Lightstone. A numerical investigation of turbulent interchange mixing of axial coolant flow in rod bundle geometries. *Numerical Heat Transfer*, Vol. 40, pp 221-237, 2001
- [58] Y.K. Suh and M.F. Lightstone. Numerical simulation of turbulent flow and mixing in a rod bundle geometry. *Nuclear Energy*, Vol. 43, pp 153 - 163, 2004.
- [59] E. Baglietto and H. Ninokata. A turbulence model study for simulating flow inside tight lattice rod bundles. *Nuclear Engineering and Design*, Vol. 235, pp 773 - 784, 2005.
- [60] S. Tóth and A. Aszódi. CFD analysis of flow field in a triangular rod bundle. In *The 12th International Topical Meeting on Nuclear Reactor Thermal Hydraulics (NURETH-12)*, 2007.
- [61] S. Tóth and A. Aszódi. CFD analysis of flow field in a triangular rod bundle. *Nuclear Engineering and Design*, Vol. 240, pp 352-363, 2010.
- [62] D. Chang and S. Tavoularis. Convective heat transfer in turbulent flow near a gap. *Journal of Heat Transfer*, Vol. 128, 2006, pp 701 - 708
- [63] D. Chang and S. Tavoularis. Simulations of turbulence, heat transfer and mixing across narrow gaps between rod-bundle subchannels. *Nuclear Engineering and Design*, Vol. 238, pp 109 - 123, 2008.

- [64] D. Chang and S. Tavoularis, "Numerical simulation of turbulent flow in a 37-rod bundle", *Nuclear Engineering and Design*, Vol. 237, 2007, pp 575 - 590
- [65] E. Merzari, H. Ninokata, E. Baglietto. Numerical simulation of flows in tight-lattice fuel bundles. *Nuclear Engineering and Design*, Vol. 238, pp 1703 - 1719, 2008.
- [66] ANSYS CFX® Academic Research, Release 12.0, *Solver Theory Guide*, Discretization of the Governing Equations, ANSYS, Inc.
- [67] J.C.R. Hunt, A.A. Wray and P. Moin. Eddies, streams and convergence zones in turbulent flows. *Center for Turbulence Research Proceedings of the Summer Program 1988*, pp 193 - 208, 1988.
- [68] R. Cucitore, M. Quadrio and A. Baron. On the effectiveness and limitations of local criteria for the identification of a vortex. *European Journal of Mechanics B-Fluids*, Vol. 18, pp 261 - 282, 1999.